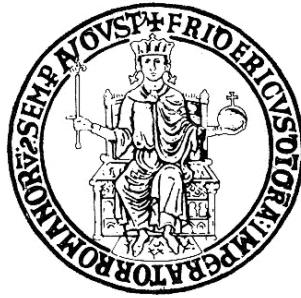**PhD in Industrial Product and Process Engineering**

XXX cycle

University of Naples Federico II

Manipulation of polymeric fluids through pyro-electro-hydro-dynamics

Federico Olivieri

Department of Chemical, Materials and Production Engineering

Tutor: Prof. Giuseppe Mensitieri

Co-tutor: Prof. Andrea D'Anna - Dr. Pietro Ferraro

February 2018

Contents

Aim of the work

This thesis is focused on the manipulation of liquids and polymeric fluids in a non-contact and electrode-free way, exploiting pyro-electro-hydro-dynamic effect. In the following, there will be described the pyro-electro-hydro-dynamic techniques, their possible applications in different field of technology and the obtained results. It will be showed as the versatility of these methods makes pyro-electro-hydro-dynamics very attractive to many scientific fields, such as optics, microfluidics, biology and chemistry. All the reported works were developed at CNR-ISASI laboratories. The thesis structure provides an introduction based on the theory and the combination between pyroelectric and electro-hydro-dynamic effect, with a focus on the developed techniques, followed by the presentation of the realized works.

Specifically, in Chapter 1 the theory and the basis of the pyro-electro-hydro-dynamics will be explained; it will be shown its potential and how we propose to use this combined effect.

In Chapter 2 it will be presented the fabrication of micro-optical devices, in particular micro-lenses, through pyro-electro-hydro-dynamic effect. Micro-lenses find application in communications, three-dimensional displays, optical data storage and photo-detectors. In the second chapter the micro-lens fabrication will be described using two different approaches: first, by an ink-jet technology, and then through self-assembly on a micro-engineered pyroelectric crystal. Starting from the need to simplify the electro-hydro-dynamic printing technology and increase the range of printable materials, a new pyro-ink-jet set-up will be proposed, which will permit to avoid the use of electrodes and nozzle. Then, further modifications of the set-up will improve the flexibility of the technique, for example extending the range of suitable substrates. After that, the micro-lenses will be optically and geometrically characterized and it will be presented the fabrication of a multi-component device as an example of application of this technique. The results demonstrate that pyro-ink-jet printing permit to realize very uniform micro-lenses arrays with high resolution (diameter ~ 300 nm). The

second approach proposed is based on the self-assembly of a micro-lenses array on a micro-engineered pyroelectric crystal. It will be showed the fabrication of a micro-lens array decorated by nano-particles, such as quantum dots, and it will be discussed the di-electro-phoretic effect for the self-assemblong of the employed dots. In particular, the study will focus on the effect of the patterned substrate on the localization of the nano-particles and on the investigation of the dots pattern transfer. The most attractive application of these nano-composites is in optic and photonic sectors: quantum dots, in fact, find great interest in solar cells and energy harvesting.

Chapter 3 will show another application of pyro-ink-jet printing: the capability of this system in the manipulation of highly viscous polymeric solution, allowing the deposition of polymeric fibers. The results presented demonstrate that pyro-ink-jet printer is also a valid alternative to the classic electro-spinning system, avoiding electrodes and spiraling effect during the deposition. The fibers produced show great uniformity and reach thicknesses until the nano-metric scale. The possibility to use biodegradable and biocompatible polymers ensures large application in attractive fields such as biology, chemistry and microfluidics. Moreover, in this chapter it will be shown how a polymeric fiber, deposited through pyro-ink-jet printing, can be used as a component in a microfluidic channel, fabricated subsequently to the fiber deposition. Finally, all the procedures used to realize micro-channel will be illustrated.

CHAPTER 1

PYRO-ELECTRO-HYDRO-DYNAMICS

1.1 Pyroelectric effect

Pyroelectricity is a property of particular materials which exhibit a spontaneous polarization that depends on the temperature[1]. This property depends on the molecular structure of the material: a pyroelectric solid has inner dipoles, due to the presence of cations or anions in the structure[2]. In equilibrium conditions (constant temperature), each dipole has its orientation and the total electric dipole moment is zero. A temperature variation induces a movement between the atoms (which have a certain mobility) and, for that reason, a change in the dipoles strength (therefore, the polarity[3]) and, consequentially, a charge displacement on the material surface, i.e. an electric current.
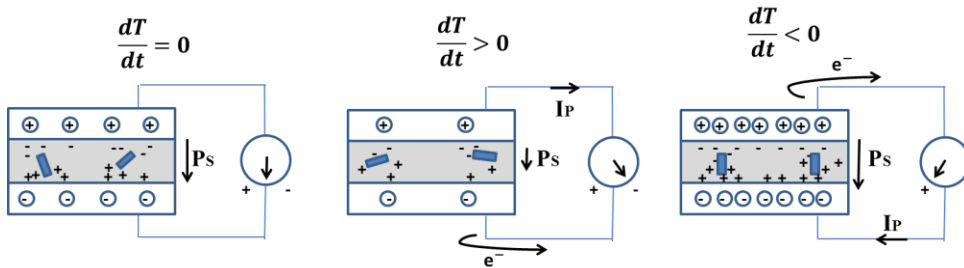
Figure 1.1. Circuital representation of pyroelectric working at constant temperature, under heating and under cooling.

It is important to underline that, if the material remains at the same temperature, after it has undergone to a thermal variation, the inner domains work to recover an equilibrium, crowding the charges on the external surfaces, reinstating the starting polarization and setting to zero the electric field. That means just a thermal gradient induces an electric current[2,4]. Thermoelectricity shows similar characteristics, compared to pyroelectricity. Nevertheless, while a thermoelectrical material, once heated, produces an electric current and a stable electrical potential, due to the inner displacement of electrons and holes[5], a pyroelectric material attracts electrons from the external ambient, in order to compensate the exceed of charges occurred on the surface[2]. The phenomenon

depends on the set temperature: in fact the Curie temperature is the temperature at which the polarization goes to zero[1,6].

1.1.2 Pyroelectric materials and properties

1.1.2.1 Pyroelectric material classes

A pyroelectric material can be either a ceramic or a polymer. Between ceramics there are lead zirconate titanate (PZT, $Pb[Zr_xTi_{1-x}]O_3$), barium titanate ($BaTiO_3$), lithium titanate ($LiTiO_3$), lithium niobate ($LiNbO_3$), lithium tantalate ($LiTaO_3$)[7] or the more complex lead magnesium niobate-lead titanate ($yPbMg_xNb_{1-x}O_3-1-yPbTiO_3$, PMN-PT) and lead zirconate niobate-lead titanate ($yPbZr_xNb_{1-x}O_3-1-yPbTiO_3$, PZN-PT)[8-11]. PZT based ceramics are probably the most common used, due to its chemical and mechanic stiffness, their high Curie temperatures (suitable, for example, for space applications) and, moreover, the variation of the Zr/Ti ratio, combined to the addition of dopants, allows to largely modify the physical properties of the material[2,12]. Pyroelectric polymers include polyvinylidene fluoride (($C_2H_2F_2)_n$, PVDF), polyvinylidene fluoride trifluoroethylene (($C_2H_2F_2)_n$-(($C_2HF_3)_m$, P(VDF-TrFE), which have the highest pyroelectric coefficient ever signed: $40\mu C/m^2K$)[13] and polyvinylidene fluoride trifluoroethlyenechlorofluoroethylene (($C_2H_2F_2)_n$-(($C_2HF_3)_m$-($C_2H_2FCl)_p$, P(VDF-TrFE-CFE))[7,14]. Obviously, in order to be pyroelectric, a polymer has to be semi-crystalline. That is a critical point because PVDF can crystallize in a α, β and γ-phase, and the more stable phase is the α one, which is paraelectric. Moreover, without external stresses, PVDF crystallizes in the α-phase too. Instead, β-phase exhibits the strongest pyroelectric properties[15], while γ-phase have chain conformation in between that of the α and β-phases, showing weak pyroelectric properties. The way to obtain one of the pyroelectric phases goes through the structure mechanic deformation and the poling (an electric process that attends to the polarization and the dipole moments orientation in the direction

9

of an applied external electric field and that will treated in the following sections)[7,15]. It is also possible to obtain a δ-phase simply poling the α-phase, making it polar[15]. Compared to PVDF, the pyroelectric β-phase of P(VDF-TrFE) is achieved without external stresses[16]. Furthermore, P(VDF-TrFE) has a Curie temperature lower and a dielectricity 25 times greater than the ones of pyroelectric ceramics[17-18]; these properties make this polymer suitable for particular application such as power generation or low temperature harvesting. Pyroelectric polymers have the advantage of being very cheap and easy to manipulate, allowing to work at low temperature. Their use occupies, in particular, biomedical and industrial fields[6-7,19]. However, in nature, pyroelectricity has been observed in minerals (such as tourmaline, probably the first pyroelectric material ever discovered[20] or quartz[2]) or biological materials (such as bones or tendons)[2,21-22].

1.1.2.2   Pyroelectricity, piezoelectricity and ferroelectricity

A pyroelectric is always a piezoelectric also, due to the existence of polarizable domains. Not all the piezoelectric materials are pyroelectric too; this is caused by the inner structure of pyroelectrics. In fact, a pyroelectric crystal is asymmetric, while the charges accumulation occurs along orthogonal faces relative to a symmetry axis. Indeed, some piezoelectric crystals have a symmetry that prevents pyroelectricity. Moreover, ferroelectric materials are also pyroelectrics, being able to reverse their spontaneous polarization if submitted to an electric field7. However, not all the pyroelectric materials can invert their polarization in the same conditions23. More in general, there are 32 classes of dielectric crystals, 21 of these are not symmetrical and 20 are piezoelectric. Among these, 10 are paraelectrics (do not exhibit a spontaneous polarization, but only in presence of external electric fields), while the other 10 are pyroelectrics. Therefore, these are divided in ferroelectrics and non-ferroelectrics7. In Fig. 2.1 is showed a recapitulative scheme:
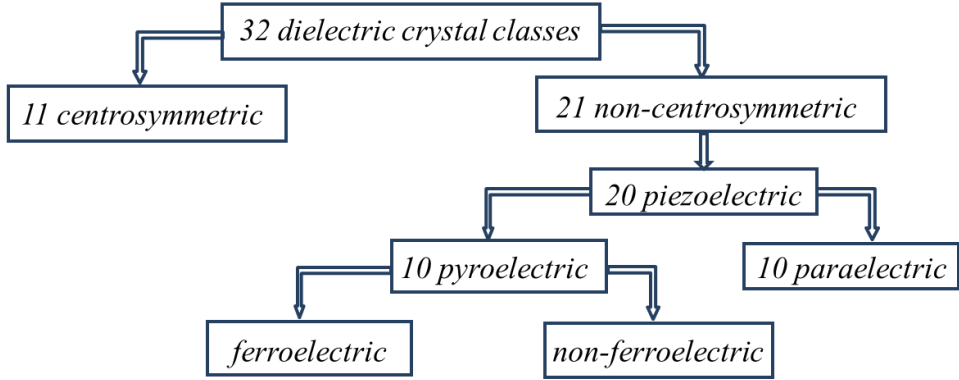
Figure 1.2. Classification of crystals: piezoelectrics, pyroelectrics and ferroelectrics.

1.1.3 Analytical interpretation of pyroelectricity

The dependence of the spontaneous polarization P_S (C/m^2) from the temperature is described by the pyroelectric coefficient p (C/m$^2 \cdot$ K), which is a vector expressed as:

$$\bar{p} = \left(\frac{\partial \overline{P_S}}{\partial T}\right)_{\bar{E}, \bar{\bar{\sigma}}} \tag{1}$$

where E is the electric field, expressed in V/m, and σ is the elastic stress, expressed in Pa. More precisely, p reported in Eq. 1 is named pyroelectric thermodynamic coefficient, while p_e showed in Eq. 2 is the pyroelectric experimental coefficient and is calculated as the variation of charges due to a thermal variation dQ/dT on a surface A[24-25].

$$p_e = \frac{1}{A}\frac{dQ}{dT} \tag{2}$$

Note that the pyroelectric experimental coefficient is a scalar and its value is usually lower than the modulus of p. The electric displacement D of the atoms is the effect of pyroelectricity in a material and can be expressed as[2]:

$$d\bar{D} = \bar{p}dT \tag{3}$$

That means that, if E is constant, D is equal to P_S. This is clear considering the formula that expresses D of an isotropic pyroelectric material[3,26]:

$$\overline{D}(E,T) = \varepsilon_0 \varepsilon_r(T) \overline{E} + \overline{P}_S(T) \qquad (4)$$

where ε_0 is the vacuum permittivity $(= 8.854x10^{-12} C/V \cdot m)$ and $\varepsilon_r(T)$ is the relative permittivity of the material at electric field E and temperature T.

Known I_P as the electric current generated by pyroelectric materials submitted to a thermal treatment (see Fig. 1.1), its expression can be written (considering linear behaviors relative to the heating or cooling[27]) as:

$$I_P = A|\overline{p}|\frac{dT}{dt} \qquad (5)$$

where A is the stimulated surface on the material[28-29]. The current generated by pyroelectric materials, at the best, is in the range of micro-amperes, but, normally, it does not exceed pico-amperes. However, the evaluation of pyroelectricity is made considering constant the volume of the material, during the thermal treatment: this effect is called primary pyroelectricity. When a thermal gradient is applied on the material, its volume changes, so all the parameters that concern the geometry are altered and a secondary pyroelectricity occurs, due to the piezoelectric effect[2,30].

1.2 EHD phenomenon

Electro-hydro-dynamics (EHD) is a phenomenon that describes the interactions of a liquid drop subjected to an electric field. A charge displacement is induced in the liquid due to the electric field that employs attractive and repulsive forces with the liquid molecules[31-32]. The result consists on the deformation of the liquid drop that assumes a conical shape, known as Taylor's cone[33], due to a charges accumulation at the interface[34-35].

Figure 1.3.Taylor's cone.

In particular, Taylor's cone is an equilibrium condition mediated by the forces generated by the surface tension force and the external electric force density[33]. In other words, an equivalence between a term F_γ, relative to the surface tension contribute, and a term F_e, relative to the electric external stimulus, has to be reached[35]. In this section the Taylor's cone equilibrium conditions will be examined summarily. These are at the basis of the phenomena involved in the pyro-EHD tools, explained in the following.

1.2.2 Surface tension

The surface tension is generically defined as the work exerted from the external ∂W to expand the liquid surface for a quantity ∂A:

$$\gamma = \frac{\partial W}{\partial A} \tag{6}$$

If the surface is curve, choosing the z axis as the direction of the force associated to the surface tension, γ can be written as:

$$\gamma = \frac{|\overline{F_Z}|}{A}\left(\frac{1}{R_{C1}} + \frac{1}{R_{C2}}\right)^{-1} \tag{7}$$

Where R_{C1} and R_{C2} are the curvature radii. In the case of a cone, as that showed in Fig. 1.4, $R_{C2} \to \infty$.

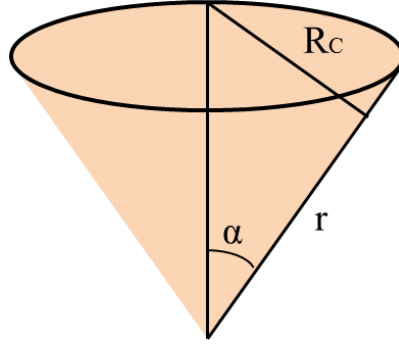$$\gamma = \frac{|\overline{F_Z}|}{A}R_{C1} = \frac{|\overline{F_Z}|}{A}\frac{r}{\cot\alpha} \tag{8}$$

13

Figure 1.4. Schematization of a Taylor's cone.

F_γ modulus could be defined as the normal force F_z per unit area A, so Eq. 8 can be also written:

$$\left|\bar{F}_\gamma\right| = \frac{|\bar{F}_Z|}{A} = \gamma \frac{\cot\alpha}{r} \tag{9}$$

1.2.3 Electric external forces

In order to evaluate F_e, the first step is the calculation of the electric force density $\bar{f}_e$. That term is linked to the Maxwell stress tensor $\bar{\bar{T}}$.

$$\bar{f}_e = \bar{\nabla} \cdot \bar{\bar{T}} \tag{10}$$

The derivation of $\bar{\bar{T}}$ follows two possibilities: the Kelvin method and the Korteweg-Helmholtz method[36-37]. These proposals consider magnetic fields as neglected and elementary dipoles as the model to describe the interaction between the fluid and the field. Moreover, the electric field is assumed independent from the mechanic pressure, i.e. electrostriction effects are neglected. By the Kelvin method, the total electric force density of Kelvin $\overline{f_{e,k}}$ could be decomposed in two contributes: one due to the charges bounded to the liquid molecules $\bar{f}_k$, associated to the tensor $\bar{\bar{T}}_k$, and another one due to free charges $\bar{f}_f$, associated to the tensor $\bar{\bar{T}}_f$[36]. $\bar{f}_k$ (also known Kelvin force polarization density) is evaluated considering $\bar{m}$ as the average electric dipole moment per unit of volume, which

14

is linear respect to the electric field, if the material is isotropic. An expression of $\bar{m}$ is:

$$\bar{m} = (\varepsilon - \varepsilon_0)\bar{E} \qquad (11)$$

where ε is the permittivity of the medium and ε_0 is the permittivity of vacuum. $\bar{f}_k$ depends on $\bar{m}$ and $\bar{E}$ through the formula:

$$\bar{\nabla} \cdot \overline{\overline{T_k}} = \bar{f}_k = (\bar{m} \cdot \bar{\nabla})\bar{E} = (\varepsilon - \varepsilon_0)(\bar{E} \cdot \bar{\nabla})\bar{E} = (\varepsilon - \varepsilon_0)\left[(\bar{\nabla} \times \bar{E}) \times \bar{E} + \right.$$

$$\left. \frac{1}{2}\bar{\nabla}(\bar{E} \cdot \bar{E})\right] = \frac{1}{2}(\varepsilon - \varepsilon_0)\bar{\nabla}(\bar{E} \cdot \bar{E}) \qquad (12)$$

being $\bar{\nabla} \times \bar{E} = 0$ for the Gauss theorem[38-39]. $\bar{f}_f$ can be expressed as:

$$\bar{\nabla} \cdot \overline{\overline{T_f}} = \bar{f}_f = (\bar{\nabla} \cdot \bar{D})\bar{E} \qquad (13)$$

where $\bar{D}$ is the charge displacement. Therefore, $\overline{f_{e,k}}$ is given by:

$$\overline{f_{e,k}} = \bar{f}_k + \bar{f}_f = \frac{1}{2}(\varepsilon - \varepsilon_0)\bar{\nabla}(\bar{E} \cdot \bar{E}) + (\bar{\nabla} \cdot \bar{D})\bar{E} \qquad (14)$$

Alternatively, the Korteweg-Helmholtz approach starts by the evaluation of electrostatic energy density W_E of a dielectric material, subjected to an electric field, and reaches the same results in terms of $\bar{f}_e$[36,40-41]. More precisely, the electric force density of Korteweg-Helmholtz $\overline{f_{e,kh}}$ differs from $\overline{f_{e,k}}$ for a quantity:

$$\overline{f_{e,kh}} - \overline{f_{e,k}} = -\nabla\left[\frac{1}{2}(\varepsilon - \varepsilon_0)\bar{E}^2 - \frac{1}{2}\rho\left(\frac{\partial\varepsilon}{\partial\rho}\right)_T \bar{E}^2\right] \qquad (15)$$

However, the term reported in Eq. 14 is associated to the electrostriction force, which is supposed to be negligible, then $\overline{f_{e,kh}} \approx \overline{f_{e,k}} \equiv \bar{f}_e$[36,41]. $\bar{F}_e$ is the total electric force acting on a volume V and is linked to $\bar{f}_e$ by:

$$\bar{F}_e = \iiint_V \bar{f}_e\, dV = \iiint_V (\bar{\nabla} \cdot \overline{\overline{T}})\, dV \qquad (16)$$

1.2.4 Equilibrium condition

Eq. 14 can be simplified considering the normal electrostatic component[37] and, applying Eq. 16, is possible to obtain an equation for $\bar{F}_e$ suitable to compare to F_γ in Eq. 9.

$$\gamma\frac{\cot\alpha}{r} = \frac{1}{2}\varepsilon_0 E_z^2 \qquad (17)$$

where E_z is the normal component of the electric field. Starting from the first two Maxwell's laws, $\bar{E}$ is linked to an electric potential φ:

$$\begin{cases} \bar{\nabla} \times \bar{E} = 0 \Rightarrow \bar{E} = -\bar{\nabla}\varphi \\ \quad\quad \bar{\nabla} \cdot \bar{E} = \dfrac{\rho}{\varepsilon_0} \end{cases} \Rightarrow \nabla^2 \varphi = -\dfrac{\rho}{\varepsilon_0} \tag{18}$$

where ρ is the density. In a cone with equipotential surface,

$$\nabla^2 \varphi = 0 \tag{19}$$

A generic solution of Eq. 17 is given by:

$$\varphi = k\tilde{Q}\sqrt{r}\cos\alpha \tag{20}$$

where $\tilde{Q}$ is the Legendre function and k is a constant. The equilibrium is reached when $\tilde{Q}$ is zero and this condition is achieved for $\alpha = 49.3°$. This value is the same empirically deduced by Taylor[33]. Nevertheless, this result assumes that there are no charges on the cone axis: that means the right solution is an angle slightly smaller[42].

1.3 Pyro-EHD effect

If the electric field that activates the EHD phenomenon is generated by a pyroelectric crystal, the combined effect is defined pyro-electro-hydro-dynamics (pyro-EHD)[43-50]. The possibility of manipulate liquids or polymeric solution exploiting pyro-EHD effect, without the use of electrodes, is investigated in the following sections. In this work, two different techniques that exploit the pyro-EHD effect have been used: the first one is based on the dispensing of micro- and nano-drops or micro-fibers, produced by a polymeric (eventually polymeric solution) reservoir placed at a certain distance from a pyroelectric crystal[43,45-47,50]; the second one consists on the self-assembling of polymeric micro-optical devices onto a micro-engineered lithium niobate LN[44,48-50]. The dispensing is guided by the pyroelectric field that induces a charge displacement on the liquid surface; the reservoir drop turns into a Taylor's cone shape, until the attractive (or repulsive) force exerted toward the crystal gets start the dispensing of drops or fibers, in order to produce drops arrays or patterns. The self-assembling depends on the pattern impressed onto a LN crystal through a poling treatment.

The field lines generated by this crystal induce the polymer to occupy precise positions onto the crystal.

References

1 Lang, S. B. *Sourcebook of Pyroelectricity.* New York: Gordon and Breach Science Publishers. (1974).

2 Lang, S. B. Pyroelectricity: From Ancient Curiosity to Modern Imaging Tool. *Physics Today*, (2005) 31-36.

3 Lovinger, A. J. Ferroelectric Polymers. *Science*, (1983) 1115-1121.

4 Whatmore, R. W. Pyroelectric Devices and Materials. *Report on Progress in Physics*, (1986) 1335-1386.

5 Kinzie, P. A. *Thermocouple Temperature Measurement.* New York: J. Wiley (1973).

6 Ramos, P., De Andres, A., and Lopez, S. Effect of Thermal Losses on the Specific Detectivity of Pyroelectric Infrared Detectors. *Integrated Ferroelectrics*, (2007) 147-159.

7 Lang, S.B. and Das-Gupta, D.K. *Handbook of Advanced Electronic and Photonic Materials and Devices*. Academic Press, San Diego, CA, (2001) 4.

8 Zhang, R., Jiang, B. and Cao, W. Orientation Dependence of Piezoelectric Properties of Single Domain $0.67Pb(Mn_{1/3}Nb_{2/3})O_3-0.33PbTiO_3$ Single Crystal. *Applied Physics Letters*, (2003) 82, 21, 3737‑3739.

9 Li, Z., Xu, Z., Xi, Z., Xiang, F. and Yao, X. Thermal Expansion Characteristics in [001]-Oriented PMN-0.32PT Single Crystals. *Ferroelectrics*, (2007) 355, 1, 245‑251, 2007.

10 Kumar, P., Sharma, S., Thakur, O.P., Prakash, C. and Goel, T.C. Dielectric, Piezoelectric and Pyroelectric Properties of PMN-PT (68:32) System. *Ceramics International*, (2004), 30, 4, 585-589.

11 Yasuda, N., Banno, T., Fujita, K., Ohwa, H., Matushita, M., Yamashita, Y., Iwata, M. and Ishibashi, Y. Piezoelectric Properties of Relaxor

Ferroelectric Solid Solution Single Crystals PMN-PT and PZN-PT Near MPB Under Pressures. *Ferroelectrics*, (2007) 347, 1, 44-49.

12 Batra, A. K., Guggilla, P., Currie, J. R., Aggarwal, M. D. and Alim, M. A. Pyroelectric Ceramics for Infrared Detection Applications. *Materials Letters*, (2006) 1937-1942.

13 Bauer, S., and Lang, S.B. Pyroelectric Polymer Electrets. *IEEE Transaction of Dielectrics and Electrical Insulation*, (1996) 56, 57‑62.

14 Chu, B., Zhou, X., Ren, K., Neese, B., Lin, M., Wang, Q., Bauer, F., and Zhang, Q.M. A Dielectric Polymer with High Electric Energy Density and Fast Discharge Speed. *Science*, (2006) 313, 5785, 334-336.

15 Sencadas, V., Lanceros-Mendez, S., and Mano, J.F. Characterization of Poled and Non-Poled *β*-PVDF Films Using Thermal Analysis Techniques. *Thermochimica Acta*, (2004) 424, 201-207.

16 Kouchachvili, L., and Ikura, M., Pyroelectric Conversion-Effects of P(VDF-TrFE) Preconditioning on Power Conversion. *Journal of Electrostatics*, (2006) 65, 182-188.

17 Olsen, R.B., and Bruno, D.A., Pyroelectric Conversion Materials. Proceedings of the 21st Intersociety Energy Conversion Engineering Conference, American Chemical Society, San Diego, CA, (1986) 89-93.

18 Olsen, R.B., Bruno, D.A., and Briscoe, J.M., Pyroelectric Conversion Cycles. *Journal of Applied Physics*, (1985) 58, 12, 4709-4716.

19 Safari, A., Panda, R. K., and Janas, V. F., Ferroelectricity: Materials, Characteristics & Applications. *Key Engineering Materials*, (1996) 35-70.

20 Lang, S. B., Bibliography on Piezoelectricity and Pyroelectricity of Polymers. *Ferroelectrics*, (1981) 191-245.

21 Fukada, E., Introduction: Early Studies in Piezoelectricity, Pyroelectricity and Ferroelectricity in Polymers. *Phase Transitions*, (1989) 135-141.

22 Varma, K.B.R., Morphology and Dielectric Properties of Fish Scales. *Current science*, (1990) 59, 8, 420-423.

23 Fedosov, S. N., and Von Seggern, H., Pyroelectricity in PolyvinylideneFluoride: Influence of Polarization and Charge. *Journal of Applied Physics*, (2008) 014105, 1-8.

24 Wong, C. P., Polymers for Electronic and Photonic Applications. Boston: Academic Press (1993).

25 Uchino, K., *Ferroelectric Devices.* New York: Marcel Dekker (2000).

26 Lines, M.E., and Glass, A.M., *Principles and Applications of Ferroelectrics and Related Materials*, Clarendon Press, Oxford, UK, (1977).

27 Itskovsky, M.A. Pyroelectric Hysteresis Loop at Ferroelectric Phase Transition, *Journal of Applied Physics*, (1999) 85, 4256-4258.

28 Ikura, M., Conversion of Low-Grade Heat to Electricity Using Pyroelectric Copolymer. *Ferroelectrics*, (2002) 267, 403-408.

29 Dietze, M., Krause, J., Solterbeck, C. H., and Es-Souni, M. Thick Film Polymer-Ceramic Composites for Pyroelectric Applications. *Journal of Applied Physics*, (2007) 54113, 1-7.

30 Zheng, D., Da-Gui, H., and De-Yin, Z. Thermal Analysis of the Microscale Pyroelectric Thin Film Infrared Detectors. *2008 IEEE International Conference on Mechatronics and Automation*, (2008) 49-54.

31 Lopez-Herrera, J., Popinet, S., and Herrada, M. A Charge-Conservative Approach for Simulating Electrohydrodynamic Two-Phase Flows Using Volume of Fluid. *Journal of Computational Physics*, (2011) 230.

32 Zeleny, J., Instability of Electrified Liquid Surfaces. *Physics Review*, (1917) 10, 1-6.

33 Taylor, G., Disintegration of Water Drops in an Electric Field. *Proceeding of the Royal Society*, (1964) 383-397.

34 Mizuno, Y., Fujii, O., Honsali, K., and Naito, K., Vibration of a Water Droplet on a Polymeric Insulating Material Subjected to AC Voltage Stress. *IEEE trans. on Dielectrics and Electrical insulation*, (2010) 17, 566-571.

35 Melcher, J., and Taylor, G., Electrohydrodynamics: a Review of the Role of Interfacial Shear Stress. *Annual Review of Fluid Mechanics*, (1969) 1, 111-146.

36 Melcher, J., Continuum Electromechanics. *MIT Press.*, (1981).

37 Landau, L., and Lifshitz, E., *Electrodynamics of Continuous Media*. Pergamon Press, (1960).

38 Hua, J., Lim, L. K. and Wang, C., Numerical Simulation of Deformation/Motion of a Drop Suspended in Viscous Liquids Under Influence of Steady Electric Fields. *Physics of Fluids*, (2008) 20, 1-16.

39 Saville, D., Electrohydrodynamics: The Taylor-Melcher Leaky Dielectric Model. *Annual Review of Fluid Mechanics*, (1997) 29, 27-64.

40 Jackson, J. D., Classical Electrodynamics 3rd edition. Wiley (1962).

41 Chen, C., Electrohydrodynamic Stability. Electrokinetics and Electrohydrodynamics in Microsystems. *International Centre for Mechanical Sciences*, (2011) 530, 144-220.

42 la Mora, J. F. D., The Fluid Dynamics of Taylor Cones. *Annual Review of Fluid Mechanics*, (2007) 39, 217-243.

43 Ferraro, P., Coppola, S., Grilli, S., Paturzo, M., Vespini, V., Dispensing Nano-Pico Droplets and Liquid Patterning by Pyroelectrodynamic Shooting. *Nature nanotechnology*, (2010) 5, 6, 429-435.

44 Merola, F., Paturzo, M., Coppola, S., Vespini, V., Ferraro, P., Self-Patterning of a Polydimethylsiloxane Microlens Array on Functionalized Substrates and Characterization by Digital Holography. *Journal of Micromechanics and Microengineering*, (2009) 19, 12, 125006.

45 Coppola, S., Vespini, V., Grilli, S., Ferraro, P., Self-assembling of Multi-Jets by Pyro-Electrohydrodynamic Effect for High throughput Liquid Nanodrops Transfer. *Lab on a Chip*, (2011) 11, 19, 3294-3298.

46 Vespini, V., Coppola, S., Todino, M., Paturzo, M., Bianco, V., Grilli, S., Ferraro, P., Forward Electrohydrodynamic Inkjet Printing of Optical Microlenses on Microfluidic Devices. *Lab on a Chip*, (2016) 16, 2, 326-333.

47 Grimaldi, I. A., Coppola, S., Loffredo, F., Villani, F., Minarini, C., Vespini, V., Miccio, L., Grilli, S., Ferraro, P., Printing of Polymer Microlenses by a Pyroelectrohydrodynamic Dispensing Approach. *Optics letters*, (2012) 37, 13, 2460-2462.

48 Vespini, V., Gennari, O., Coppola, S., Nasti, G., Mecozzi, L., Pagliarulo, V., Grilli, S., Carfagna, C., Ferraro, P., Electrohydrodynamic Assembly of Multiscale PDMS Microlens Arrays. *IEEE Journal of Selected Topics in Quantum Electronics*, (2015) 21, 4, 399-406.

49 Coppola, S., Nasti, G., Mandracchia, B., Vespini, V., Grilli, S., Pagliarulo, V., Pareo, P., Manca, M., Carbone, L., Gigli, G., Ferraro, P., Twofold Self-Assembling of Nanocrystals into Nanocomposite Polymer. *IEEE Journal of Selected Topics in Quantum Electronics* (2016), 22, 1, 1-7.

50 Olivieri, F., Todino, M., Coppola, S., Vespini, V., Pagliarulo, V., Grilli, S., Ferraro, P., Fabrication of Polymer Lenses and Microlens Array for Lab-on-a-Chip Devices. *Optical Engineering*, (2016) 55, 8, 081319-081319.

CHAPTER 2

POLYMERIC MICRO-LENSES OBTAINED BY PYRO-EHD EFFECT

2.1 Micro-lenses applications and conventional fabrication

2.1.1 Overview and soft lithography

Micro-lenses and micro-lens arrays are assuming an increasingly important role in optical devices and communication systems. They become key components of many optical devices, being useful for the imaging of very small structures. In response to their extended use in different fields of technology, a great emphasis is being placed on research into simple manufacturing approaches for these micro-optical components as well as on the characterization of their performance. Currently, in industrial applications, micro-lenses are used in a large range of fields, like laser printers[1] or communication systems[2], and can also be useful in the fabrication of electronic devices[3], such as three-dimensional (3-D) displays[4], optical data storage[5], solar cells[6], photodetectors[7], and for biological components. Numerous classes of micro-lenses exist, depending on the embedding technology and the specific applications[8]. An interesting property of micro-lenses consists of the possibility of tuning their focal length. In fact, many procedures have been applied for the assembly of arrayed tunable micro-lenses with a variety of materials[7]. The geometrical properties and the focal length of the lens array are easily modulated by controlling appropriate experimental parameters. In a general way, micro-lenses with variable focal length can be generated by actuation of liquid crystals or other liquids through electro-wetting (EW), electrophoresis, or hydrodynamic pressure[7]. However, in recent years, there is great interest in obtaining micro-lenses made of polymeric material, which makes their use very comfortable. In fact, polymer properties allow easy manipulation of the material, making it possible to use a large range of techniques for the fabrication of optical micro-lenses. Several techniques have been developed to make micro-lenses, using many materials and trying to keep production costs low, in order to support their spread and improve their properties. It is possible to

realize structures of variable dimensions, from millimeters to micrometers. Some of these techniques are included in the soft lithography approach, based on the use of soft materials (polymers) to realize patterns of lenses on an opportune substrate (generally made of another soft material). Through soft lithography, it is possible to realize micro- and nano-structures with great precision. For example, the steps required to obtain a polydimethylsiloxane (PDMS, $(C_2H_6OSi)_n$) stamp starting from a silicon (Si) substrate are explained in Fig. 2.1.
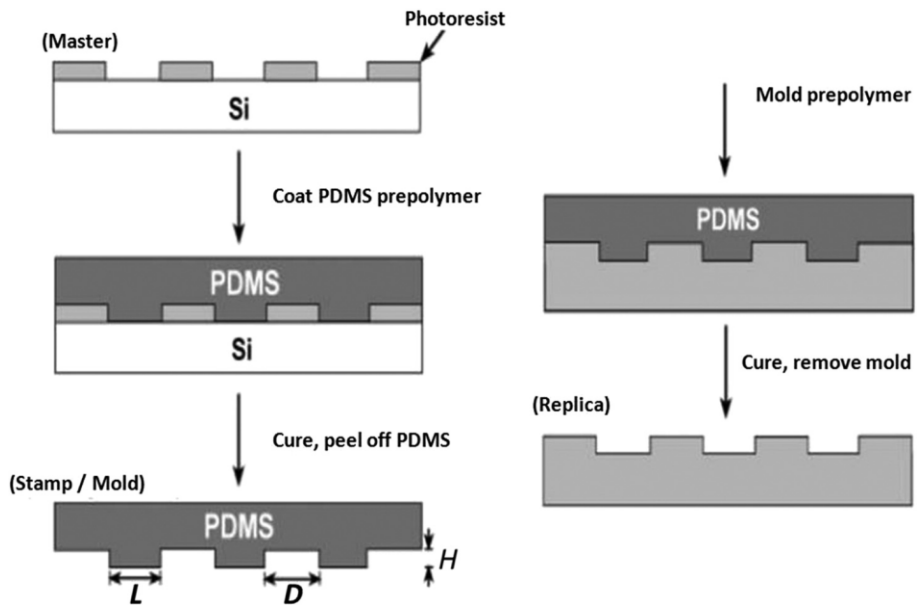

Figure 2.1. Steps to realize a PDMS stamp starting from a Si substrate[2].

First of all, the pattern transfer consists of the fabrication of a patterned master, through a deposition of a photoresist layer on a substrate. Once the pattern master is obtained, a pre-polymer is poured on the master, then molded to generate the stamp; therefore, it is made of the pre-polymer, which becomes rigid when it cures[9]. Other techniques based on the use of polymers are contact printing[10-11], replica molding[12-13], and imprinting (embossing)[14-15]. Keeping a suitable contact between the substrate and the mold, contact printing became an efficient and simple method for pattern transfer[16]. In fact, once the stamp is made, it is possible to create more samples that follow the pattern. Other advantages of this technique are the possibility to make an additive process, with a low waste of material and

to design a pattern with a large area. Contact printing is particularly indicated for two-dimensional (2-D) structures[10]. Regarding micro-lenses, this technique is particularly adopted for the realization of the mold that is used for the stamp of the lenses[12]. Replica molding[10,12-13] is so called because it is able to replicate one or more characteristics of the master, also in the case of 3-D structures in a nanometer resolution. Physics parameters that regulate the accuracy of a replica are wetting, Van Der Waals forces, and kinetic factors, like the filling of the mold[10]. Embossing is a technique that uses thermoplastic materials and imprints micro-structures in them. This technique has great potential to make features as small as 25 nm in silicon[14]. Some examples of this kind of fabrication are hot embossing[15], extrusion rolling embossing[17], gas-assisted ultraviolet (UV) embossing[18] and electromagnetic force-assisted UV imprinting[19]; all these works demonstrate that embossing is a good way to fabricate micro-lenses. Nevertheless, some of the methods described are expensive or require the use of clean-room facilities, reducing the selection of suitable materials[7]. Among these techniques, replica molding is probably the best: using a rigid PDMS stamp and, eventually, a substrate, the polymer in liquid form is deposited over the stamp and acquires the shape of the negative of the mold. The great advantage is related to the mold: if it is opportunely fabricated and dimensioned, an array of micro-lenses can be built with a single molding. An example is shown in Fig. 2.2 and consists of the fabrication of lenses using a polycarbonate (PC) substrate and a poly-metylmethacrylate (PMMA) solution deposited in the PDMS mold[12]. Starting from a PC substrate [Fig. 2.2(a)], a PMMA film is spin-coated on it, as shown in Fig. 2.2(b). Once the PMMA is cured, the PDMS is cast onto the PMMA film and another substrate (glass or plastic) is used to cover the system, as shown in Fig. 2.2(c). Once the PDMS is also cured, it can be easily stripped from the PMMA, allowing the micro-lens array[12] to be obtained, as shown in Fig. 2.2(d).
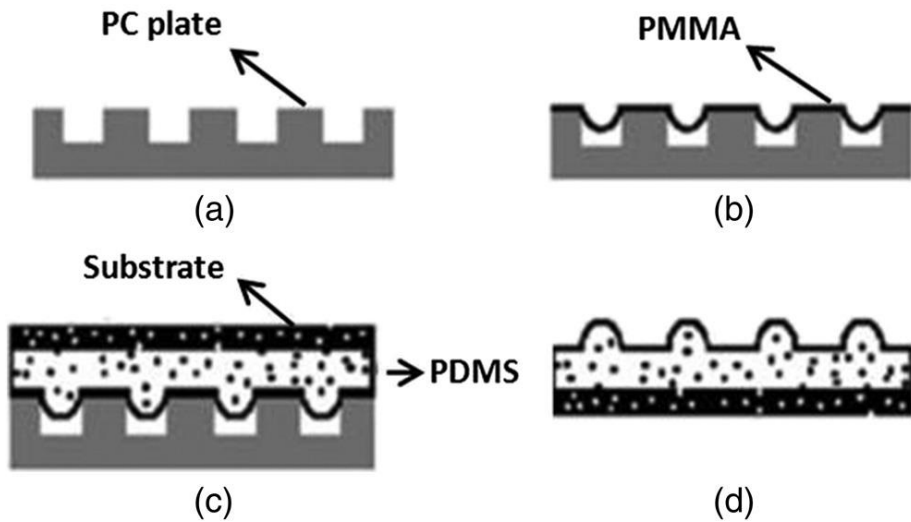
Figure 2.2. Fabrication of micro-lenses using a PC substrate (a) coated by a first layer of PMMA (b) and a second one of PDMS (c) in order to create a mold of micro-lenses (d)[12].

The lenses obtained, following the profile of the mold, can be defined as convex, but it is also possible to design lenses through a different mold profile to create a concave array[14], as shown in Fig. 2.3.
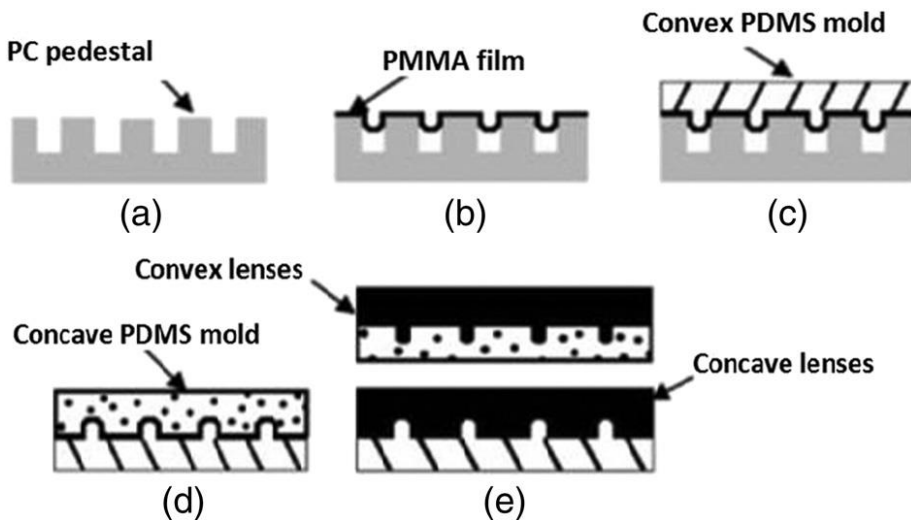

Figure 2.3. Fabrication of PMMA micro-lenses using a PDMS convex (c) and concave (d) mold, starting from a PC substrate[14].

Another option to make micro-lenses is through a replica molding that uses capillaries (also called micro-molding in capillaries). It exploits the viscoelastic properties of a polymer solution that, placed in a set of channels shaped from the PDMS mold, through capillary forces, can slide into the channels and acquire the shape marked by the mold[10,20]. Otherwise, micro-transfer molding exploits a system where the PDMS mold is in contact with a substrate and the pre-polymer is deposited between them: micro-lenses are obtained by eventually removing the excess polymer and heating the system to cure the polymer[21].

2.1.2 Electric field techniques

Very recently, various techniques have been presented and tested for the fabrication of micro-lenses. These techniques exploit electric fields and are focused on two phenomena: EW[15] and EHD[22-26]. EW is based on the study of the contact angle between a liquid and a substrate when an external electric field is applied[27]. The phenomenon can be also described through the interaction between two immiscible liquids and their behavior related to the forces applied by electric fields. The dynamic conditions of the system allow the evolution and the interaction between the liquids to be controlled, in turn controlling the meniscus' shape, forming lenses[28] and tuning their optical properties[29]. In fact, one of the biggest advantages of micro-lenses is the possibility to change the focus, modifying their shape by simply intervening on the radius of curvature[30-31]. An application of EW for the fabrication of micro-lenses is through the use of polymers that are reactive to UV rays[32]. The EHD, which has been already discussed in Chapter 1, includes all the interactions between two electrodes and a dielectric fluid placed between them that are due to an electric field generated by the two electrodes. The nature of the material allows manipulation by the action of the electric field; a non-uniform electric field applied on a dielectric particle generates the di-electro-phoretic (DEP) effect, and it is possible to fabricate micro-lenses through this phenomenon[33-35]. It is also possible to fabricate micro-lenses combining a soft lithography technique with EHD: e.g.,

through hot embossing to generate a polymer micro-pillar array and successive EHD reflowing to create a bifocal micro-lens array[23]. In this category, some systems based on ink-jet printing can be included (see Sections 2.2 and 2.3). A chance to use the electric fields is based on the use of pyro-electrical materials that show an electric answer under a thermic gradient and vice versa through EW[36-38] or exploiting EHD[24]. In particular, the combination between pyro-electric effect and EHD will be treated in the following and constitutes the center of this work. The attention will be mainly focused on an ink-jet printing approach will proposed for on-demand printing of lenses with high resolution and, on the other hand, on polymer molding and self-assembling for micro-lens arrays.

2.2   Pyro-Ink-Jet printing of micro-lenses

2.2.1 Ink-Jet printing: overview

An ink-jet printer makes use of tiny ink droplets to facilitate direct printing without the device coming into contact with the printed surface. Because of this technology enables non-contact printing, it can be applied to all kinds of materials[25-26,40-41] and it is now being introduced for use in a wide range of fields ranging from general purpose to industrial. Ink-jet printing has arisen from Rayleigh's idea, but only in 1951 was this method more widely adopted[39]. Ink-jet printing is divided into two categories: continuous and drop-on-demand. In particular, drop-on-demand could be activated through thermal [Fig. 2.4(a)], piezoelectric [Fig. 2.4(b)], acoustic [Fig. 2.4(c)], electrostatic [for instance, EHD (as depicted in Fig. 2.5)], and, very recently, pyro-EHD effects.
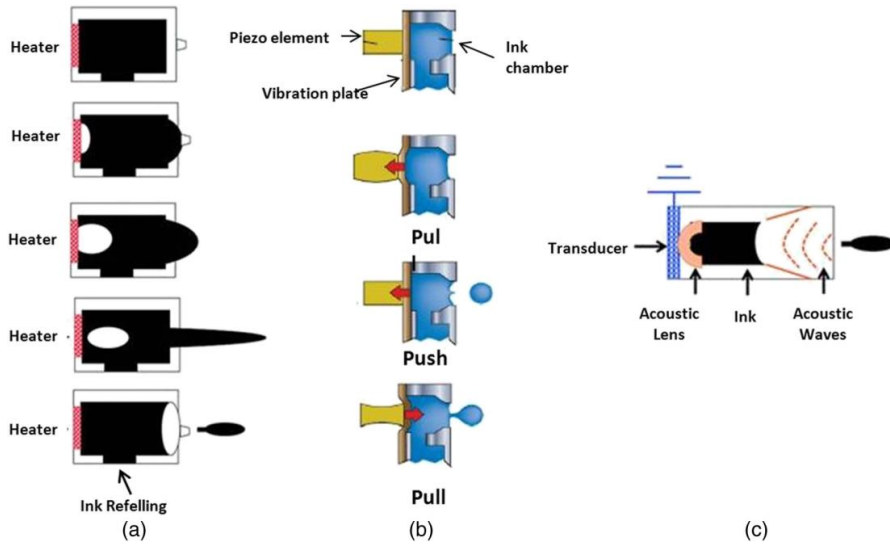
Figure 2.4. Drop-on-demand thermal ink-jet printer (a); piezo ink-jet printing system (b); acoustic printing (c)[39].
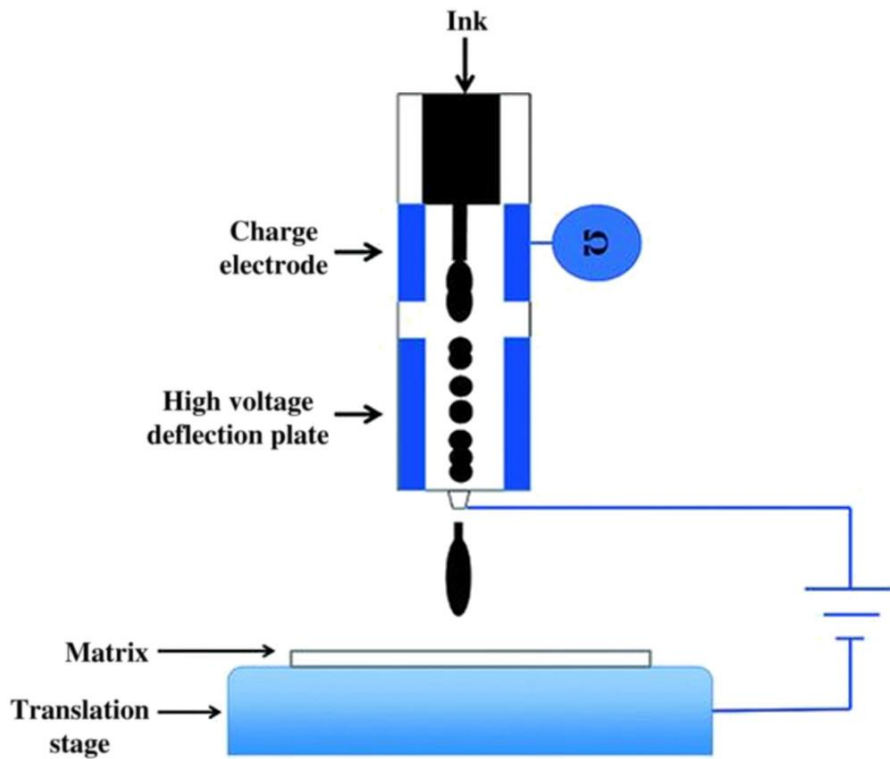

Figure 2.5. EHD ink-jet printer (single or multi-head).

The development of the thermal ink-jet printer was inspired by the natural process of water boiling to form water bubbles[39-41]. In this technology, the ink in a suitable chamber is rapidly heated to a high temperature to vaporize. The vaporization promptly creates a bubble at the surface of a heater (resistor), causing a pressure pulse to push the ink droplets out through the nozzle. As the ink droplets are ejected, the vapor bubble collapses, which generates a force to refill the ink[39-40]. The piezoelectric ink-jet exploits the inverse piezoelectric effect to work. The piezo-ceramic plate deforms in response to an electric impulse. This generates a pressure wave that causes the ink to be ejected from the nozzle. On the removal of the electric pulse, the ink is refilled as the piezo-ceramic plate returns to its normal shape[39]. In the acoustic printing, high-intensity sound beams can be used for ejecting droplets from a free liquid surface. This process is capable of producing drops as small as a few microns without the need for nozzles. A burst of acoustic energy focused to a diffraction-limited spot at a liquid surface can result in droplet ejection from the surface. This printer is made up of a piezoelectric transducer, an acoustic lens, and ink. When the piezoelectric transducer is excited, it makes sound waves toward the ink surface via an acoustic lens. The impact of the sound burst will cause a mound of liquid to rise from the surface due to the radiation pressure of the acoustic waves. If the energy of the incident sound beam is high enough, Rayleigh-Taylor instability will cause the top of the mound to neck down until a droplet breaks free. The droplet is expelled away from the surface at a velocity of several meters per second. After ejection, the surface relaxes as capillary waves generated near the mound propagate radially outward. Ejection droplets have been found to be very stable in size, velocity and directionality[42]. Moreover, between the techniques proposed, the setup used in the EHD printing method shown in Fig. 2.5 furnishes a flexible way to handle liquid and polymeric material on the micrometer and nanometer scale. This method allows manipulation of the liquid and polymeric materials by a non-uniform electric field[43-47]. In an electric field, an electric charge is induced on the surface of the meniscus of the ink and electrical stress stretches the meniscus

toward the direction of the field, drawing the meniscus of the liquid into a sharp cone from which charged liquid droplets are ejected when the electrostatic force exceeds the surface tension[40,43,46,48-49]. Between the types of EHD printing systems, there is also the EHD droplet ejection, based on the spray phenomenon. The EHD spray phenomenon (known as electrospray), shown in Fig. 2.6, is mainly focused on the liquid atomization mode.
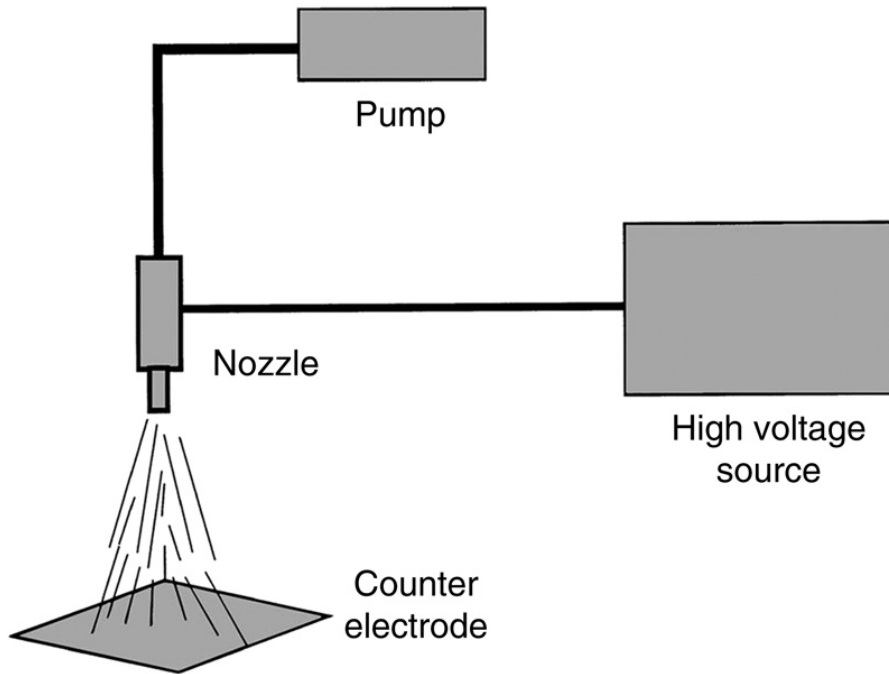

Figure 2.6. EHD spray phenomenon.

However, each of these techniques offers advantages and disadvantages. For example, thermal ink-jet printers are a low-cost option for printing at a fast speed with a high-quality finish. They can print on a wide variety of surfaces, including regular and specialty papers, plastics, metals and cartons. Most of these printers are simple to use and require no training or practice. But, in industrial applications, there are many problems with the high operation temperature. The thermal bubble, for instance, can be inclined to problems from the high operation temperature. As an alternative to thermal ink-jet printer, currently, the common use is a piezoelectric ink-jet printer. The piezoelectric print head, however, cannot

vary the size of droplets produced by a single nozzle; there is also a limit in terms of the nozzle dimensions for high-resolution patterns, as the size of the droplet is proportional to the size of the nozzle[39-40]. Furthermore, reducing the nozzle size to create micro-droplets requires a reduction in the size of the piezoelectric device, leaving it unable to create sufficient force to eject the droplets. Moreover, there are many limitations related to the use of the ink because the pressure caused from the vibration of the piezoelectric device is insufficient to eject highly viscous ink[40] and the cost of the piezoelectric print head and of the associated software (that directs the head to apply certain droplets of ink per dot) is considerable[39]. EHD ink-jet printing is, instead, a one-direct printing technology that overcomes the drawbacks of conventional piezoelectric ink-jet printing, which includes the use of highly viscous ink and nozzle-clogging problems. The most attractive advantage is that EHD printing technology generates a droplet much smaller than the nozzle size so that high-resolution printing is possible[25,44].

2.2.2 Pyro-EHD printing

2.2.2.1 Pyro-EHD printing standard working

As already said, the EHD printing system requires a high voltage supplier and exploits a non-uniform electric field to move a liquid or polymer material from the nozzle to the target substrate[43,45,47]. This configuration involves the choice of a low viscous liquid (to not obstruct the nozzle) and restricts the distance between the electrode and the counter electrode (about hundreds of microns), in order to achieve high accuracy[46]. The closest consequence is the limitation in placing a substrate between the nozzle and the electrode, making very difficult the direct printing on devices having millimetric thickness (such as commercial microfluidic channels). In order to evolve the system, the research has moved toward the overcoming of the nozzle limitations[50]. Pyro-EHD printing is a technique which does not provide nozzle, exploiting a liquid drop reservoir which is deformed, due to EHD effect, activated by a pyroelectric field[8,26,51]. More

specifically, local pyroelectric forces, activated by scanning a thermal source over an LN substrate, draw liquid droplets from the reservoir and deposit them on a target substrate[26]. Moreover, this process does not require complicated electrodes or a high-voltage circuit to work and allows to use polymers having a larger range of viscosity. This method is a simple way to draw attolitre liquid droplets with high spatial resolution. One of the materials that could be used for the activation of the EHD effect is the pyroelectric LN. In general, the experimental setup of EHD printing is made up of three elements, essentially: a starting drop, a substrate that intercepts the dispensed drops on demand and a source of electric field. As shown in Fig. 2.7(b), the system is simplified with respect to the conventional ink-jet apparatus [Fig. 2.7(a)] and could be mounted in a dynamic [Fig. 2.7(c)] or static [Fig. 2.7(d)] configuration.
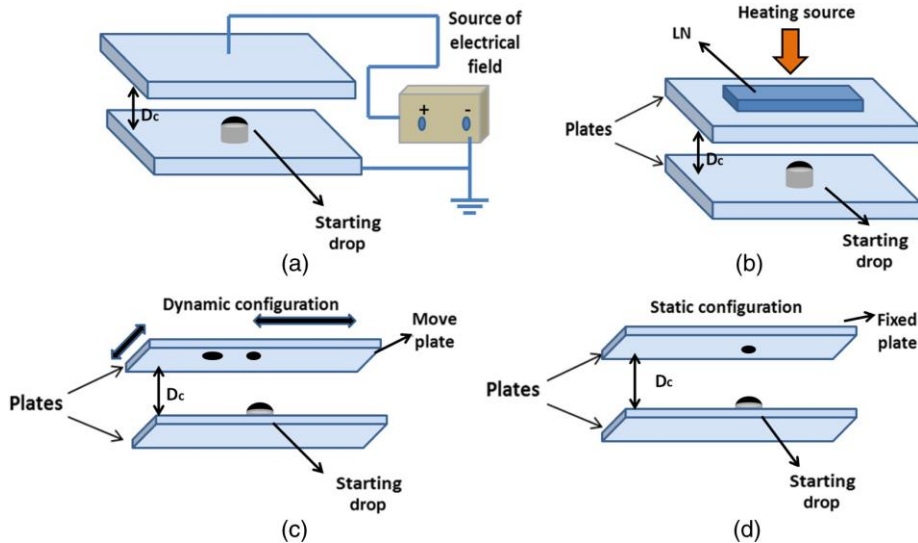

Figure 2.7. Generic setup (a); pyro-EHD setup (b); dynamic configuration (c); static configuration (d).

In both cases, the upper plate is constituted, e.g., of a microscope coverslip used as receiving substrate, placed on a three-axis translation stage, while the LN crystal drives the process. In the static configuration, the collector is fixed in space so that the reservoir drop can dispense multiple jetting in the same position,

increasing the dimension in terms of volume and the geometric characteristics of the deposited droplet. On the other hand, a more interesting configuration is related to the continuous printing of separate droplets controlling the movement of the target substrate with high-precision motorized positioners. The distance between the two plates is set on the scale of hundreds of microns depending on the investigated base drop[8,26,51-52]. It is well known that for a fixed drop volume, a critical value D_C can be defined for the distance D between the base and the substrate, according to the following expression:

$$D_C = \left(1 + \frac{\vartheta}{4}\right) V^{\frac{1}{3}} \tag{21}$$

where ϑ is the contact angle and V is the volume of the drop reservoir. A stable liquid bridge is established when $D < D_C$. The most relevant case here refers to $D > D_C$, when an unstable liquid streaming regime occurs. We use such an instability to break up the liquid reservoir and to dispense droplets[8,26]. A video camera is used to monitor the printing process; the light coming from a collimated LED light source (Thorlabs M470L2) illuminates the cross-section of the dispensing system, thus is collected by a 10× microscope objective and, finally, projected onto a CMOS camera (Motion ProY3-S1).

2.2.2.2   Micro-lenses   fabrication   through   pyro-ink-jet printing

The fabrication of micro-lenses with pyro-EHD could be accomplished in various ways: by the spontaneous breakdown of an unstable matter bridge created through the pyro-EHD effect[8]; with a dispensing process[26,52]. The spontaneous breakdown of an unstable polymer bridge can be explained in this way: for a fixed volume drop [Fig. 2.8(a)], when the stable liquid bridge is formed [Fig. 2.8(b)], it is possible to separate the plates at a certain distance and obtain the micro-lenses, as shown in Fig. 2.8(c).
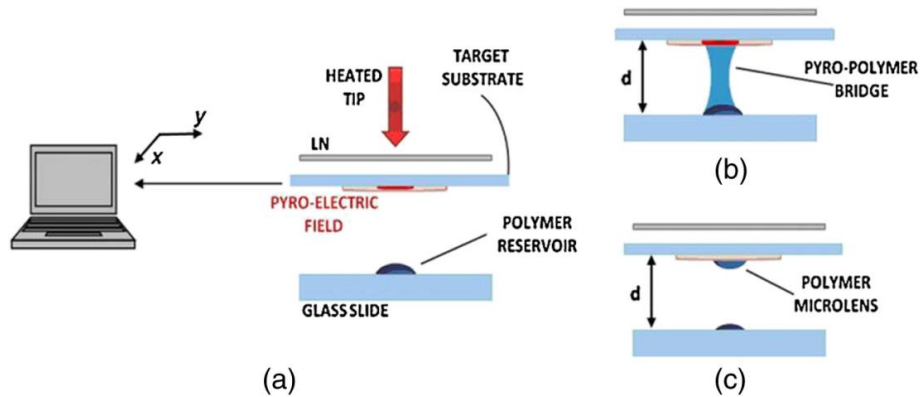
Figure 2.8. Scheme of the printing system (a) consisting of a LN plate, a heat source, and a drop reservoir, formation of the pyro-polymer bridge of the polymer micro-lens (b) and the translating target substrate (c)[8].

As disclosed, if the distance is $d > D$, it is possible to create lenses by the dispensing process. A pointwise thermal stimulus is applied to the LN crystal to induce the pyro-electric effect locally. At equilibrium, spontaneous polarization P_S of the LN crystal is fully compensated by the external screening charge and no electric field exists. The electric field exerts an attractive force on the liquid and, when sufficiently strong, deforms the liquid into a conical tip from which a thin liquid jet is released[26,51]. This liquid jet is intercepted by a target substrate (Fig. 2.9), and micro-lenses are generated.
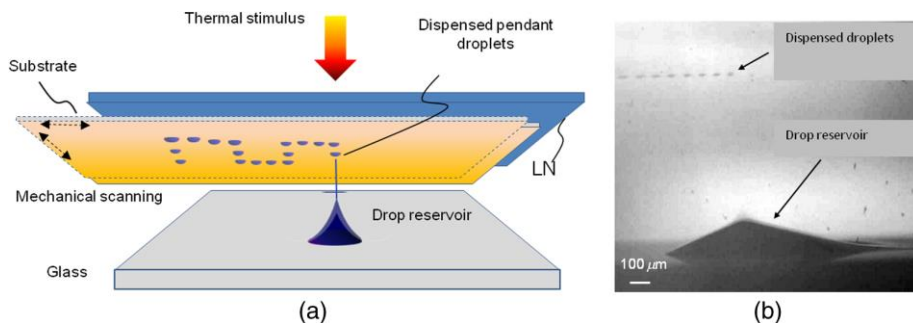

Figure 2.9. Dispensing nano-liter droplets for liquid patterning (a): liquid is dispensed onto a translating substrate inserted between the LN and the glass plate. Side view of the typical printing functionality (b).

2.2.2.3   LN stimulation by CB-layer

A chance to extend the electric field area is the use of a carbon black (CB) layer; in fact, this layer allows one to obtain a uniform heating upon the LN crystal. The use of a CB-layer reduces the recombination of the temporary surface charges and decreases the heat transfer from the crystal to the air, thus increasing the temperature gradient and improving the pyroelectric efficiency[52]. The fabrication process used to produce a nano-composite coating to be applied on the surface of LN crystals is shown in Fig. 2.10.
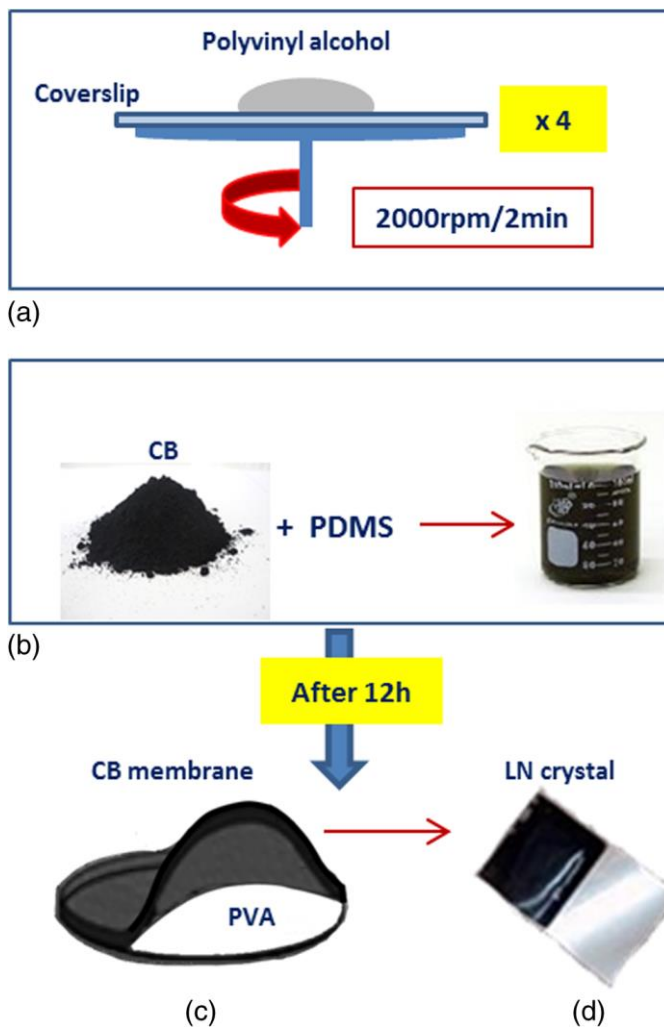

Figure 2.10. Schematic diagram of the CB deposition process[51].

The method consists of the preparation of a PDMS/CB film on polyvinyl alcohol (PVA)-coated glass substrate, followed by its peeling from the substrate and by the subsequent application of the resulting PDMS/CB membrane directly at a later stage to the crystal. In detail, the glass substrate, a microscope coverslip, is functionalized by spin-coating a PVA solution (2.8% in water) at 2000 rpm for 2 min. This step is repeated four times to produce a film thick enough to allow the easy peeling of the membrane [Fig. 2.10(a)]. Then, a CB suspension is prepared in PDMS [Fig. 2.10(b)] by adding 0.02 g of CB (graphitized CB-carbon nano-powder, size <200 nm, >99.95%) in 0.5 g of PDMS curing agent (Dow Corning Sylgard 184; 10:1 pre-polymer to curing agent) and sonicating it for 2 h. A drop of the suspension obtained after adding the elastomeric base to the solution is finally deposited on the top of the PVA-coated coverslip and cured at room temperature for 12 h. Once the CB membrane is peeled off the coverslip [Fig. 2.10(c)], it is set down on the crystal [Fig. 2.10(d)]. An illustration of the setup integrated with the CB-layer is reported in Fig. 2.11.
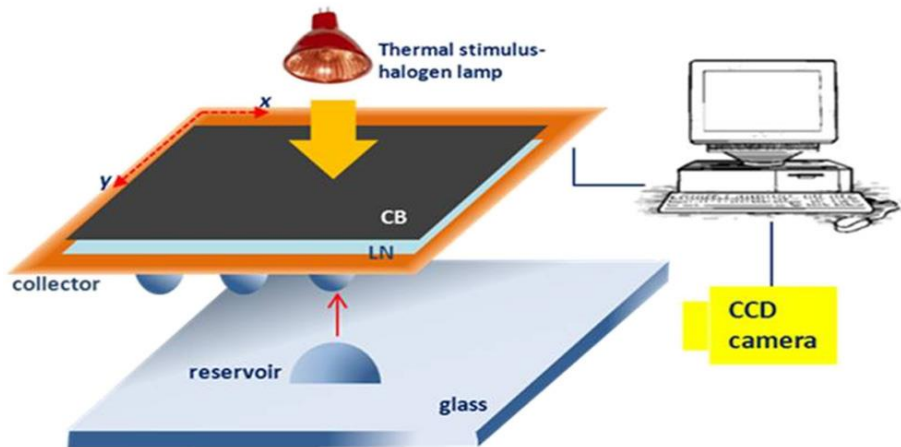

Figure 2.11. Pyro-EHD setup using the halogen lamp as the heating source[52].

Depending on the material of the starting reservoir drop, the dynamic and jetting evolution could be different. The geometry of electric field lines, as shown in Fig. 2.12, plays a fundamental role in the process: the plots of electric field lines for

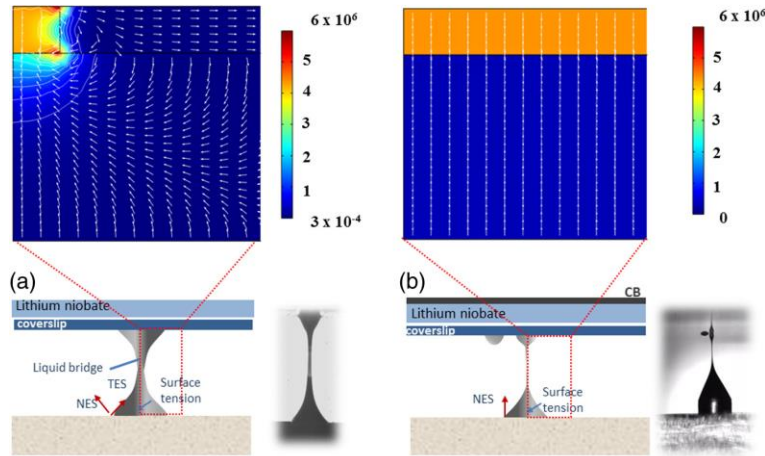localized heating and for uniform heating with a CB-layer are shown in Fig. 2.12(a) and 2.12(b), respectively.

Figure 2.12. Images of the PDMS-based reservoir drop deformation obtained by standard pyro-effect configuration (a) and innovative pyro-effect configuration employing a CB coating (b). In case (a), the starting polymer drop assumes the shape of a liquid bridge and experiences both normal and tangential components of the stress tensor while introducing a CB coating; (b) the pyro-effect is enhanced so that the polymer drop deforms into a sharp and elongated printing cone under the action of the tangential components[52].

It can be noted that when a CB layer is used, the electric field is very uniform over a large area, thus affecting the geometry of the dispensing process. The thickness of the CB-layer is about 200 μm; this value is the result of an easy method of preparation and peeling of a uniform CB membrane balanced with the radiation absorption value for the activation of the pyroelectric effect. As explained in Chapter 1, the EHD force generated at the air-polymer interface can be represented by a stress tensor, with normal and tangential components. In Fig. 2.12(a), under the influence of the pyroelectric field, the air-polymer interface moves dynamically, while in the case of Fig. 2.12(b) it appears uniform and experiences a stress tensor with a single component. In this case, once the

pyroelectric field is applied, the top polymer surface moves progressively upward with a spatially non-uniform geometry; the elongated cone experiences a greater EHD force over a small distance, thus leading to the activation of the upper surface and to the formation of a thin polymer tip. The electric field generated by the LN crystal is able to exert hydrodynamic pressure on the reservoir liquid, leading to the formation of a bridge or a conical tip that is a similar to the Taylor's cone[26,53]. The materials tested and used to make micro-lenses are PMMA and PDMS with different viscosities (PDMS: 3500 cps, PMMA: 560 cps). 200 mg/mL of PMMA (MW = 120000 amu) are dissolved in N-Methyl-pyrrolidone (NMP), while PDMS is used without any additional solvents. PMMA and PDMS are chosen for their good optical and mechanical properties and the lenses are fabricated onto a highly hydrophobic substrate made from a tetraethyl orthosilicate 1H,1H,2H,2H-perfluorodecyltriethoxysilane (TEOS/PFTEOS) film, deposited on a glass substrate. The substrate is prepared as described in the following procedure: a commercial glass (Corning Eagle 2000) is used as the substrate and cleaned by a standard procedure, applying in sequence sonication with detergent in boiling water for 2 h, acetone and isopropyl alcohol and drying under nitrogen flow. A sol-gel solution is prepared by mixing TEOS, PFTEOS, ethanol, deionized water, and concentrated hydrochloric acid (HCl). Before deposition, this solution is diluted with fluoro-propanol and then filtered. The use of fluoro-propanol is aimed at enhancing the wetting of the solution-substrate system so as to improve adhesion. The solution prepared is spin-coated (1000 rpm for 30 s) by means of a Brewer Science Model 100 spin-coater, successively baked on a hot plate at 100°C for 30 min to remove residual solvent and gradually heated from 110°C to 150°C for thermal curing. Finally, the film is kept in an oven at 150°C for one night. The thickness of the TEOS/PFTEOS film is 280 nm and the contact angle exceeded 100 deg[54]. Once the lenses are fabricated on the target of interest, the substrate is placed onto a hot plate at 100°C for 15 min and at 150°C for 15 min, thus inducing rapid heating of the sample. The subsequent sudden cooling solidifies the PDMS lenses that are therefore ready for being characterized[55].

2.2.3 Forward pyro-EHD printing configuration

The flexibility of EHD printing systems is one of the principal turning points in the research on this field. Pyro-ink-jet printing overcomes some limitations, as reported in Section 2.2.2.1. However, the geometrical configuration of pyro-ink-jet printer constrains to put the target substrate between the drop reservoir and the pyroelectric crystal. This necessity is the same in classical EHD printing configuration, wherein the target substrate is placed between the nozzle and an electrode. That causes limitations in terms of geometrical characteristics of the target substrate, making more complex the direct dispensing or the functionalization of devices. Laser-induced forward transfer (LIFT) offers a good solution, but the system is very complex[56-57]. Forward pyro-ink-jet printing configuration works placing the reservoir drop in contact with the pyroelectric crystal and the dispensing exploits the repulsive forces generated by the interaction between the liquid surface charge accumulation and the electric field[58]. In Fig 2.13 is showed the evolution of the EHD printer setup, from the classic EHD printer, to EHD conical tip dispenser, classic pyro-EHD printer configuration and forward pyro-EHD printer.
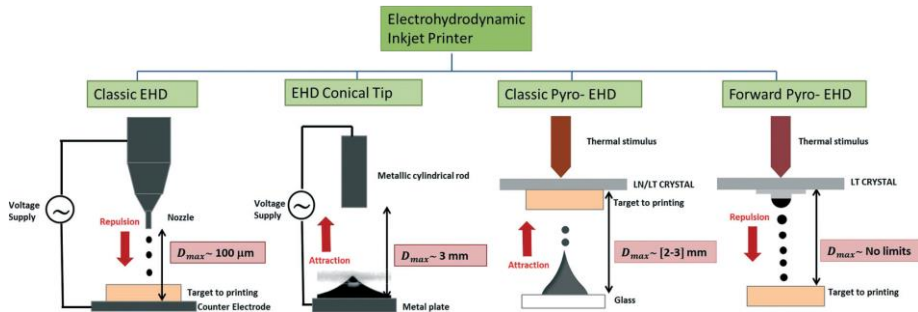

Figure 2.13. EHD ink-jet printers: evolution of the setup. Classic EHD setup has nozzle and electrodes; these limitations are progressively overcome with pyro-EHD printers.

In this way, with forward pyro-EHD dispenser, the limit imposed by the target substrate thickness is completely overcome (Fig. 2.13). This setup allows the

printing of liquid shots with high resolution, independently by the distance between the starting drop and the receiving substrate. The dispensing quality is also independent by the chemical nature of the substrate and the kind of material chosen for printing. In the next section, a published paper based on the forward pyro-EHD technique in reported. Printed micro-structures realization and characterization is showed and, moreover, the flexibility of the setup is demonstrated, functionalizing a commercial micro-fluidic device.

2.3 Paper: "Direct Fabrication of Polymer Micro-lens Array"

Authors and affiliations

Sara Coppola[a], Vito Pagliarulo[a], Veronica Vespini[a], Giuseppe Nasti[a], Federico Olivieri[a,b], Simonetta Grilli[a] and Pietro Ferraro[a]

[a] Institute of Applied Sciences and Intelligent System- CNR, Via Campi Flegrei 34, Pozzuoli (NA), 80078, Italy.

[b] University of Naples Federico II, Department of Chemical Materials and Production Engineering, Piazzale Tecchio 80, Naples 80125, Italy.

2.3.1 Abstract

In order to break the rigidity of classic lithographic techniques, a flexible pyro-EHD ink-jet printing is presented. In particular, here is showed a method able to manipulate highly viscous polymers, usable for optical integrated devices. The system proposed reaches spatial resolution up to the nano-scale and can print, for instance, nano-particles and high viscous polymer solutions. This technique allows writing patterns directly onto a substrate of interest in 2D or in 3D configuration and is studied in order to overcome limitations in terms of type of materials, geometry and thickness of the substrate. In the present work, we show the potential of pyro-EHD printing in fields as optics and micro-fluidics. A micro-channel chip is functionalized with a PDMS-made micro-lenses array, directly printed on the chip. The geometric properties and the quality of the lenses are evaluated by a Digital Holography (DH) analysis.

2.3.2 Introduction

Polymer-made micro-structures are useful for a large number of applications ranging from the integral imaging for 3D displays and optical communication, to OLEDs and high-resolution imaging[13,59]. A great variety of techniques answers to the necessity to manufacture these micro-optical components and to characterize their performances. Between them, as already said, there are hot embossing, soft replica molding, rapid laser-based patterning, ink-jet printing, and UV-nanoimprint lithography. Anyway, some of these methods have limitations: they could be expensive, require the use of clean-room facilities or highly trained staff with a limited selection of suitable materials. One of the most used structures in optical applications are micro-lenses[13,59]. A micro-lenses property that raises enormous interest would be the tunability of their focal length[54]. Therefore, in order to varying geometric and optical characteristics of the micro-lenses, such as their tunability, many procedures have been developed. For instance, swellable polymer micro-lenses, upon exposure to solvents, create

a tunable range of focal lengths, or also the generation of micro-lenses by virtue of the photo-polymerization, wherein the employment of a surfactant has broadened the range of substrates for the micro-lens formation. Recently, exploiting EHD phenomenon to manipulate polymeric solutions, new direct methods have been proposed for the micro-lenses arrays fabrication[8,26,60]. Here, we present a simple multiscale process able to fabricate micro-lenses arrays, using the pyro-electric effect activated onto a Lithium Niobate (LN) crystal and high viscous polymer materials[58]. Specifically, this method is driven by the pyro-electric field, activing the EHD pressure through the application of a temperature gradient. This technique, known as pyro-EHD inkjet printing, guarantees high resolution in terms of microns, representing a competitor with conventional soft lithography techniques. Micro-lenses produced here have a diameter dimension in a range between 25 and 500 μm and have high degree of uniformity. Additionally, pyro-EHD printing allows to write directly onto a substrate of interest. In this work, a micro-lenses array has been printed and characterized onto a micro-fluidic chip. In particular, the micro-lenses optical behavior is studied in terms of the optical aberrations, intrinsically present in a lens as an optical tool, by digital holographic microscopy (DHM).

2.3.3 Pyro-EHD printing: setup evolution

In Chapter 1 it has been explained that pyro-electricity is the property of certain materials to generate an electric potential onto their surfaces[26,50,61]. In this work, a LN (*z*cut and 500μm thick) crystal is used and a thermal stimulus produces a pyro-electric field onto its surfaces. In LN this effect is due to the movement of the lithium and niobium ions relative to the oxygen layers[62-63]. Furthermore, if that field is quite strong, it can generate forces able to induce an instability into fluids and polymer films[64-65]. Recently, we developed a pyro-EHD printing system free from nozzles and electrodes based on pyro-electric effect[64]. In Fig. 2.14 is represented the set-up realized for classic pyro-EHD printing.
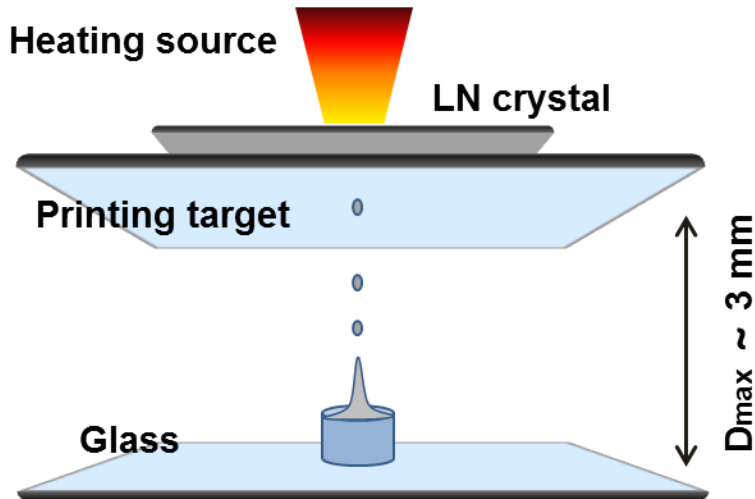
Figure 2.14. Classic Pyro-EHD setup configuration where the maximum distance between drop and receiving-substrate is 2-3 mm.

There are three macro-systems composing that setup: a heating system, a moving stage system and a monitoring system. The heating source is in contact with an auxiliary plate of LN wafer. The liquid reservoir is arranged on a glass substrate in front of a second glass substrate, representing the receiver-substrate mounted onto a three axes translation stage, in contact with the LN crystal and on the same line of the heating source. The moving stage system is made up of a high precision linear motor, with an X-Y axis (SGSP26-100(XY) SIGMA KOKI CO., LTD.) and a digital motion controller (SIGMA KOKI CO., LTD.). Through this system, a speed of 30 mm/s is achievable. The monitoring system consists of a highly-sensitive and fast camera (uEye, USB 3.0, a resolution of 2048 x 2048 pixels), an optical zoom lens and a blue LED light source (Thorlabs M470L3, wavelength of 470 nm and beam power of about 650 mW). This last system is used in order to monitor the cone-jet mode and jetting status. The major limitation of this configuration was the restriction of the distance between the droplet and the LN crystal: liquid reservoir could not be so far from the crystal, i.e. the pyro-electric field. Inducing a consequent limitation on thicknesses and geometric constrain of the receiving substrate. The problem of the distance is exceeded in the novel

configuration proposed in this paper: the novelty consists in the placement of the receiving substrate now in front of the drop reservoir and of the crystal (Fig. 2.15).
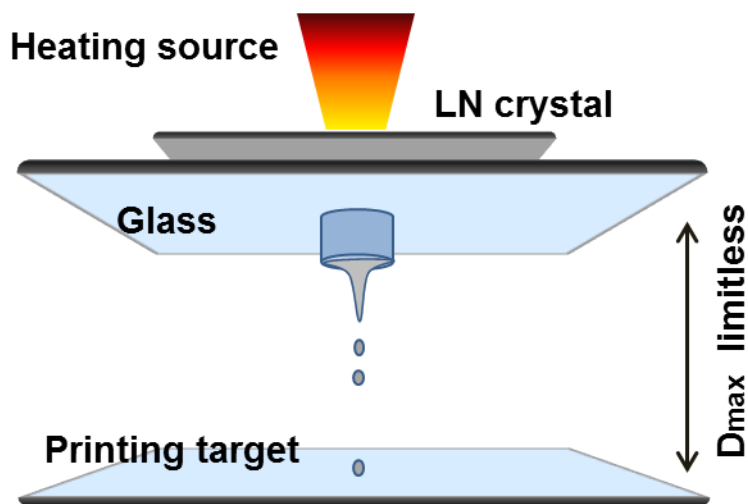

Figure 2.15. Novel Forward Pyro-EHD configuration where the maximum distance is limitless.

Comparing Fig. 2.14 and Fig. 2.15, is clear that the difference between the two configurations is in the placement of the liquid reservoir that is now in contact or in proximity of the LN. The receiver-substrate is in front of the liquid reservoir and the LN crystal. Specifically, the liquid drop is mounted onto a polymeric base, previously realized, in order to improve the uniformity of the drop. This base is in contact with a glass substrate. The LN crystal is locally heated, in particular in the area where the placed liquid drop is in contact with the crystal. Once the field is activated, it polarizes the fluid, exerting a repulsive force on the drop and, when it is strong enough, deforms the liquid into a conical tip (Taylor's cone)[26,53,66-67]. The drop releases micro-droplets, used for direct printing onto the moving substrate. The great advantage of this technique consists in the possibility of direct writing micro-drops onto a device, used as the receiving-substrate. In fact, pyro-EHD printing allows to realize high resolution samples, keeping good

precision during the printing process, fine spatial resolution onto a very large could be obtained. Moreover, several kinds of inks could be used through pyro-EHD printing. 3D structures directly printed onto devices of interests have applications, for example, in micro-optic technology. Optical micro-lenses are actually incorporated into commercial systems and scientific fields, such as optoelectronics, photonics and imaging process[53-54,67].

2.3.4 3D PDMS micro-lenses onto micro-fluidic chip

The integration of polymeric micro-lenses onto a commercial microfluidic PMMA-made channel (ChipShop GmbH) is the object of the work. Pyro-EHD printing is a key to develop integrated lab-on-a-chip (LoC) devices: this technique is able to fabricate micro-lenses, guaranteeing high chemical compatibility, good optical characteristics and flexibility in the design of the realized devices. PDMS (Dow Corning Sylgard 184, 10:1 mixing ratio, base to curing agent Midland; η = 3900 cP, εp = 2.65 from datasheet) is the polymer chosen for the fabrication of micro-lenses, being very powerful in optical applications. Moreover, in order to deposit PDMS onto the PMMA substrate, PDMS high adhesion and rapid curing make it an excellent candidate for this application. A fluorosilane agent (Fluorolink S10, Solvay Solexis) is used to modify the substrate wettability; in this way, the control on the geometrical features of the micro-lenses is improved. The contact angle between PDMS and fluorosilane-covered PMMA is ~ 40°. Moreover, the antireflection properties of fluorosilane guarantee good optical properties for the final realized device. Furthermore, fluorosilane have good chemical resistance and endures abrasion. Fluorosilane preparation follows the producer's procedure: the mixture consists of 98.8 wt% of isopropyl alcohol, 0.2 wt% of acetic acid (used to start the catalysis in the reaction), 0.8 wt% of deionized water and 0.2 wt% of Fluorolink S10. The reaction is complete in one day. In order to improve the link between the fluorosilane agent and the PMMA substrate, a O_2 plasma treatment (made through Femto System, Diener Electronic GmbH & Co. KG, Ebhausen, Germany) is done on the channel. This treatment

"actives" PMMA surface, increasing its chemical reactivity. Moreover, plasma treatment is also used to clean the substrate. The reaction between PMMA and the fluorosilane is completed after 1 h; in fact, the sample needs 30 minutes to complete the hydrolysis of siloxane groups and, then, it is heated at $T = 80\ °C$ for 30 minutes, in order to cure the material. Micro-lenses fabrication is done using the forward Pyro-EHD printing configuration, showed in Fig. 2.15. First of all, a PDMS drop, used as a reservoir, is deposited on a polymer pillar in proximity with the LN crystal. Once the heating source induces the temperature gradient onto the LN, the PDMS drop starts to deform itself and assumes a conical shape, known as Taylor's cone, dispensing micro- nano- and pico-drops. Fig. 2.16 shows a scheme of a micro-fluidic channel with PDMS micro-lenses pyro-ink-jet-printed on it. Micro-lenses can have different shapes and dimensions[26,54] and are formed using a XY axis stage, controlled by a computer. Once the lenses are deposited on the channel, the device is heated at 80 °C for 30 minutes, in order to improve the reaction between the base and the curing agent into the PDMS and make it solid.
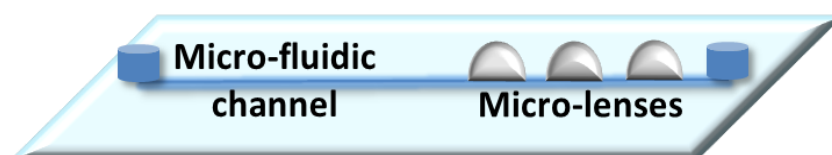

Figure 2.16. Schematization of a device with printed PDMS micro-lenses onto a PMMA-made micro-fluidic channel.

We have already demonstrated that pyro-ink-jet printing is a powerful technique for a large variety of materials[58]. Moreover, pyro-ink-jet printing allows to realize polymeric lenses arrays with a great control of their dimensions[58]. As shown in Fig. 2.17(b), a characterization of micro-lenses dimensions has been done, considering a PDMS micro-lenses array [four of these lenses are showed in Fig. 2.17(a)] printed onto a hydrophobic-treated glass. This treatment is done spinning

TEOS/PFTEOS onto the glass, in order to minimize the contact angle between the glass and the PDMS and obtain lenses with higher focal length.
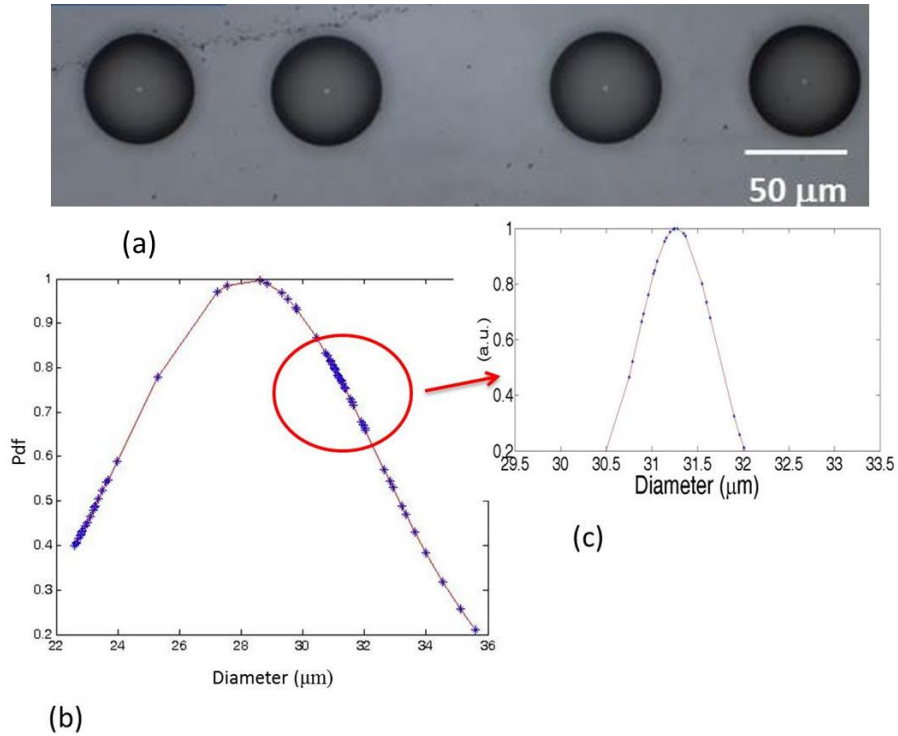

Figure 2.17. A short segment of a PDMS micro-lenses array is showed in (a). Randomly chosen micro-lenses dimensions are reported in (b) and (c). In particular, mean value measured is 28.55 µm, with a standard deviation of 4.91 µm (b). Focusing onto a region with more comparable values (c), mean value is 31.27 µm and the standard deviation is 0.42 µm.

The optical qualities of the micro-lenses have been evaluated through the Digital Holography (DH)[55]. In particular, optical aberrations and focusing properties of the micro-lenses have been studied. The set-up used is a classic Mach-Zehnder interferometer (Fig. 2.18): the object beam crosses the device and recombines to the reference one in the acquisition plane. In this way, an interference pattern is created and a digital hologram is recorded. Then, numerical propagation gives the object complex field in whatever plane along the optical axis from which the

phase distribution and the intensity of the optical wavefield transmitted by the sample can be extrapolated[68]. In order to compensate for the aberrations of the optics in the set-up, due to the phase delay relative to the cross of the object beam through the micro-fluidic channel, a double exposure method is done.
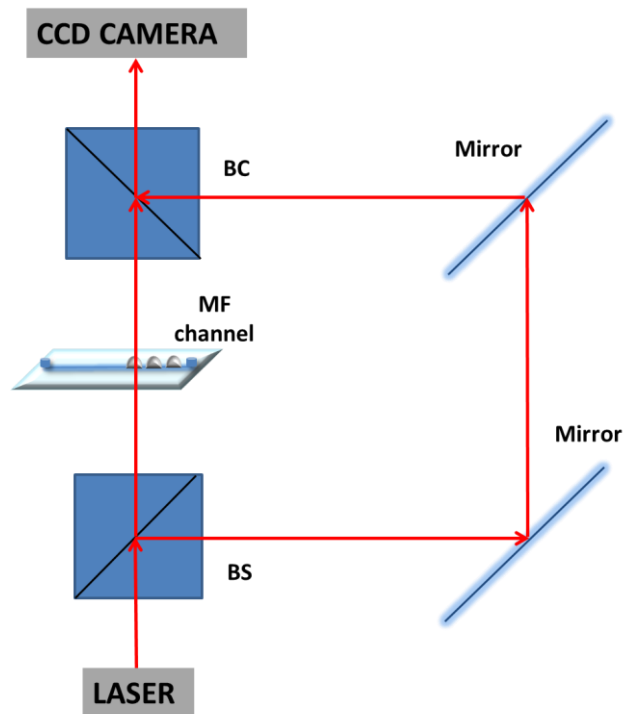

Figure 2.18. Mach-Zehnder interferometer: a continuous wave laser (with wavelength of 632.8 nm) emitted a beam that splits itself into two beams, one directed toward the object and the other recombines itself with the first in order to produce an interference pattern. The beam arrive on a CCD camera 1024x1024, having pixel patch $\Delta x = \Delta y = 4.4 \mu m$). BS: Beam Splitter. MF: Micro-Fluidic. BC: Beam combiner.

The Zernike polynomial expansion is used to model and study the optical aberrations due to the micro-lenses[30,55,68]: though it, a 2D fitting is applied, in order to recover the phase map. The acquisition method of the hologram has been explained in Chapter 1. The radius of curvature of the micro-lens, R, can be

measured from the phase-contrast map relative to the plane in which the lens exit pupil is found. This means that it is possible to estimate the focal length, f, from DH: f=R/(n-1)=4.3 nm, considering n=1.46 as refractive index of the micro-lens. Additionally, DH set-up can capture holograms of a test resolution target, placed behind the micro-fluidic chip, in the sample plan, in order to exalt the capability of the magnifying action of the micro-lens. An example is showed in Figure 2.19, wherein fibroblast cells, flowing into the chip, appear in focus when pass through the lens area, while are out-of-focus in the areas outside the lens.
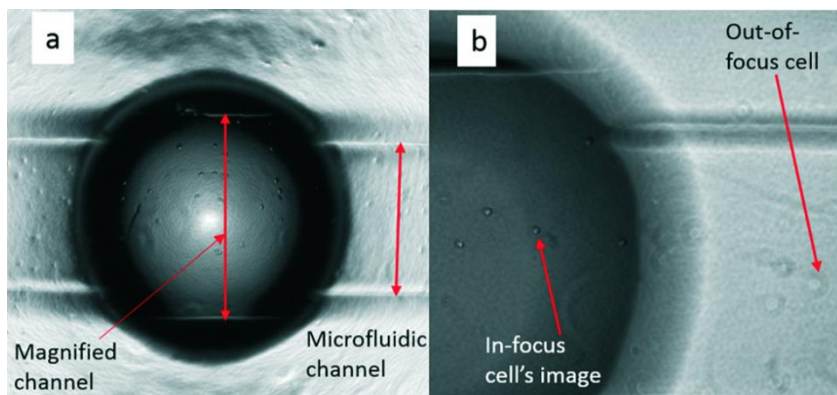

Figure 2.19. Magnification action operated by the micro-lens is showed comparing the distance between the walls of the micro-channel, that appears higher in correspondence of the area occupies by the lens (a). Fibroblast cells focus is not constant in the lens area and outside the lens area (b).

2.3.5 Conclusions

A valid alternative inkjet printing technique able to deposit optical polymeric tools directly onto micro-fluidic chips is proposed. The forward configuration for pyro-EHD printing overcomes the limit of the distance between liquid reservoir and receiving substrate, compared to classic pyro-EHD printing configuration. In this way, the flexibility of the EHD system is increased. Moreover, this printing technique has very high resolution, allowing to print drops of dimensions until few hundred nanometers, having volumes of pico-liters. The use of micro-lenses,

integrated on a micro-fluidic chip, supports the development of fast, portable, and easy-to-use devices with a high level of functional integration. PDMS is a material with good chemical, mechanical and optical properties, absolutely suitable to be pyro-EHD printed and easy to manipulate, in order to cure it and to obtain lenses and devices with good optical performances. DH is an excellent way to evaluate micro-lenses optical properties, also thanks to the transparent property of the PDMS that allows to present the image with good quality.

2.4 Micro-engineered pyroelectric crystal and self-assembling of micro-lenses

Using the described printing approach, it is possible to obtain single lenses on a substrate. It is also possible to obtain an array of lenses, but there are many parameters to check in the drop deposition for the realization of the array. The way to obtain an array more easily is through the use of an engineered substrate with a pattern that heads a flexible layer on it. As extensively explained, the LN crystal shows a pyro-electric effect that can be used to generate a spatial distribution of electrical charges. In fact, those electric charges can induce self-assembling and patterning of a soft material if it is on the crystal, through pyro-EHD[7,69-70]. With correct control of the EHD effect, an array of micro-lenses with great uniformity and with a variable dimension is obtained[7].

2.4.1 Periodically poled lithium niobate (PPLN)

PPLN is obtained by fabricating periodically reversed ferroelectric domains (in Section 1.1 is reported that a pyroelectric material can be also a ferroelectric material and this is the case of the LN) by an electric field poling process that is obtained by an external voltage exceeding the coercive field of the material[71-72]. LN Micro-engineering is a multi-step process: LN crystals are commercially furnished in the form of wafers, so the first step is to reduce LN dimensions to obtain a suitable substrate for the micro-lenses. After that, on the z-side of the LN crystal (each crystal has, conventionally, a Z− and Z+ side, related to the orientation of the domains), a coat of photoresist polymer is laid down and is spin-coated onto the surface with a rate of 3000 rpm for 30 s. The following step is a lithography using a mask able to imprint a pattern on the LN. Zones of the sample are only periodically exposed, namely those that the mask allows to expose. Thus, the pattern on the mask is transferred onto the LN and can have variable sizes; in particular, it can be written as an array of circles having diameters of 25, 50, 100, or 200 μm, depending on the mask used. The shape of

those circles is very important, because the equilibrium in the crystal allows the creation of the characteristic hexagons where the circles are imprinted. Lithography is done using an interferometer consisting of a single laser beam put in interference with itself, exploiting an optical system made by mirrors and lenses. Once the lithography is completed, photoresist is developed by immersing the crystal into an appropriate chemical substance and drying it with nitrogen. The last phase of the preparation of the crystal is the poling, consisting of an oscilloscope, a generator of electric current and a device to maintain the sample between two cells full of water (conductive, transparent, maneuverable and cheap), that permits closing of the circuit and application of tension to the crystal, orienting the domains and imprinting the hexagons. A hexagon is the geometric shape energetically more comfortable to discharge the tension. The tension used to pole a crystal is about 5.2 V. After cleaning the sample by photoresist excess and heating it, it is possible to see the hexagons on the surface. It is important to say that each phase of this process is easily reversible, except for the poling, that requests a complicate apparatus; the risk of over-poling the crystal is not rare (domains do not remain in the zones impressed with lithography, and a large domain on the surface is obtained).

2.4.2 Polymer self-assembling on PPLN

A polymer used for this application is PDMS, an elastomer that keeps a liquid state for a sufficiently long time to slide on the surface of the crystal and create the micro-lens array. It is demonstrated that using an opportune polymer, e.g. PDMS, and spinning it on the PPLN surface, it self-assembles due to pyro-EHD effect[7,73]. In fact, PPLN produces pyroelectric forces due to a charge displacement on its surface (Fig. 2.20), and its structure induces the polymer to follow the pattern impressed on the substrate, producing micro-lenses that have shape and dimensions depending on the PPLN characteristics and spinning setup[7]. Some examples of the effect of the polymer spinning rate are represented in Fig. 2.20,

in the cases of 4000 rounds per minute (rpm) [Fig. 2.20(a)], 6000 rpm [Fig. 2.20(b)], 8000 rpm [Fig. 2.20(c)], and 10,000 rpm [Fig. 2.20(d)].
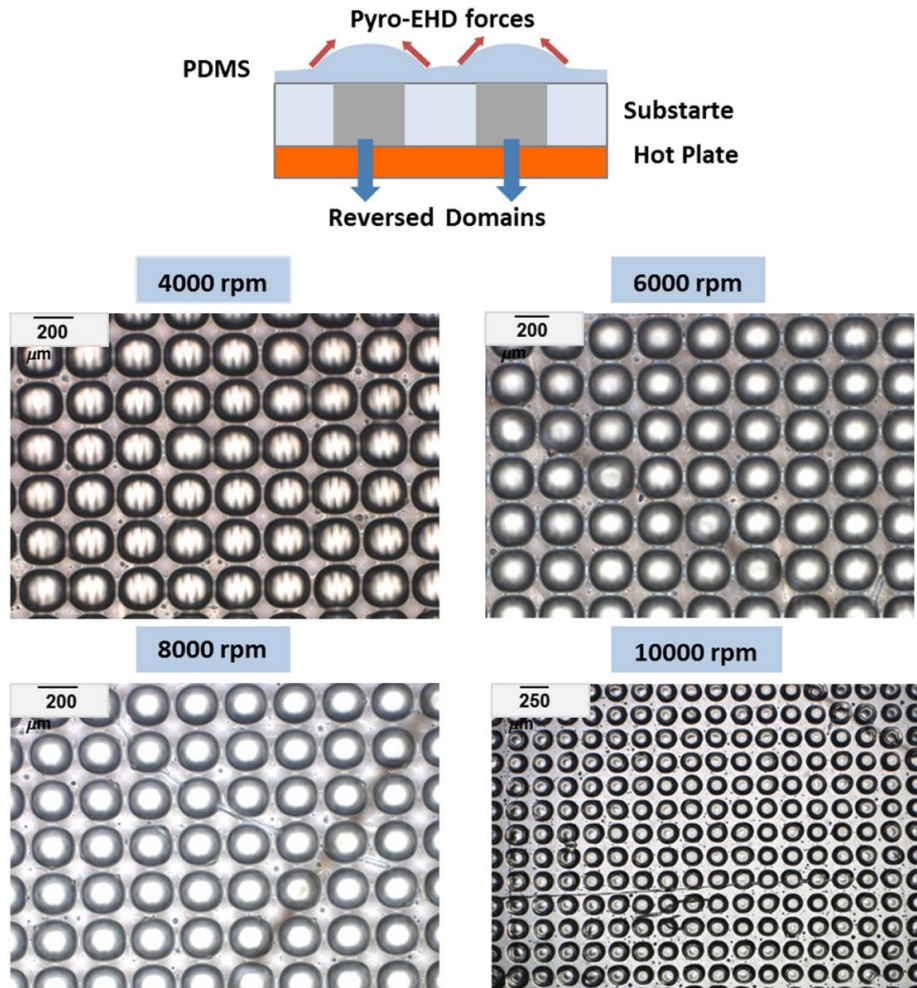

Figure 2.20. Images from PDMS micro-lenses array on a PPLN controlling spinning rate[7].

In order to make the lenses on the crystal, it is sufficient to deposit PDMS, in addition with the curing agent, in a 10:1 concentration proportion, on the surface of the crystal on either of the two sides. At this point, the PDMS is spin-coated onto the PPLN, and that sample is heated at 170°C for 30 s. The pyro-electric effect is activated and the polymer is self-assembled on the surface of the crystal,

following the domains related to the hexagons. An example is shown in Fig. 2.21: a micro-lens array on a 50 μm hexagon pattern is showed.
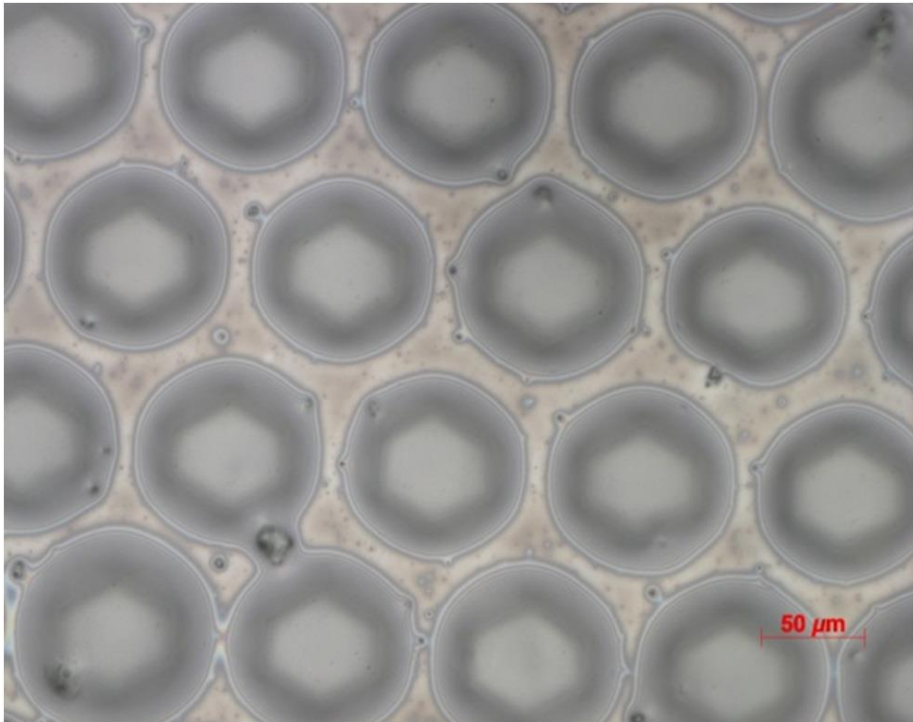

Figure 2.21. PDMS micro-lens array on a 50 μm hexagon PPLN crystal, Z+ side.

As already said, the shape and dimensions of the micro-lenses depend on some factors: PDMS quantity (i.e., spinning rate) and PPLN side are the principal ones. Generally, on the z+ side, PDMS is self-assembled in a classic lens shape, as visible in Fig. 2.22(a), while, on the z− side, lenses do not keep their shape and collapse in their center, creating a donut shape, shown in Fig. 2.22(b).
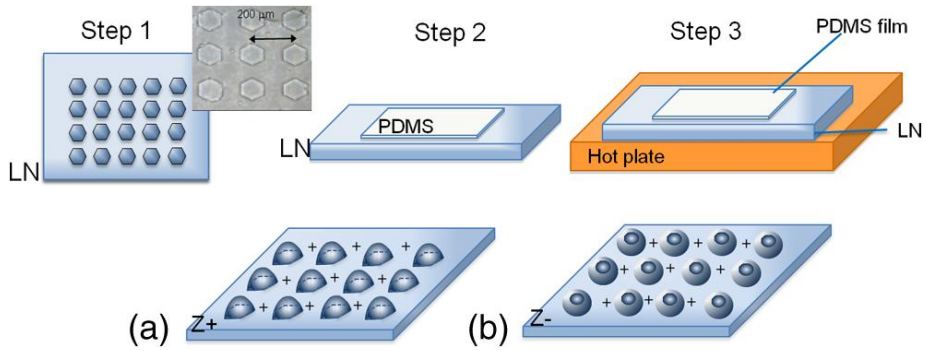
Figure 2.22. Steps to realize a PDMS micro-lenses array (a) and a micro-donut array (b) on a PPLN crystal[7].

A high spinning rate entails a low quantity of PDMS on the PPLN and so shorter lenses, until the polymer does not succeed in shaping lenses, obtaining micro-donuts instead[7].

2.4.3 Microstructure characterization

2.4.3.1   Morphological and optical characterization

Fig. 2.23 summarizes the morphological and optical properties of two microstructures, referring to the characterization of a polymer array.
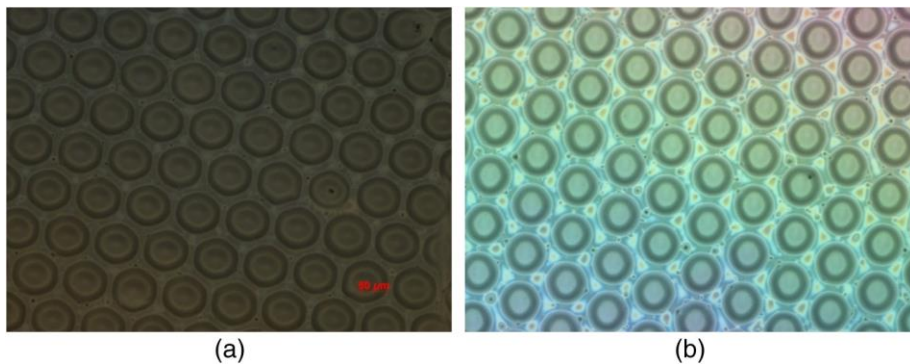

Figure 2.23. Images from micro-donut array (a) and micro-lens array (b), with no concentration of toluene.

Images show the shape of the structures, or eventually the action of the addition of toluene into PDMS[7], as shown in Fig. 2.24. In fact, modulating the viscosity of the solution, the pyroelectric effect acts varying the lens shape: a toluene diluition reduces, in this case, the PDMS viscosity.

(a)
(b)
(c)
(d)
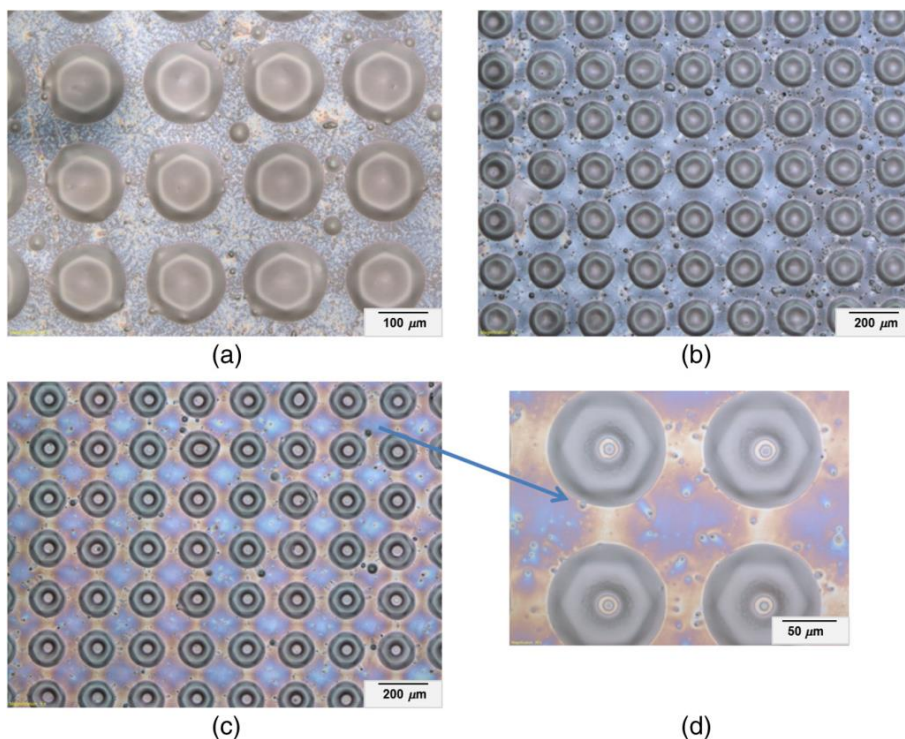
Figure 2.24. Micro-donuts array with toluene added in PDMS in the following volume ratio 1:1 (a), 1:2 (b) and 1:3 (c); magnified view of micro-donuts (d)[7].

For this analysis, a microscope Zeiss Axio Imager M1 has been used. Arrays, being on one of the two sides of the crystal, can be seen in reflection mode, but it becomes necessary when a fluorescence analysis has been done, because filters are linked only with the lamp used for reflection analysis. An important piece of information derived from the microscope analysis is the focal length, evaluated through a z-stack acquisition (known x and y as the axis on the plane of the crystal). A microscope is usually used for this measure in transmission mode. The measure is made using different distances from the samples with an incremental

step of 7 μm. Fig. 2.25 summarizes the morphological and optical properties of three micro-structures. The xz-view of the light cone generated by the lens within a vertical plane passing through one of the xy-symmetry axes is shown in Fig. 2.25(a). The light intensity profile shows a sharp maximum around 700 μm. Fig. 2.25(b) reports the graph of profilometer data for the polymer lens measured along one of the symmetry axes, and a Gaussian fitting of the data is reported to better define the profile. The results are then summarized by the three images in Fig. 2.25(c), where the xy-view is shown: in correspondence to the maximum intensity for lenses, a bright and defined spot is formed. The same characterization is performed for two micro-donuts obtained at different dilution ratios. Figs. 2.25(d) and 2.25(g) show the focal length emitted by the polymer micro-structures and the corresponding profile is reported in Figs. 2.25(e) and 2.25(h). In the case of donuts, the xz-view reveals that each of the two peaks visible in the profile graph generates a cone of light. For the donuts, one global maximum is located around 150 μm above the donut peak. As visible in the results summarized in Figs. 2.25(f) and 2.25(i) in the case of the donuts, the first maximum corresponds to a bright and well-defined light ring, while the second maximum corresponds to a bright spot in the center, but less bright and defined.
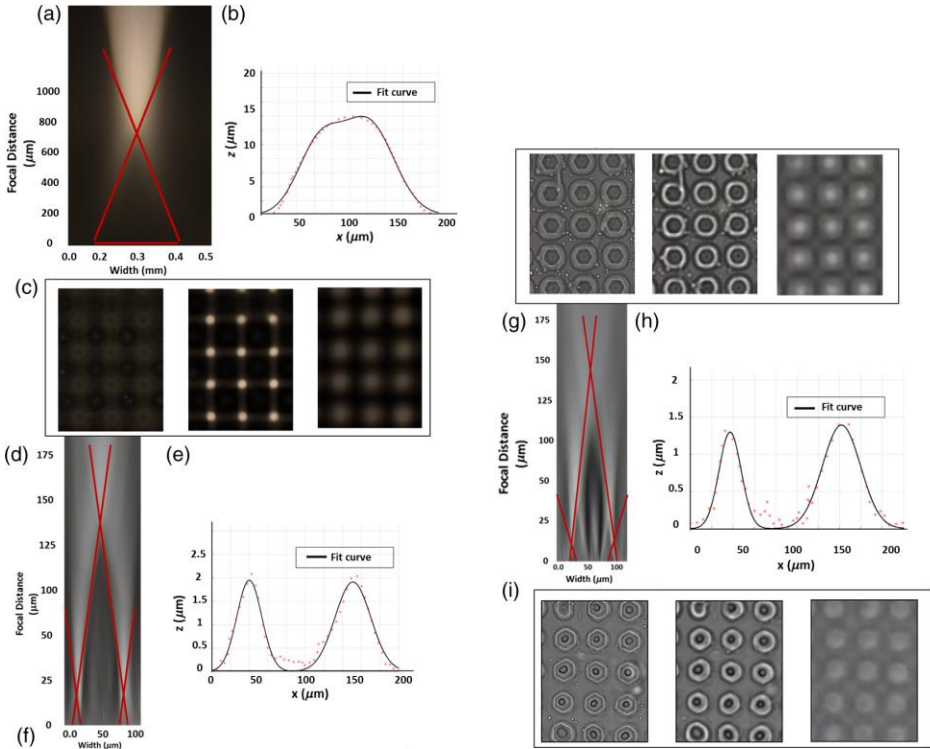
Figure 2.25. Morphological and optical properties of micro-lenses and micro-donuts: xz-view reconstruction for the z-stack acquisition using a Zeiss Axio Imager M1 microscope in transmission mode (a), (d), (g); profilometer measure point and Gaussian fit (bold line) (b), (e), (h); xy-view for focalized light at three different distances (c), (f), (i).

As reported in Table 2.1, the average height of the lens is 14 μm, while the peaks of the donut-like lenses are only 2.1 and 1.5 μm in height for the 1:1 and the 2:1 PDMS dilutions, respectively. The half-band width is also reduced from 105 μm for lenses to about 40 μm for both donuts[7]. Therefore, focal length is generally higher in lenses than in donuts.

	Peak (μm)	Half-band width (μm)	Focal distance (μm)
Lens	14 ± 2	105 ± 10	700 ± 17
Donut (1:1)	2.1 ± 0.3	40 ± 5	144 ± 15
Donut (2:1)	1.5 ± 0.2	39 ± 5	134 ± 20

Table 2.1. Main parameters of polymer microstructures[7].

The z-stack is not the only information obtained from the crystal plane; using a profilometer (Model DektakXT 2011, Bruker Corporation), it is possible to obtain morphological information and surface pattern. Two examples of micro-structure profiles are shown in Figs. 2.26(a) and 2.26(b). For the PDMS, micro-structure is important to set the correct applied force on the sample in order to preserve the structures, as the tip is harder than the structures. A longer analysis permits minimization of error in the measurement; it is more opportune to set a long time as the measure when the structures are micro-donuts, where the profile is more irregular, as shown in Fig. 2.26(b), in order to evaluate the profile at the best in each point. An experimental result is shown in Fig. 2.26(c): as the spin rate is increased, repeating the tests with a constant solution ratio and thermic treatment after spin-coating, the shape of the structures evolves to a donut, while, decreasing the spin rate, the structures acquire a lens shape.
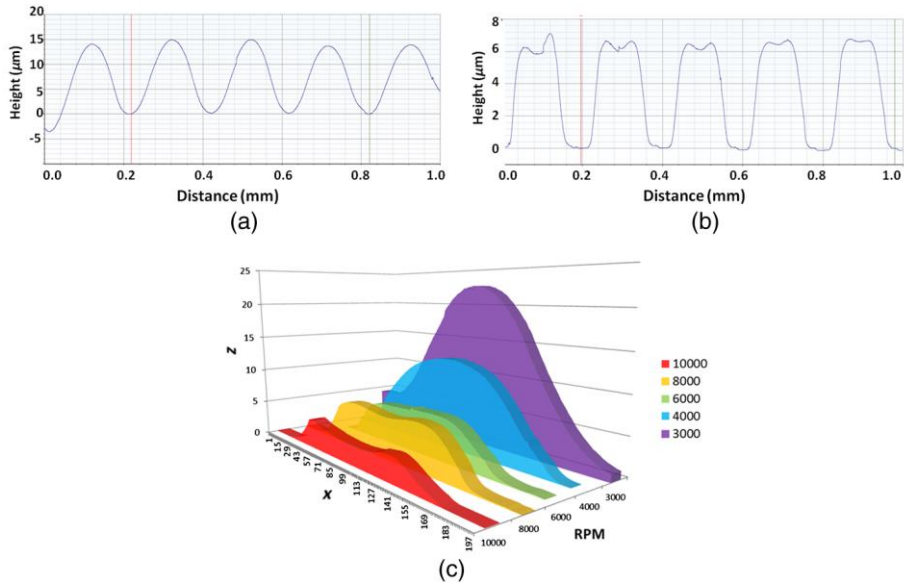
Figure 2.26. Profiles of micro-lenses (a) and micro-donuts (b). Changing spin rate, the shape of the structure is modified, moving from a lens with a higher height with a low spin rate to a donut with lower height when spin rate is increased (c)[7].

2.4.3.2 Interferometric characterization

Interferometric characterization of micro-lenses helps in understanding focus properties and evaluating optic aberrations in them. An experimental set-up consists of a typical Mach‑Zehnder interferometer arranged in a transmission configuration, as shown in Fig. 2.27.

Figure 2.27. Experimental setup used for the micro-lenses' optical characterization[55].

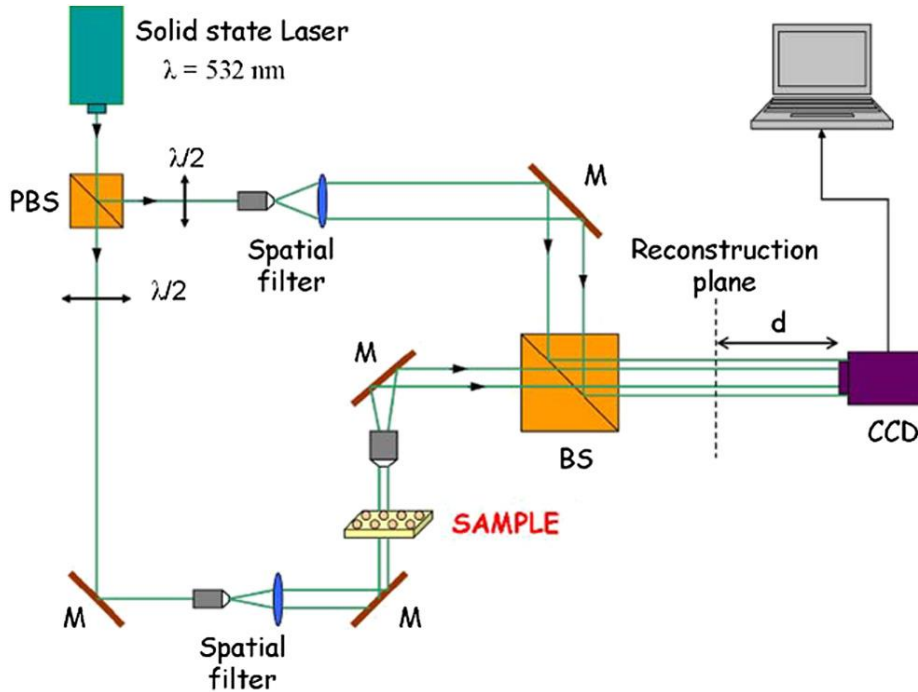The source is a continuous-wave solid state laser emitting light at 532 nm. The beam is divided in two by a beam splitter; the object beam passes through a thin PDMS micro-lens array and is imaged by a 5× microscope objective onto a CCD camera (pixel size 4.4 μm). The reference beam is opportunely expanded and, with the same polarization of the object one, is recombined with it via another beam splitter. The resulting interference pattern, the digital hologram, is recorded by the CCD camera placed at a distance *d* from the image plane according to the holographic technique. The intensity and the phase of the complex wave (wavefields) passing through the PDMS sample are numerically calculated starting from these digitally recorded holograms, which contain the entire information of the specimen. Due to the flexibility of digital holography (DH), the wavefields reconstruction is possible in different image planes without changing the setup, i.e. without moving the sample, simply by varying the reconstruction distance *d* in the reconstruction algorithm. This is based on the

Fresnel transformation method. Figs. 2.28(a) and 2.28(b) display the unwrapped phase map $\varphi(x,y)$ of two different micro-lenses. These phases have been analyzed in order to recover the focal length f of each lens. Figs. 2.28(c) and 2.28(d) show a parabolic fit along both dimensions of the phase according to:

$$\varphi(x, y) = \frac{2\pi}{\lambda} \frac{(x^2 + y^2)}{2f} m \tag{22}$$

with $\lambda = 0.532\ \mu m$. Here, the parabolic approximation of the spherical wavefront of the beam passed through the lens is considered. The focal lengths recovered from the parabolic fits are $f \approx 307\ \mu m$ for the one in Fig. 2.28(a) and $f \approx 1010\ \mu m$ for Fig. 2.28(b). By these measurements, the micro-lens in Fig. 2.28(b) has a higher focal length and the profile is flatter as a consequence of the fabrication process, as results from the fringe number and from the lower value of the phase [Figs. 2.28(b) and 2.28(d)][55].
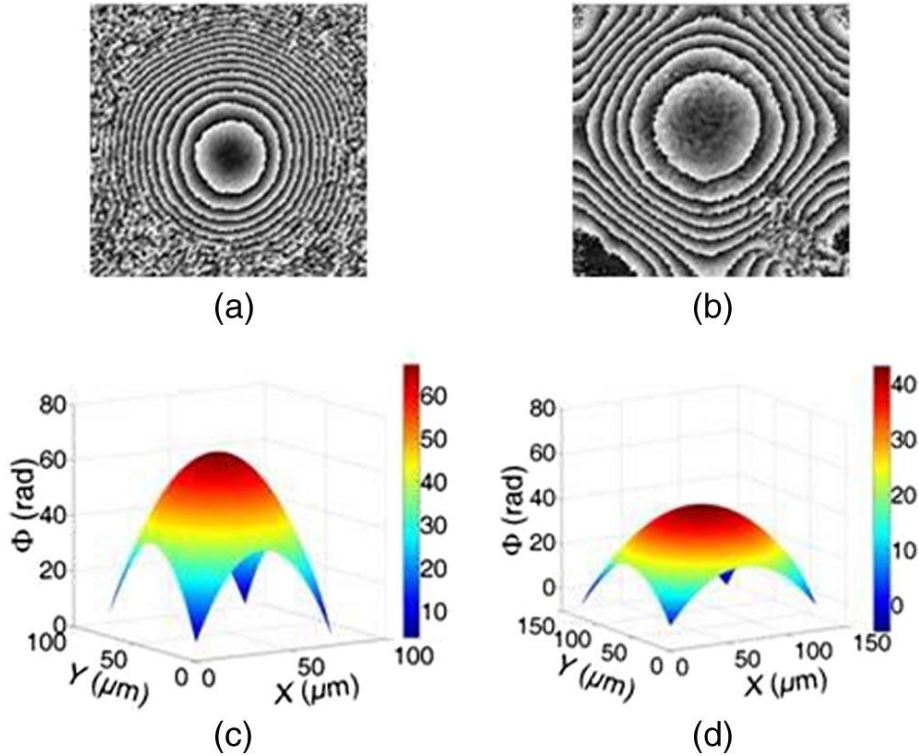
(a)   (b)

(c)   (d)

Figure 2.28. Phase maps of two micro-lenses from different samples (a, b) and corresponding parabolic fits (c, d)[55].

The optical behavior of the micro-lenses is also characterized in terms of the optical aberrations intrinsically present in the lens array, by applying a 2-D fitting procedure. Several holograms of a 4 × 4 lens array are acquired during the stationary condition, i.e., when the number of fringes is stable in the wrapped phase distribution, while the fitting procedure is performed for each of the three chosen lenses of the array and for the lenses of some arrays at different time instants. The function used for the fitting process is a linear combination of Zernike polynomials. The coefficients of the linear combination for tilts, astigmatism, focus, and third-order spherical aberration terms are evaluated. The coma and the higher order coefficients are neglected because they are smaller by some orders of magnitude. The calculated coefficients show that the phase distribution at the exit of each lens is made of the same terms for each lens and,

for each term of the linear expansion, the coefficients of different lenses are similar. This allows us to state that our device displays the same properties for each microlens[30]. A 2-D fitting is applied to the recovered phase map using a Zernike polynomial expansion[74] to model and study the optical aberrations produced by the lens[30,74-75]. To ensure the best fitting results, the hologram plane is chosen in order to obtain a proper sampling of the object information on the whole lens area.Thus, the optical aberrations are estimated in the hologram plane, far *d = 17.3 cm* from the lens exit pupil. As a fitting quality index, we calculated the mean square error (MSE) between the measured and the calculated phase distribution, normalized with respect to the maximum value of the measured phase map. When $P_{MAX}= 10$ terms are adopted to synthesize the Zernike function, an *MSE = 0.07%* is found, assuring a very accurate reconstruction quality. The first 10 orders of the linear combination of Zernike polynomials (i.e., the Zernike function) are shown in Fig. 2.29, along with the corresponding coefficients a_P, representing the weight of each aberration term.
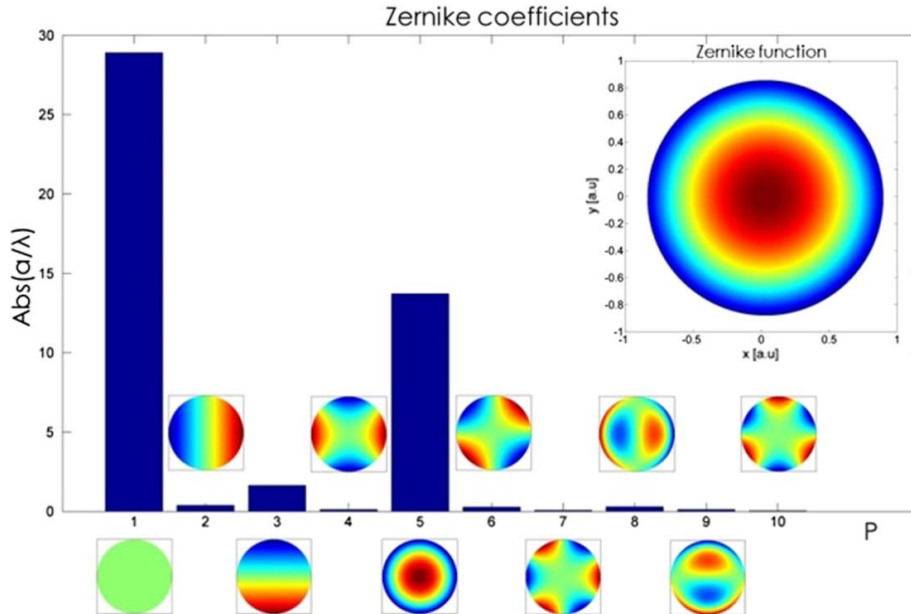
Figure 2.29. Normalized Zernike coefficients derived from the lens phase-contrast map. For each order *P*, the corresponding Zernike polynomial is shown.

From the bar diagram of Fig. 2.29, it is apparent that, except for the constant offset (*P = 1*), the main contribution to the development of the Zernike function is a defocus term (*P = 5*). This is an expected result due to the spherical shape of the lens. Moreover, a tilt along the y axis (*P = 3*) is present, as well as a coma aberration along the x axis (*P = 8*). The other terms give a negligible contribution. If compared to the expected spherical contribution (*P = 5*), the aberration surface distributions depicted in Fig. 2.30 show shorter dynamics.
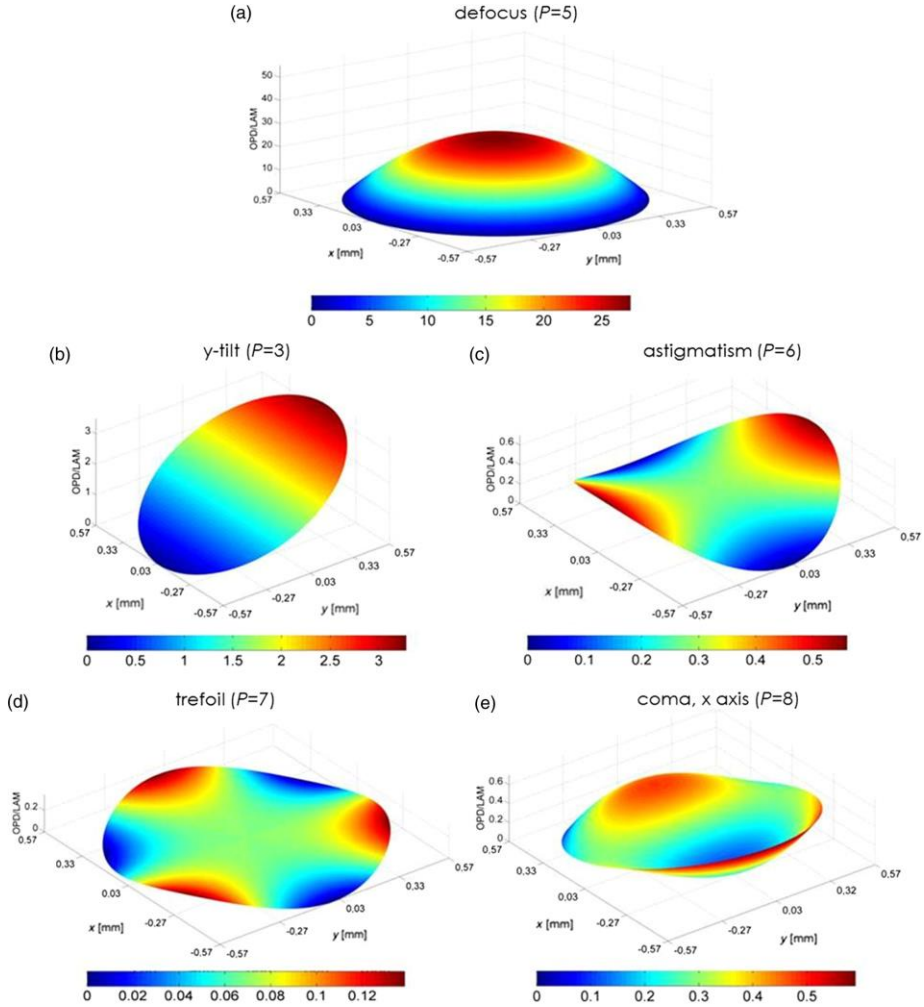
Figure 2.30. Surface distribution of the main Zernike polynomials: spherical factor (a); tilt along the y-axis (b); astigmatism (c); trefoil (d); coma aberration, x-axis (e).

Hence, they play a minor role in determining the optical behavior of the microlens. In order to estimate the lens focal length, we adopted two different strategies, whose results are in good agreement. As previously discussed, DH allows numerically performed z-scanning in order to reconstruct the complex object wavefield in a convenient plane. Thus, it is simple to measure the focal length as the distance between the lens focus plane and its exit pupil. On the other hand, a geometrical approach can be followed. Indeed, the radius of curvature R

can be measured from the phase-contrast map extracted in the plane corresponding to the lens exit pupil. Hence, we estimated the focal length as where $n = 1.46$ is the lens refractive index.

2.4.4 Self-assembled micro-structure functionalization

PDMS can be functionalized by adding a substance into its viscous structure before it is cured. For example, by adding a dispersion of CdSe/CdS (core-type quantum rods, 5 mg/mL in toluene, Aldrich) quantum rods in toluene to PDMS, the fabrication of a lens array has been demonstrated following the same procedure. Once the array is heated, rods arrange themselves in a particular way into the polymer, obtaining a double self-assembly phenomenon due to the pyroelectric effect: pyro-EHD, related to PDMS, and pyro-DEP, related to rods. In this way, a pattern of nano-rods is obtained and is visible through fluorescence microscopy, as shown in Fig. 2.31.

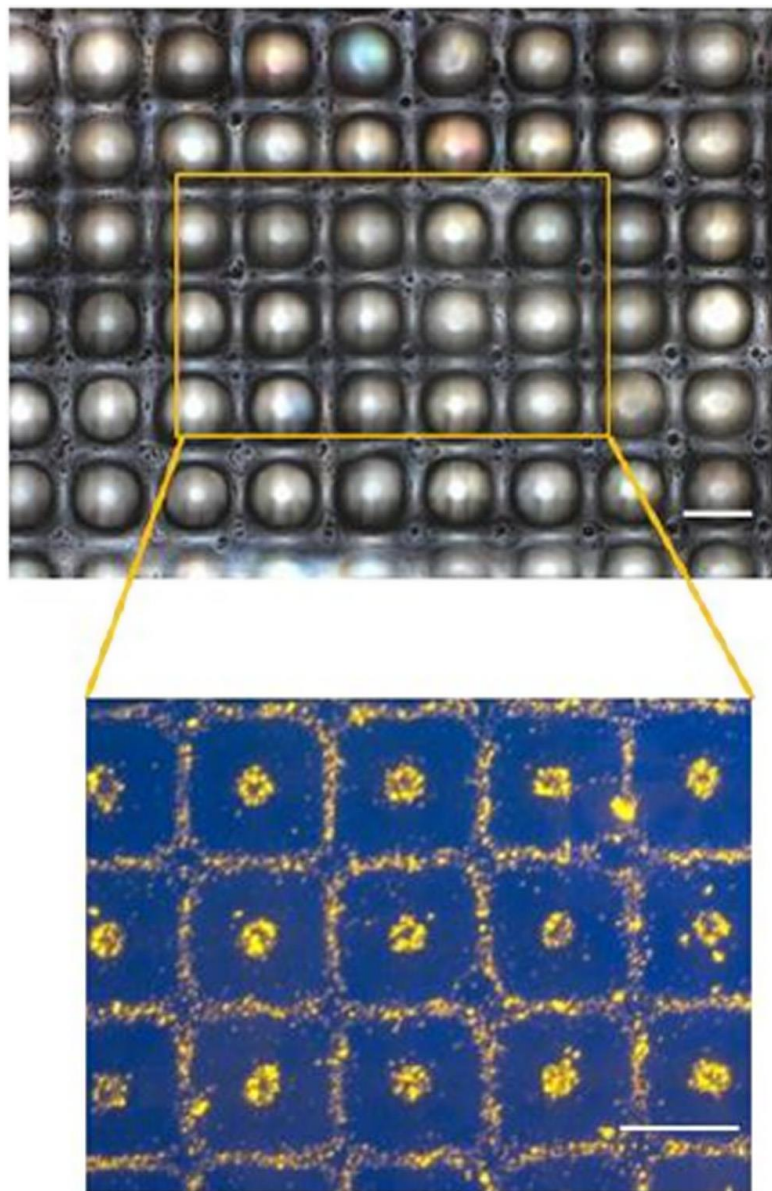**Figure 2.31**. Bright-field image compared to the respective fluorescence image; lenses are self-assembled and nano-rods are arranged in the center and at the border of the lenses (scale bar 100 μm)[76].

The chance of obtaining nano-composites is very interesting, because it is relatively easy for a polymer to incorporate nano-fillers into its matrix, modulating the resulting properties of the nano-composite produced and, at the

71

same time, allowing one to use the existing fabrication methods[76]. Furthermore, the addition of quantum rods allows the organic transformation of passive micro-optical elements into active photonic components[76]. The interaction between the polymer matrix and nano-fillers embedded into it has been further investigated: in the following, a published paper focused on the pyro-DEP effect on quantum dots in PDMS is reported. The hexagon pattern influence and the dots disposition are evaluated, in order to realize a separate dots pattern.

2.5   Paper: "Direct Self-Assembling and Patterning of Semiconductor Quantum Dots on Transferable Elastomer Layer"

Authors and affiliations

Sara Coppola[a], Veronica Vespini[a], Federico Olivieri[a,b], Giuseppe Nasti[a], Michele Todino[a], Biagio Mandracchia[a], Vito Pagliarulo[a] and Pietro Ferraro[a]

[a] Institute of Applied Sciences and Intelligent System- CNR, Via Campi Flegrei 34, Pozzuoli (NA), 80078, Italy.

[b] University of Naples Federico II, Department of Chemical Materials and Production Engineering, Piazzale Tecchio 80, Naples 80125, Italy.

2.5.1 Abstract

Functionalization of thin and stretchable polymer layers by nano- and micro-patterning of nanoparticles is a very promising field of research that can lead to many different applications in biology and nanotechnology. In this work, we present a new procedure to self-assemble semiconductor quantum dots (QDs) nanoparticles by a simple fabrication process on a freestanding flexible PDMS membrane. We used a PPLN crystal to imprint a micrometrical pattern on the PDMS membrane that drives the QDs self-structuring on its surface. This process allows patterning QDs with different wavelength emissions in a single step in order to tune the overall emission spectrum of the composite, tuning the QDs mixing ratio.

2.5.2 Introduction

Colloidal semiconductor QDs have gained popularity since their discovery mainly because of their optical properties and their unique electronic capabilities[77-78]. The sharp wavelength emission spectrum, whose characteristic wavelength can be tuned with slight changes in size and composition, and the quite low cost synthesis make QDs attractive for a range of optoelectronic applications in light emitting diodes[79], nano-electronic devices[80], solar cells[81], quantum computing[82] as well as highly sensitive biomedical diagnostics[83]. Furthermore colloidal quantum dot led (QLEDs) have attracted great attention as for next generation displays or skin-like tattoo for biomedical and wearable electronics. In fact the QDs have unique properties such as the color tunability, photo/air stability, and are printability on various substrates. The device is paper thin and can be applied to human skin like a sticker[84]. However, in order to fully exploit the unique properties of QDs for emergent technology, it is important to find facile fabrication processes for disposing and patterning QDs over large surfaces, favoring their integration with solid-state devices, and at the same time opening new ways for direct QDs decoration of flexible and freestanding plastic layers. In fact, the prospective of using QDs in flexible and wearable opto-

electronics device is still challenging due to lack of suitable fabrication methods. In recent years, much effort has been under-taken for the fabrication of well-ordered soft-matter-based QDs patterns over large area due to their increasing applicability in a lot of different fields such as polymer electronics[85] soft machines[86], light-emitting devices[87], hybrid organic/inorganic solar cells[88] and in particular for chemical and biological sensors. Actually there have been foreseen numerous applications of QDs patterns for highly sensitive biomedical diagnostics[89], tissue-engineering[90], surface modification[91-92] and microfluidics[93]. Despite the numerous advantages of QDs, the fabrication of micro-decorated QDs patterns is still challenging. Different and more or less intricate strategies have been proposed and attempted for creating surface-ordered arrays of QDs. Recent advances include the generation of complex patterns through recognition directed by self-assembly[94–96], direct patterning[79-80] and several lithographic techniques[97–101]. These include deposition of nanoparticles dispersed in di-block-copolymer templates[102] using capillary forces for immobilization[103], self-assembling driven by electrostatic and hydrogen bond interactions[102,104], microcontact printing[105-106] and layer-by-layer (L-b-L) self-assembled technique. Unfortunately, the proposed techniques require multi-steps approaches, often combining the use of expensive photolithography equipment's with chemical surface treatments and/or special functionalization. Unlike conventional lithography, direct dispensing and patterning would be very attractive as it could offer a significant simplification thus avoiding the complications of long processing times, resist deposition, etching, removal and subsequent roughness generation. Electron beam lithography (EBL) can be an attractive lithographic technique for direct patterning but, in general, it becomes difficult to pattern QDs clusters on a pre-defined structure with accurate compensation of alignment mismatch[107-108]. Anyway, EBL is suitable only for processing very restricted areas. From another point of view, spray deposition notably simplifies the degree of morphological and chemical control required in the QDs coating process. Unfortunately, spray coating results in a problematic reduction in performance characteristic of the solution-processed active materials[109]. An alternative low-

cost solution for patterning QDs could be the microcontact printing approach by using a polymer mold. Nevertheless, many common organic solvents used for QDs dispersion (e.g. toluene, hexanes) solubilize polymers and are generally not suitable for pattern replication. In this paper an alternative strategy for QDs direct patterning and the embedded into a stand-alone polymer film is proposed. A LN is functionalized by micro-engineering (i.e. by spatially arranging the inverted ferroelectric domains[38,71]) and covered by a film of hydrophobic polymer. Essentially, the self-patterning method proposed is based on pyro-DEP self-assembling approach and allows the fabrication of a micro-shaped polymer layer functionalized with patterns of colloidal semiconductor QDs. The PPLN samples act as a template for driving the self-assembling by electrode-free DC DEP of polymeric films[38,71,110]. Recently the self-assembling of polymers in patterned array[48,76,111-112] made in PDMS and the fabrication of nano-composite polymeric lens array (diameter ∼100 μm) have been already demonstrated on microscale in case of nano-crystals embedded in the polymeric solution[76]. However at the actual state of the art, capability to get a freestanding patterned elastomer membrane was not demonstrated and achieved yet. Here we show that self-assembly of QDs induced by DEP effect could be used to produce a patterned and transferable elastomer layer. The patterning is obtained by DEP effect activated over a colloidal QDs solution spin coated onto a 25 μm hexagonal PPLN substrate already covered with a thin charged micro-structured PDMS film. The phenomenon at the basis of this experimental behavior is the DEP effect, not induced by an external electric field but due to the pyroelectric effect. The QDs spontaneously assemble under the action of a temperature gradient, creating a decorated polymer layer that is easily transferable in a free-suspended and flexible layer. It is noteworthy that the technique makes use of a reconfigurable electric charge template, thus allowing us to avoid tedious replications of specific chemical and/or physical procedures or the use of molds. In fact, a single driving crystal is reusable indefinitely for fabricating multiple patterned flexible layers. The proposed process not only offers a simple route for pattering and controlling

the distribution of QDs but also reduces the complexity of fabrication of a functionalized self-assembled material.

2.5.3 Fabrication process

PPLN is the result of a micro-engineering process applied to a LN crystal. Periodically reversed ferroelectric domains are obtained applying an external electrical voltage, exceeding the coercive field of the material[71-72]. Shape and size of the QDs array can be varied by changing the underneath PPLN pattern in the bulk LN substrate. Details on poling process can be found in literature[38,112]. A typical PPLN with hexagonal geometry is shown in Fig. 2.32(a). In this work we exploit an interesting effect observed recently regarding the capability to manipulate liquid and drops by pyroelectric-EHD effect. As we reported in a previous work, in which nematic liquid crystals droplets could be fragmented and spatially self-assembled on the PPLN substrate driven by electric filed induced by pyro-electric effect[113], here we use the pyro-DEP forces for the self-assembling of QDs. The conditions in which the instabilities produce fragmentation and dewetting of QDs are governed by the interaction between solid-liquid interface and liquid-air interface, as in case of liquid crystals[113]. The QDs pattern produced formed could be reconfigured very easily because the particles are free to move on top of the polymer layer. In the case of CdSe/CdS/PDMS nano-composite they were embedded into the polymer and their positions were fixed after the PDMS crosslinking[76]. The QDs are fragmented and driven by the DEP effect induced by the pyroelectric field activated by thermal stimulus applied to the PPLN substrate during spin coating and self-assembled on the substrate according to the underneath ferroelectric domain patterned structure into LN. In fact, the QDs patterning is guided exclusively by DEP effect due to the pattern of charges created and exposed by the PPLN crystal as a consequence of the pyroelectric effect[38,71,76,110,113]. It is worth to be noted that the morphology of the underlying polymer, although not negligible, is not the driving force of the self-assembling. The QDs pattern (i.e.

on the top of the hills) is not consistent with the more energetically favorable and stable configuration (i.e. on the bottom of the valleys). This pattern is rather consistent to the DEP forces as already demonstrated in a previous work[66]. Nevertheless it is very difficult to detach the patterned membrane from the PPLN crystal thus preventing the possibility to achieve free-standing and transferrable membranes with the patterned QDs. A commercial thermo-crosslinkable PDMS solution (Dow Corning Sylgard 184, 10:1 mixing ratio, base to curing agent Midland; $\eta = 3900$ cP, $\varepsilon_p = 2.65$ from datasheet) was prepared and deposited on the PPLN crystal by spin coating [Fig. 2.32(b)]. Depending on the spin rate, different film thickness can be obtained, ranging from ~ 10 µm at 3000 rpm for 1 min to ~ 150 nm at 10000 rpm for 8 min. The phenomenon at the basis of the self-assembling of the polymeric layer is the EHD[35,48,112]. In our case, however, this process is not induced by an external electric field, but it is due to a pyro-electric effect: the variation in temperature induces a charge displacement on PPLN surface used to create a polymeric pattern[48,112]. After the spinning procedure, the crystal is heated at 170 °C for 30 s onto a conventional hot plate [Fig. 2.32(c)] and two different typologies of structures can be obtained, depending on the choice of the crystal side (Z− or Z+). Uncompensated charges are free to diffuse into the polymer while is in its liquid phase and PPLN structure induces the polymer self-assembling as direct function of the pattern impressed on the surface of the substrate, producing a micro-structured film[48,112]. In particular, the polymeric fluid crowds where the pyro-electric field reaches the maximum of the intensity: on Z+ the maximum is around the hexagons [Fig. 2.32(d), sample A], while on Z− the maximum is in the center of the hexagons[48,112] [Fig. 2.32(e), sample B]. The diameter of the micrometrical polymeric pattern depends on the dimensions of the hexagonal structures of the PPLN crystal; in this work we scaled the average dimension of the hexagons down to 25 µm.
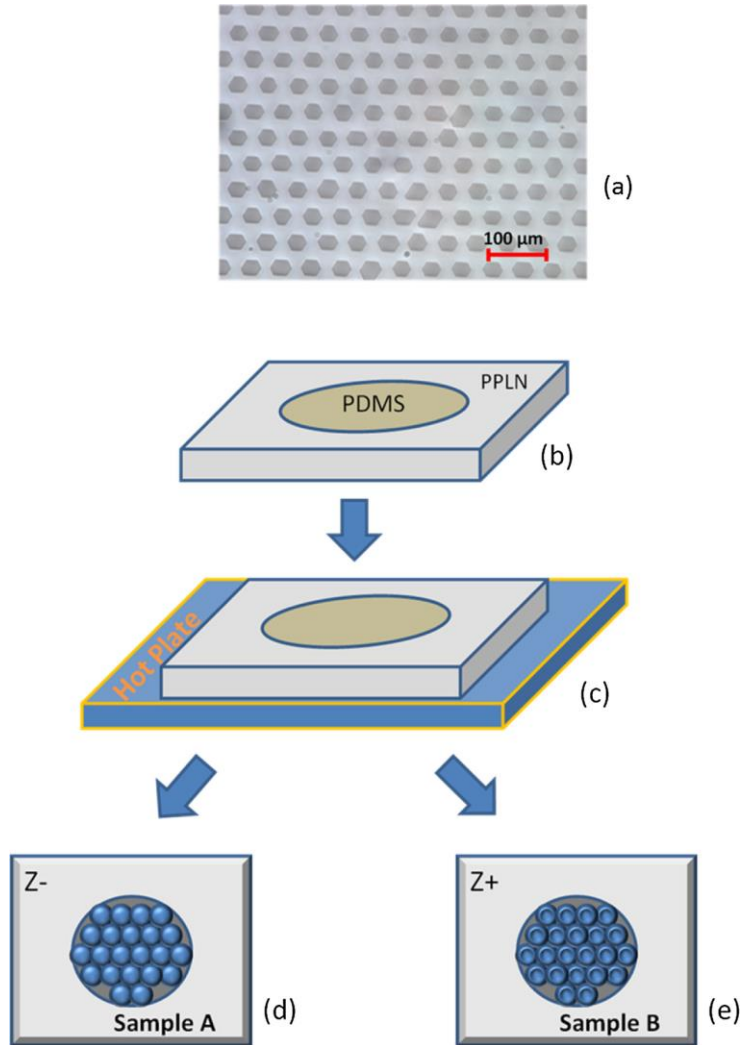
Figure 2.32. A typical PPLN is showed in (a). PDMS is deposited on PPLN (b) and heated on an hot plate (c). Depending on crystal side two different PDMS structures can be obtained, i.e. small bumps (d) or slight craters (e), schematically illustrated in (d) sample A and (e) sample B, respectively.

In Fig. 2.33 optical images of micro-structured polymer film are presented: samples A is produced on Z− side while sample B onto Z+ side.
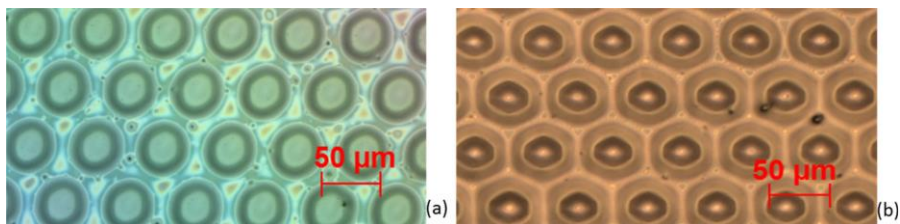
Figure 2.33. Typical images of sample A and sample B, obtained by using a Zeiss Axio Imager M1 microscope in reflection mode; (a) polymer film decorated with polymer micro-bumps and (b) polymer film decorated with polymer micro-craters arrays on a 25 μm hexagonal PPLN crystal.

In a first step, a double layered film onto the PPLN substrate was obtained. The procedure is illustrated in Fig. 2.34. A thin film of CdSe QDs was deposited on top of the PDMS structures by self-assembly techniques. The realization of the double layer makes possible to pattern directly the polymer surface and, furthermore, the problems relative to the dispersion of dots into the polymer matrix are overcome. In this approach, the first layer is made by cured PDMS that self-assembles into very thin and flat micro-structured film, while the second layer is made by Quantum Dots in Toluene Solution (QDTS). In particular, 25 μL of a Lumidot CdSe quantum dots (core-type, fluorescence λ_{em} 560 nm, Sigma Aldrich) solution were spin coated on the polymeric film produced onto the PPLN sample. The spinning rate for the polymer self-assembling has been chosen in order to maintain the micro-structures due to the regions of highest electric filed in a flat polymeric layer. The optimal spin condition for QDs patterning was a speed rate of 5000 rpm for 2 min, these spin coating speed and duration allow the evaporation of toluene during spinning and, simultaneously, the self-assembly of QDs on PDMS. A 25 μL drop of the 0.08 vol% QDs dispersion in toluene was spin coated over a 2 × 2 cm PPLN sample, the maximum time employed to prepare the sample during which the polymer and the solvent are in contact has to be of about 20 s, making a balance between polymer dissolution and solvent evaporation. The drop volume and spinning time were selected in order to reduce the swelling of the crosslinked PDMS membrane[114].
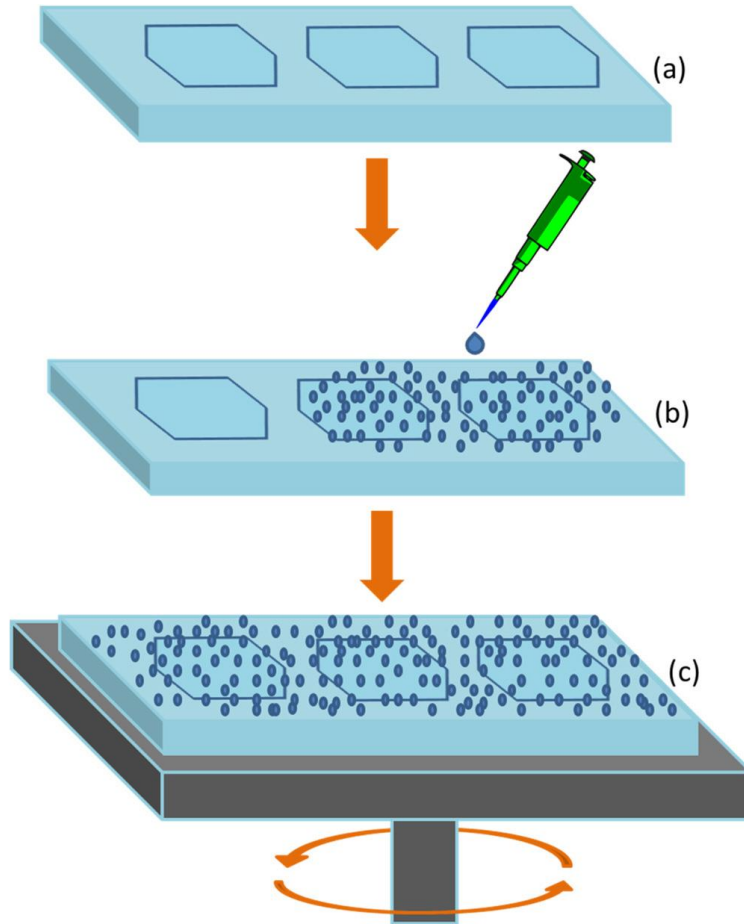
Figure 2.34. Schematic illustration of the deposition and spinning processes to realize the double layer film onto the PPLN substrate, (a) PDMS micro-bumps or micro-craters on PPLN z−/z+ face, (b) standard QDs deposition procedure, (c) a typical spin coating process.

In Fig. 2.35 is outlined the arrangement of QDTS that are initially homogeneously dispersed [Figs. 2.35(a) and 2.35(b)]. On sample A, during spin, dots move from their initial position [Fig. 2.35(c)] and occupy precise position over the hexagons [Fig. 2.35(e)]. Otherwise, on sample B, QDs move from their starting position [Fig. 2.35(d)] to a new one, preferentially around the hexagons [Fig. 2.35(f)]. The movement of QDs over the polymer film is related to the DEP effect activated by the underlying micro-structured PPLN, widely described in literature[115–117]. The

distribution obtained on each side of the crystal is opposed to the more energetically favorable configuration that would occur in the case of the micro-structured polymer layer without the underlying PPLN crystal. In sample A the pyro-DEP effect is maximum at the center of the hexagon, while in a sample B the pyro-electric field collapses at the center of the hexagon while the maximum is reached at the border of the domain[38,71,76,110]. In the case of a QDTS spin-coated onto the Z− face of a PPLN substrate (sample A), a high density of small QDs droplets covers the domain region. This phenomenon resembles the well-known dewetting effect observed in correspondence of the underlying polymeric micro-structured film[113,118-119]. If the QDTS solution is deposited onto the Z+ face of the PPLN crystal (sample B) an opposite behavior is obtained, demonstrating that the phenomena are driven by the sign of the pyro-electric charge intermediate by the polymer film. In fact, in case of sample B, the experimental evidence is that almost all of the QDs drops move selectively in the area around the hexagons. In this case, the interconnections of near droplets reduce the interfacial tension between QDs and PDMS promoting a coalescence effect in time[118].
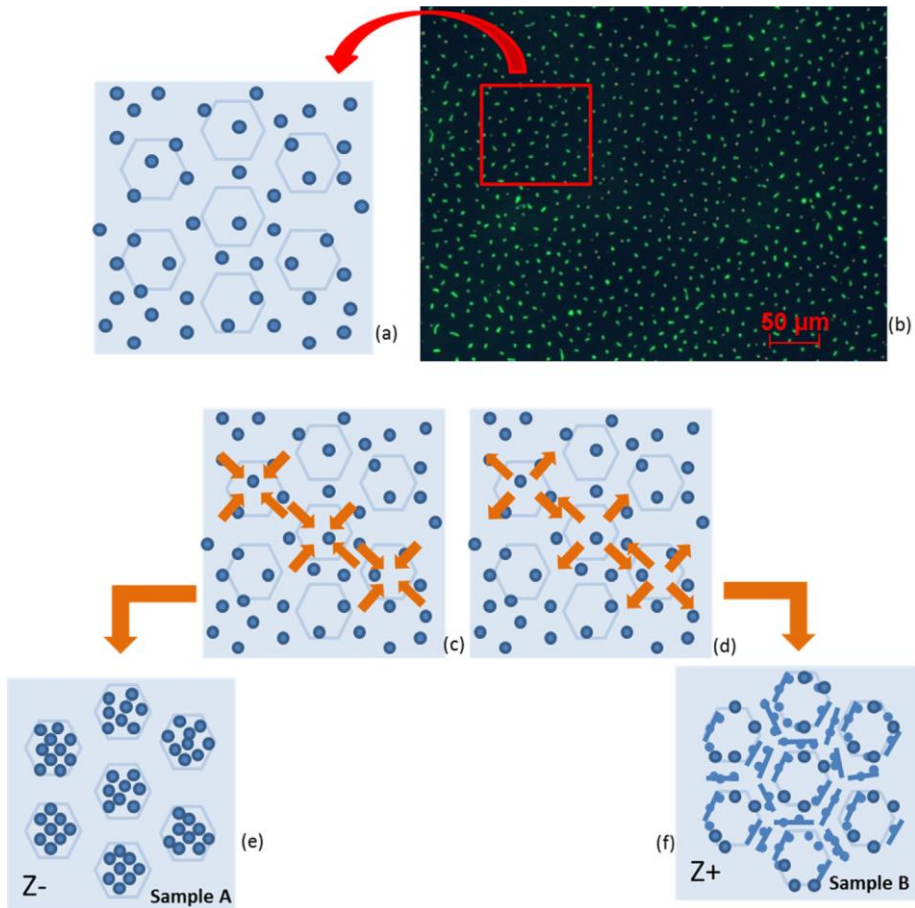
Figure 2.35. QDTS on PDMS micro-structures. QDs move from their initial random position (a), view under fluorescence microscope (b), after spin, arrange themselves: on sample A (c) they move to the center of the polymer micro-bumps (e), while on sample B (d) they pattern around the craters (f).

In Fig. 2.36 are showed two images captured by Zeiss microscope, using a fluorescence lamp and a FITC filter. Fig. 2.36(a) represents the pattern impressed by dots on sample A; QDs occupy only the areas onto the underling hexagons. In Fig. 2.36(b), on a sample B, dots pattern the borders of the hexagonal domains and occupy halfway areas between the domains. In the inset of Fig. 2.36(a) is reported the mean fluorescence intensity distribution measured over N = 22 dots of the Z− sample while in the inset of Fig. 2.36(b) the same measure of

fluorescence intensity is reported for over N = 20 dots of the Z+ face. In this way, it is demonstrated the possibility of obtaining QDs pattern on very small domains: these sparse dots arrangement is accurately patterned inside and outside the hexagonal periodic structures, as shown in Figs. 2.36(a) and 2.36(b), respectively. The reduced dimensions of the domains "force" QDs to occupy narrow areas of the sample, according to the underlying charge pattern impressed on PPLN; this is possible because PDMS is already cured and shaped into a flat micro-structured film when the second layer is deposited on it. QDTS is easy to deposit on this pattern and QDs self-assemble spontaneously on it. Exploiting this approach, another interesting opportunity is used for the fabrication of a multi-QDs layer on PDMS. The starting polymeric micro-structured film on PPLN has been made in the same way of the previous samples, while, about the second layer, QDTS was substituted by a solution containing QDs having three different emission wavelengths of 480 nm, 520 nm and 610 nm in a variable mixing ratio, respectively. The Three Quantum Dots Layer (TQDL) solution is preliminarily sonicated for 15 min and then 25 μL of this mix are spin coated over the polymer film. Spin conditions are unchanged, according to those relative to the sample B.
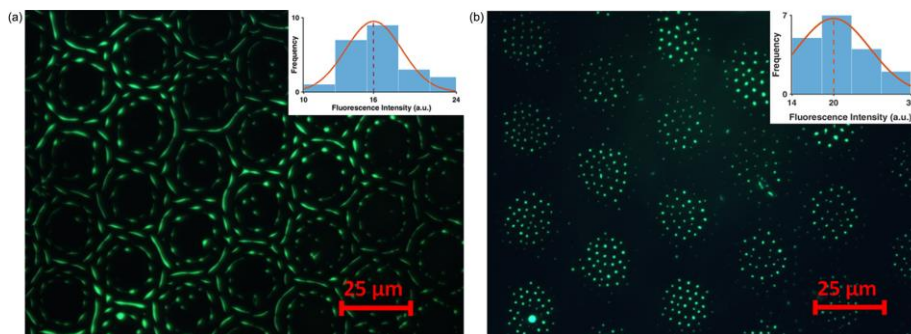

Figure 2.36. Images obtained using a FITC filter from a sample A, having hexagons domains with a diameter of 25 μm, on Z− side (a), and a sample B, with the same domains, on Z+ side (b). On Z−, dots mark little points over the hexagons, while, on Z+, they stand along the space between the domains.

In Fig. 2.37 is represented an image captured with a fluorescence lamp, using a DAPI filter. Dots follow the underlying structure, like in one kind QDs case. As showed in Fig. 2.37(a), QDs emission is whitish as expected from the superposition of the three primary colors. The QDs size is small compared to the clusters size therefore the individual wavelength emission cannot be distinguished by optical microscopy. However, to demonstrate the presence of the three QDs, a measure by OceanOptics QE65000 Spectrometer has been realized and the results are showed in Fig. 6b. The overall spectrum acquired using a DAPI filter show the combination of the three emissions of QDs. The spectrum appears equally distributed overall the visible wavelength coherently to the white color of QDs in Fig. 2.37(a) (black line). In order to distinguish the different component of the emission related to the different particles we performed two spectroscopic measurements using a FITC and RHODAMINE filters. The FITC excitation filter allows to isolate the emission of the green QDs emitting at 520 nm, as visible in Fig. 2.37(b) (green line). Using the RHODAMINE filter (red line) also the red QDs peak could be isolated.

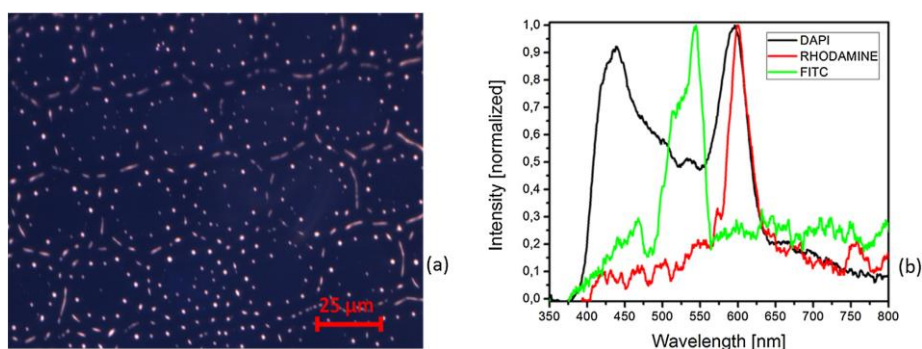**Figure 2.37**. PDMS on a sample A + TQDL, made using a 10:2:1 mixing ratio, image, captured with a DAPI filter, of a Z+ 25 μm sample (a). (b) shows the spectrum of TQDL layer obtained.

Once obtained the double layer smooth polymeric sandwich on the PPLN, we introduced a third outer layer of PDMS on the sandwich, leaving it for a day to cure at ambient temperature T_{amb}. After 24 h the top PDMS film resulted solid

enough to be removed from the decorated PPLN crystal (bottom), used as a mold. This third step allows to transfer on the third removable PDMS layer both the polymer microstructure and the QDs assembly. It is worth to be noted that the last two steps, deposition of QDs and molding of the third layer, can be replicated indefinitely. The process is schematized in Fig. 2.38. After the formation of the PDMS micro-structured film [Fig. 2.38(a)], QDs are deposited on the sample leading to their self-assembly [Fig. 2.38(b)]. The PDMS + QDs sample is used as a mold to transfer the QDs nano-structure to a third, removable, PDMS layer [Fig. 2.38(c)].
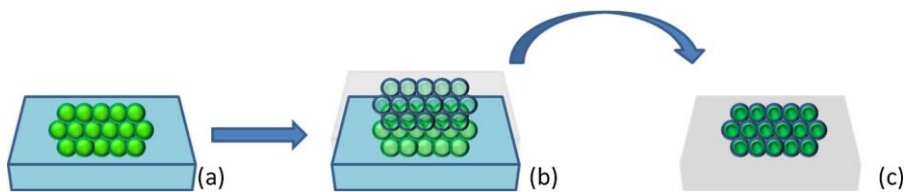

Figure 2.38. Steps to obtain a PDMS + QDs mold: from the starting double layer on PPLN (a), using a second PDMS layer (b), is has been obtained a mold having the negative of initial pattern impressed on it (c).

In Figs. 2.39(a) and 2.39(b) are showed the images of the polymeric layer (hexagon side 50 μm) captured in bright field and using fluorescence lamp (DAPI filter), while in Figs. 2.39(c) and 2.39(d) are showed the images of the mold film, in bright field and fluorescence mode respectively. We demonstrated that QDs micro-structure could be easily transferred from the crystal to the film, following the same profile pictured on the crystal, making a flexible and free standing replica. The dimension of the pattern upon the membrane is around 4 cm^2 and is directly related to the dimension of the underlying PPLN crystal used for the fabrication and it could be potentially extended up to the entire LN wafer surface. As QDs are deposited on the surface of the solid PDMS, when the top layer of liquid PDMS is poured, the most part are embedded in the uncured resin and then fixed on its surface after crosslinking. As shown in Fig. 2.39 the QDs pattern obtained on the mold [Figs. 2.39(c) and 2.39(d)] is accurately replicated on the

free standing film [Figs. 2.39(a) and 2.39(b)]. The efficiency of the particles transfer is not complete as the mold remains slightly fluorescent after the process but, the percentage of the QDs transferred to the self-standing membrane is about 30% and it was quantified by fluorescence examination.
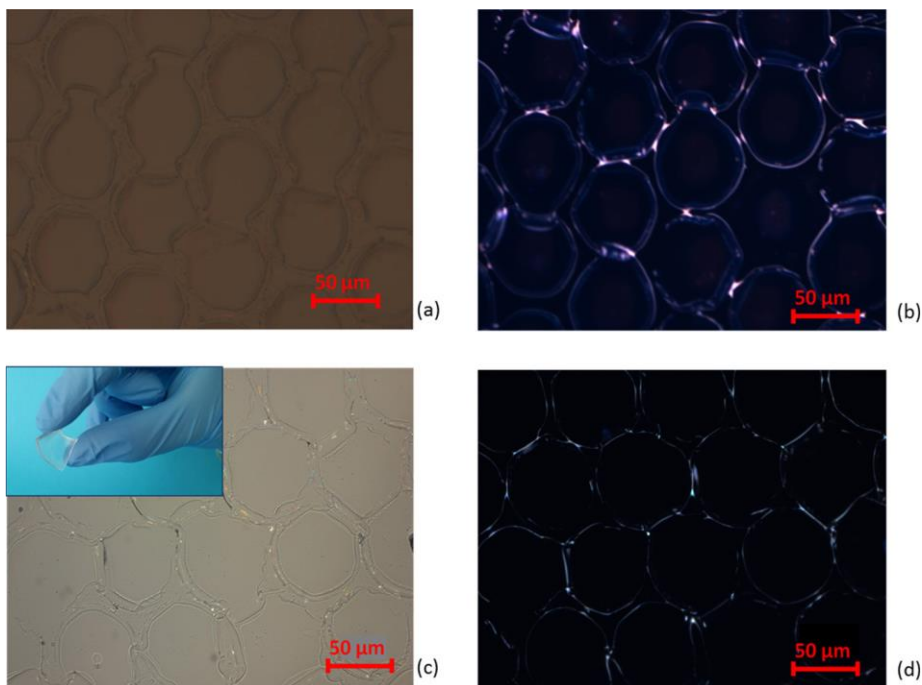
Figure 2.39. A 50 μm PPLN (a), with QDs having emission wavelength of 480 nm, 520 nm and 610 nm, in 18:2:1 mixing ratio, on Z+ side sample. The same image, showed in (b), is captured using a DAPI filter. In (c) is represented PDMS film obtained by this sample in bright field, in the insert is shown the free-standing flexible PDMS membrane, while the image obtained using DAPI filter, is showed in (d).

2.5.4 Conclusions

In this work, we presented a facile method to self-assemble nanoparticles of semiconductor QDs on a free-standing flexible PDMS films. Such self-assembling of nano-composite polymer could inspire future fabrication techniques for producing layers that could be mounted on top of OLED devices

in order to drive the light in a more efficient way or for improving their photovoltaic efficiency. Moreover, scaling down the dimension of the polymeric structures and controlling the self-assembling of QDs over large area represents a very promising tool in biology and nanotechnology.

References

1. Y. Lu et al., "A self-assembly approach to the fabrication of patterned, two-dimensional arrays of microlenses of organic polymers", Adv. Mater. 13, 34–37 (2001).

2. X. Jin et al., "Microlenses with tuned focal characteristics for optical wireless imaging", Appl. Phys. Lett. 105, 031102 (2014).

3. I. Frese et al., "Polymer based optical interconnect module for a bidirectional transceiver and optical NxM star couplers for Datacom applications with data rates > 1 Gbps", in Proc. of the 7th Electronics Packaging Technology Conf., 471–476 (2005).

4. H. Navarro et al., "Three-dimensional imaging and display through integral photography", J. Inf. Commun. Convergence Eng. 12, 89–96 (2014).

5. J. S. Donner et al., "Fast and transparent adaptive lens based on plasmonic heating", ACS Photonics 2, 355–360 (2015).

6. X. Xiao et al., "Enhancing light harvesting of organic solar cells by using hybrid microlenses", Opt. Appl. 45, 89–100 (2015).

7. V. Vespini et al., "Electrohydrodynamic assembly of multiscale PDMS microlens arrays", IEEE J. Sel. Top. Quantum Electron. 21(4), 399–406 (2015).

8. I. A. Grimaldi et al., "Printing of polymer microlenses by a pyro-electrohydrodynamicdispensing approach", Opt. Lett. 37(13), 2460–2462 (2012).

9. B. D. Gates et al., "Unconventional nanofabrication", Annu. Rev. Mater. Res. 34, 339–372 (2004).

10. Y. Xia and G. M. Whitesides, "Soft lithography", Angew. Chem. Int. Ed. 37, 550–575 (1998).

11. T. H. Lin, C. K. Chao, and S. Y. Hung, "A novel fabrication method of micro-needle mold by using the micro-lens mask through contact printing", Microsyst. Technol. 21, 1843–1848 (2015).

12. T. K. Shih et al., "Fabrication of PDMS (polydimethylsiloxane) microlens and diffuser using replica molding", Microelectron. Eng. 83, 2499–2503 (2006).

13. T. K. Shin, J. R. Ho, and J.W. J. Cheng, "A new approach to polymeric microlens array fabrication using soft replica molding", IEEE Photonics Technol. Lett. 16(9), 2078–2080 (2004).

14. S. Y. Chou, P. R. Krauss, and P. J. Renstrom, "Embossing on the nanometerscale", Appl. Phys. Lett. 67, 3114–3116 (1995).

15. N. S. Ong, Y. H. Koh, and Y. Q. Fu, "Microlens array produced using hot embossing process", Microelectron.Eng. 60, 365–379 (2002).

16. A. Voet, "Ink and Paper in the Printing Process", Interscience Publishers, Inc., New York (1952).

17. L. T. Jiang et al., "Fabrication of plastic microlens arrays using hybrid extrusion rolling embossing with a metallic cylinder mold fabricated using dry film resist", Opt. Express 15(19), 12088–12094 (2007).

18. P. H. Huang et al., "Fabrication of large area resin microlens arrays using gas-assisted ultraviolet embossing", Opt. Express 16(5), 3041–3048 (2008).

19. T. T. Wen and H. Hocheng, "Innovative rapid replication of microlensarrays using electromagnetic force-assisted UV imprinting", J. Micromech. Microeng. 19(2), 025012 (2009).

20. C. Y. Chang and S. Y. Yang, "Fabrication of polymer microlens arrays using capillary forming with a soft mold of micro-holes array and UV-curable polymer", Opt. Express 14(13), 6253–6258 (2006).

21. C. Y. Chang et al., "A novel method for rapid fabrication of microlens arrays using micro-transfer molding with soft mold", J. Micromech. Microeng. 16, 999–1005 (2006).

22. Y. J. Lee et al., "Microlens array fabricated using electrohydrodynamic instability and surface properties", Opt. Express 19(11), 10673–10678 (2011).

23. H. Hu et al., "Fabrication of bifocal microlens arrays based on controlled electrohydrodynamic reflowing of pre-patterned polymer", J. Micromech. Microeng. 24(9), 5027–5035 (2014).

24. X. Xi et al., "The self-assembly and patterning of thin polymer films on pyroelectric substrates driven by electrohydrodynamic instability", Soft Matter. 8, 298–302 (2012).

25. Y. Kim, S. Jang, and J. H. Oh, "High-resolution electrohydrodynamic printing of silver nanoparticle ink via commercial hypothermic needles", Appl. Phys. Lett. 106, 014103 (2015).

26. P. Ferraro et al., "Dispensing nano-pico droplets and liquid patterning by pyroelectrohydrodynamic shooting", Nat. Nanotechnol. 5, 429–435 (2010).

27. F. Mugele and J. C. Baret, "Electrowetting: from basics to applications", J. Phys.: Condens. Matter. 17, R705–R774 (2005).

28. S. Kuiper and B. H. W. Hendriks, "Variable-focus liquid lens for miniature cameras", Appl. Phys. Lett. 85(7), 1128–1130 (2004).

29. S. Grilli et al., "Liquid micro-lens array activated by selective electrowetting on lithium niobate substrates", Opt. Express 16(11), 8084–8093 (2008).

30. L. Miccio et al., "Tunable liquid microlens arrays in electrode-less configuration and their accurate characterization by interference microscopy", Opt. Express 17(4), 2487–2499 (2009).

31. B. Berge and J. Peseux, "Variable focal lens controlled by an external voltage: an application of electrowetting", Eur. Phys. J. 3, 159–163 (2000).

32. W. H. Hsieh and J. H. Chen, "Lens-profile control by electrowetting fabrication technique", IEEE Photonics Technol. Lett. 17(3), 606–608 (2005).

33. H. Ren and S. T. Wu, "Tunable-focus liquid microlens array using dielectrophoretic effect", Opt. Express 16(4), 2646–2652 (2008).

34. T. B. Jones et al., "Dielectrophoretic liquid actuation and nanodroplet formation", J. Appl. Phys. 89(2), 1441–1448 (2001).

35. F. Merola et al., "Self-patterning of a polydimethylsiloxane microlens array on functionalized substrates and characterization by digital holography", J. Micromech. Microeng. 19(12), 125006 (2009).

36. S. Grilli et al., "Quantitative phase microscopy for accurate characterization of microlens arrays", Coherent Light Microsc. 46, 115–144 (2011).

37. P. Ferraro et al., "Wettability patterning of lithium niobate substrate by modulating pyroelectric effect to form microarray of sessile droplets", Appl. Phys. Lett. 92, 213107 (2008).

38. S. Grilli and P. Ferraro, "Dielectrophoretic trapping of suspended particles by selective pyroelectric effect in lithium niobate crystals", Appl. Phys. Lett. 92, 232902 (2008).

39. J. Li, F. Rossignol, and J. Macdonald, "Inkjet printing for biosensor fabrication: combining chemistry and technology for advanced manufacturing", Lab. Chip 15, 2538–2558 (2015).

40. S. Lee and J. Choi, "MEMS print heads for industrial printing", Smart Sensor MEMS 14, 402–430 (2014).

41. I. Endo et al., "Bubble jet recording method and apparatus in which a heating element generates bubbles in a liquid flow path to project droplets", Brevetto, US 4740796 A (1988).

42. B. Hadimioglu et al., "Acoustic ink printing", IEEE Ultrasonics Symposium, 929–935 (1992).

43. C. H. Chen, D. A. Saville, and I. A. Aksay, "Scaling laws for pulsed electrohydrodynamic drop formation", Appl. Phys. Lett. 89, 124103 (2006).

44. K. Barton et al., "A desktop electrohydrodynamic jet printing system", Mechatronics 20(5), 611–616 (2010).

45. M. S. Onses et al., "Mechanism, capabilities and applications of high resolution electrohydrodynamic jet printing", Mater. Rev. 34, 4237–4266 (2015).

46. J. U. Park et al., "High-resolution electrohydrodynamic jet printing", Nat. Publish. Group 6, 782–789 (2007).

47. J. Park et al., "Prediction of drop-on-demand (DOD) pattern size in pulse voltage-applied electrohydrodynamic (EHD) jet printing of Ag colloid ink", Appl. Phys. 117(4), 2225–2234 (2014).

48. H. A. Pohl, "Dielectrophoresis: The Behavior of Neutral Matter in Nonuniform Electric Fields", Cambridge University Press, Cambridge (1978).

49. J. G. Lee et al., "Electrohydrodynamic (EHD) dispensing of nanoliter DNA droplets for microarrays", Biosens. Bioelectron. 21(12), 2240–2247 (2006).

50. R. T. Collins, J. Jones, M. T. Harris and O. A. Basaran, "Electrohydrodynamic tip streaming and emission of charged drops from liquid cones", Nat. Phys., 4(2), 149–154 (2008).

51. S. Coppola et al., "Pyro-printing on demand of polymer microlenses", 2014 Fotonica AEIT Italian Conf. Photonics Technologies IEEE, 1–3, (2014).

52. S. Coppola et al., "Nanocomposite polymer carbon black coating for triggering pyro-EHD inkjet printing", Appl. Phys. Lett. 106, 261603 (2015).

53. M. de Angelis et al., "Plasmon resonance of gold nanorods for all optical drawing of liquid droplet", Appl. Phys. Lett. 103, 163112 (2013).

54. I. A. Grimaldi et al., "Graded-size microlens array by the pyro-electrohydrodynamic continuous printing method", Appl. Opt. 52(32), 7699–7705 (2013).

55. F. Merola et al., "Exploring the capabilities of digital holography as tool for testing optical microstructures", 3D Res. 2(1), 1–8 (2010).

56. A. K. Diallo et al., "Laser-induced forward transfer of multi-layered structures for OTFT applications", Appl. Surf. Sci., 336, 11–15 (2015).

57. C. Florian et al., "Conductive silver ink printing through the laser-induced forward transfer technique", Appl. Surf. Sci., 336, 304–308 (2015).

58. V. Vespini et al., "Forward electrohydrodynamic inkjet printing of optical microlenses on microfluidic devices", Lab Chip 16(2), 326-333 (2016).

59. Ackenhusen, J., "Microlenses in optical communications" IEEE J. Quantum Electron., 15(9), 1026 (1979).

60. Coppola, S., Vespini, V., Nasti, G., Gennari, O., Grilli, S., Ventre, M., Iannone, M., Netti, P. A., Ferraro, P., "Tethered Pyro-Electrohydrodynamic Spinning for Patterning Well-Ordered Structures at Micro- and Nanoscale", Chem. Mater. 26(11), 3357-3360 (2014).

61. Xi, X., Zhao, D., Tong, F., Cao, T., "The self-assembly and patterning of thin polymer films on pyroelectric substrates driven by electrohydrodynamic instability", Soft Matter, 8, 298-302 (2012).

62. Bao, B., Jiang, J., Li, F., Zhang, P., Chen, S., Yang, Q., Wang, S., Su, B., Jiang L., Song, Y., "Fabrication of patterned concave microstructrures by inkjet imprinting", Adv. Funct. Mater. 25(22), 3286-3294 (2015).

63. Coppola, S., Vespini, V., Grilli, S., Ferraro, P., "Self-assembling of multi-jets by pyro-electrohydrodynamic effect for high throughput liquid nanodrops transfer", : Lab Chip 11(19), 3294-3298 (2011).

64. Viswanathan, P., Ondeck, M. G., Chirasatitsin, S., Ngamkham, K., Reilly, G. C., Engler A. J., Battaglia, G., "3D surface topology guides stem cell adhesion and differentiation", Biomater. 52, 140-147 (2015).

65. Duan, Y., Huang, Y., Yin, Z., Bu N., Dong, W., "Non-Wrinkled, Highly Stretchable Piezoelectric Devices by Electrohydrodynamic Direct-Writing", Nanoscale 6(6), 3289-3295 (2014).

66. Grilli, S., Coppola, S., Nasti, G., Vespini, V., Gentile, G., Ambrogi, V., Carfagna, C., Ferraro, P., "Hybrid ferroelectric-polymer microfluidic

device for dielectrophoretic self-assembling of nanoparticles", RSC Advances 4(6), 2851-2857 (2014).

67. Vespini, V., Coppola, S., Grilli, S., Paturzo, M., Ferraro, P., "Pyroelectric Adaptive Nanodispenser (PYRANA) microrobot for liquid delivery on a target", Lab Chip. 11(18), 3148-3152 (2011).

68. Bianco, V., Paturzo, M., Marchesano, V., Gallotta, I., Di Schiavi E., Ferraro, P., "Optofluidic holographic microscopy with custom field of view (FoV) using a linear array detector", Lab Chip, 15(9), 2117-2124 (2015).

69. J. D. Brownridge et al., "Observation of multiple nearly monoenergetic electron production by heated pyroelectric crystals in ambient gas", Appl. Phys. Lett. 78(8), 1158–1159 (2001).

70. B. Rosenblum, P. Bräunlich, and J. P. Carrico, "Thermally stimulated field emission from pyroelectric $LiNbO_3$", Appl. Phys. Lett. 25(17), 17–19 (1974).

71. S. Grilli et al., "In situ investigation of periodic poling in congruent $LiNbO_3$ by quantitative interference microscopy", Meas. Sci. Technol. 19, 074008 (2008).

72. M. Yamada et al., "First-order quasi-phase matched $LiNbO_3$ waveguide periodically poled by applying an external field for efficient blue second-harmonic generation", Appl. Phys. Lett. 62, 435–436 (1993).

73. J. Choi et al., "Drop-on-demand printing of conductive ink by electrostatic field induced ink jet head," Appl. Phys. Lett. 93, 193508 (2008).

74. D. R. Iskander et al., "Modeling of corneal surfaces with radial polynomials", IEEE Trans. Biomed. Eng. 49(4), 320–328 (2002).

75. P. Marquet, C. Depeursinge, and P. J. Magistretti, "Review of quantitative phase-digital holographic microscopy: promising novel imaging technique to resolve neuronal network activity and identify cellular biomarkers of psychiatric disorders", Neurophoton. 1(2), 020901 (2014).

76. S. Coppola et al., "Two-fold self-assembling of nanocrystals into nanocomposite polymer", IEEE J. Sel. Top.Quantum Electron. 22(1), 4800107 (2015).

77. V. Nandwana, R. Mout, Y.C. Yeh, S. Dickert, M.T. Tuominen, V.M. Rotello, Patterning of Protein/Quantum Dot Hybrid Bionanostructures, J. Inorg. Organomet. Polym. Mater. 23 (1) (2013) 227–232.

78. W.C.W. Chan, S.M. Nie, Quantum dot bioconjugates for ultrasensitive nonisotopic detection, Science 281 (1998) 2016–2018.

79. D. Bodas, C. Khan-Malek, Direct patterning of quantum dots on structured PDMS surface, Sens. Actuators B 118 (1) (2007) 168–172.

80. M.J. Hampton, J.L. Templeton, J.M. De Simone, Direct patterning of CdSe quantum dots into sub-100 nm structures, Langmuir 26 (5) (2010)3012–3015.

81. Y.J. Na, S.J. Park, S.W. Lee, J.S. Kim, Photolithographic process for the patterning of quantum dots, Ultramicroscopy 108 (10) (2008) 1297–1301.

82. J.J. Gassensmith, P.M. Erne, W.F. Paxton, M. Frasconi, M.D. Donakowski, F. Stoddart, Patterned assembly of quantum dots onto surfaces modified with click microcontact printing, Adv. Mater. 25 (2) (2013) 223–226.

83. Y.H. Ghymn, K. Jung, M. Shin, H. Ko, A luminescent down-shifting and moth-eyed anti-reflective film for highly efficient photovoltaic devices, Nanoscale 7 (2015) 18642–18650.

84. M.K. Choi, J. Yang, K. Kang, D.C. Kim, C. Choi, C. Park, S.J. Kim, S.I. Chae, T.H. Kim, J.H. Kim, T. Hyeon, D.H. Kim, Wearable red–green–blue quantum dot light-emitting diode array using high-resolution intaglio transfer printing, Nat. Commun. 6 (2015) 7149.

85. M. Ikawa, T. Yamada, H. Matsui, H. Minemawari, Y. Tsutsumi, Y. Horii, M. Chikamatsu, R. Azumi, R. Kumai, T. Hasegawa, Simple push coating of polymer thin-film transistors, Nat. Commun. 3 (2012) 1176.

86. S.A. Morin, R.F. Shepherd, S.W. Kwok, A.A. Stokes, A. Nemiroski, G.M. Whitesides, Camouflage and display for soft machines, Science 337 (2012) 828–832.

87. S. Coe, W.K. Woo, M. Bawendi, V. Bulovic, Electroluminescence from single monolayer of nanocrystals in molecular organic devices, Nature 420 (2002)800–803.

88. A. Malavè, M. Tewes, T. Gronewold, M. Lohndorf, Development of impedance biosensors with nanometer gaps for marker-free analytical measurements, Microelectron. Eng. 587 (2005) 78–79.

89. L.R. Giam, S. He, N.E. Horwitz, D.J. Eichelsdoerfer, J. Chai, Z. Zheng, D. Kim, W.Shim, C.A. Mirkin, Positionally defined: binary semiconductor nanoparticles synthesized by scanning probe block copolymer lithography, Nano Lett. 12 (2)(2012) 1022–1025.

90. J.C. Nawroth, H. Lee, A.W. Feinberg, C.M. Ripplinger, M.L. McCain, A. Grosberg, J.O. Dabiri, K. Kit Parker, A tissue-engineered jellyfish with biomimetic propulsion, Nat. Biotechnol. 30 (2012) 792–797.

91. F. Wang, M.Q. Xue, T. Cao, Thermochemical patterning of polymer thin filmswith tunable size-reduction effects using metal-coated poly dimethylsiloxane stamps, Adv. Mater. 21 (2009) 2211–2215.

92. M. Cavallini, D. Gentili, P. Greco, F. Valle, F. Biscarini, Micro-and nanopatterning by lithographically controlled wetting, Nat. Prot. 7 (2012)1668–1676.

93. M. Jamal, A.M. Zarafshar, D.H. Gracias, Differentially photo-crosslinked polymers enable self-assembling microfluidics, Nat. Commun. 2 (2011) 527.

94. H. Xu, R. Hong, T. Lu, O. Uzun, V.M. Rotello, Recognition-directed orthogonal self-assembly of polymers and nanoparticles on patterned surfaces, J. Am. Chem. Soc. 128 (10) (2006) 3162–3163.

95. C. Subramani, S. Dickert, Y.C. Yeh, M.T. Tuominen, V.M. Rotello, Supramolecular functionalization of electron-beam generated nanostructures, Langmuir 27 (4) (2011) 1543–1545.

96. X. Duan, M.H. Park, Y. Zhao, E. Berenschot, Z. Wang, D.N. Reinhoudt, V.M. Rotello, J. Huskens, Metal nanoparticle wires formed by an integrated nanomolding-chemical assembly process: fabrication and properties, ACS Nano 4 (12) (2010) 7660–7666.

97. S.N. Jun, E.J. Jang, J.J. Park, J.M. Kim, Photopatterned semiconductor nanocrystals and their electroluminescence from hybrid light-emitting devices, Langmuir 22 (6) (2006) 2407–2410.

98. Y. Ofir, I.W. Moran, C. Subramani, K.R. Carter, V.M. Rotello, Nanoimprint lithography for functional three-dimensional patterns, Adv. Mater. 22 (32)(2010) 3608–3614.

99. C. Subramani, Y. Ofir, D. Patra, B.J. Jordan, I.W. Moran, M.H. Park, K.R. Carter, V.M. Rotello, Nanoimprinted polyethyleneimine: a multimodal template for nanoparticle assembly and immobilization, Adv. Funct. Mater. 19 (18) (2009)2937–2942.

100. C. Subramani, A. Bajaj, O.R. Miranda, V.M. Rotello, Biocompatible charged and uncharged surfaces using nanoparticle films, Adv. Mater. 22 (47) (2010)5420–5423.

101. M.J. Hampton, J.L. Templeton, J.M. De Simone, Direct patterning of CdSe quantum dots into sub-100 nm structures, Langmuir 26 (15) (2010)3012–3015.

102. C.L. Zhang, T. Xu, D. Butterfield, M.J. Misner, D.Y. Ryu, T. Emrick, T.P. Russell, Controlled placement of CdSe nanoparticles in diblock copolymer templates by electrophoretic deposition, Nano Lett. 5 (2) (2005) 357–361.

103. Y. Cui, M. Bjork, A. Liddle, C. Sonnichsen, B. Boussert, P. Alivisatos, Integration of colloidal nanocrystals into lithographically patterned devices, Nano Lett. 4(5) (2004) 1093–1098.

104. D.J. Zhou, A. Bruckbauer, C. Abell, D. Klenerman, D.J. Kang, Fabrication of three-dimensional surface structures with highly fluorescent quantum dots by surface-templated layer-by-layer assembly, Adv. Mater. 17 (10) (2005)1243–1248.

105.   X.C. Wu, A.M. Bittner, K. Kern, Microcontact printing of CdS/dendrimer nanocomposite patterns on silicon wafers, Adv. Mater. 16 (5) (2004) 413–417.

106.   Z. Hens, D.V. Talapin, H. Weller, D. Vanmaekelbergh, Breaking and restoring a molecularly bridged metal quantum dot junction, Appl. Phys. Lett. 82 (2002)4245–4247.

107.   A.A. Tseng, Nanofabrication: Fundamentals and Application, World Scientific Publishing Co. Pte. Ltd., Arizona U.S.A, 2008.

108.   V. Pagliarulo, Electron Beam Lithography Patterning of Superconducting and Magnetic Nanostructures for Novel Optical and Spintronic Devices Ph.D. Thesis, University of Naples Federico II, Napoli, Italy, 2010.

109.   I.J. Kramer, J.C. Minor, G. Moreno-Bautista, L. Rollny, P. Kanjanaboos, D.Kopilovic, S.M. Thon, G.H. Carey, K.W. Chou, D. Zhitomirsky, A. Amassian, E.H. Sargent, Efficient spray-coated colloidal quantum dot solar cells, Adv. Mater.27 (1) (2014) 116–121.

110.   S. Grilli, V. Vespini, P. Ferraro, Surface-charge lithography for direct PDMS micro-patterning, Langmuir 24 (23) (2008) 13262–13265.

111.   F. Merola, S. Grilli, S. Coppola, V. Vespini, S. De Nicola, P. Maddalena, C.Carfagna, P. Ferraro, Reversible fragmentation and self-assembling of nematic liquid crystal droplets on functionalized pyroelectric substrates, Adv. Funct. Mater. 22 (15) (2012) 3267–3272.

112.   F. Olivieri, M. Todino, S. Coppola, V. Vespini, V. Pagliarulo, S. Grilli, P. Ferraro, Fabrication of polymer lenses and microlens array for lab-on-a-chip devices, Opt. Eng. 55 (8) (2016) 1–16, 081319.

113.   J.N. Lee, C. Park, G.M. Whitesides, Solvent compatibility of poly(dimethylsiloxane)-based microfluidic devices, Anal. Chem. 75 (23) (2003) 6544–6554.

114.   T. Kimura, M. Yamato, A. Nara, Particle trapping and undulation of a liquid surface using a microscopically modulated magnetic field, Langmuir 20 (3) (2004) 572–574.

115.   R. Cicoria, Y. Sun, Dielectrophoretically trapping semiconductive carbon nanotube networks, Nanotechology 19 (2008), 485303-485207.

116.   P. Mokry, M. Marvan, J. Fousek, Patterning of dielectric nanoparticles using dielectrophoretic forces generated by ferroelectric polydomain films, J. Appl. Phys. 1078 (9) (2010) 094104.

117.   L. Valentini, F. Mengoni, A. Taticchi, A. Marrocchi, J.M. Kenny, Surface patterning of linearly functionalized 43 paracyclophanes by voltage assisted dewetting, J. Mater. Chem. 16 (2006) 1622–1625.

118.   F. Vandenbrouck, M.P. Valignat, A.M. Cazabat, Thin nematic films: metastability and spinodal dewetting, Phys. Rev. Lett. 82 (13) (1999) 2693–2696.

CHAPTER 3

TETHERED PYRO-EHD SPINNING (TPES) FOR POLYMER FIBERS PRINTING: MICRO-CHANNELS FABRICATION

3.1 Fibers patterning through TPES

Electrospinning (ES) is a consolidated technique largely used to deposit polymeric fibers. Its working is guided by an electric field, strong enough to deform a liquid droplet; when the electrostatic repulsion, generated by applying the field, overcomes the surface tension of the liquid, the drop turns into the Taylor's cone and starts to dispense material onto a target substrate. The great advantage of this technique consists of the possibility to exploit the high viscous polymeric solutions or polymers with very long chains to keep a continuous jet of material and to obtain polymeric fibers.
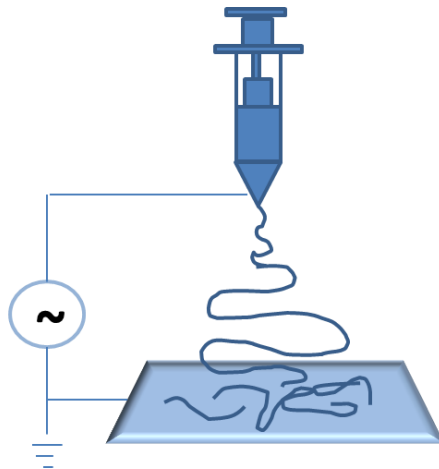

Figure 3.1. Electrospinning setup; typically, the fiber polymeric deposition produces mats.

One of the limitations of this technique consists of the troubles in the ordered deposition of fibers: the random jet of the polymer by the nozzle produces a low-ordered fiber pattern (Fig. 3.1). In order to improve the manageability of the jet, several solutions have tested[1-2], such as near-field ES[3-4], field-induced ES[5-8] and mechano ES[9]. However, problems as the complexity of the setup, the selection of suitable polymers in order to exploit the spinneret and to not clog the nozzle and the high required temperature are not overcome by these solutions. The tethered pyro-electrodynamic spinning (TPES) is a revolutionary system that works

without wires, electric circuits, electrodes and nozzle[10]. Fiber jet is driven by the pyro-electric field, activated by a LN crystal, in a configuration very similar to the one used for the pyro-EHD printing of micro-lenses, already showed in Chapter 2[11].
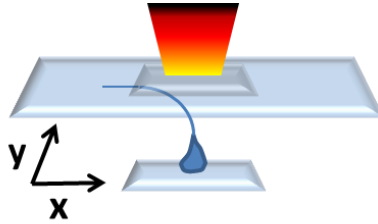

Figure 3.2. TPES setup: the LN crystal is heated and actives a pyro-electric field. The polymer drop is deformed through EHD effect into a Taylor's cone, depositing fibers onto a target substrate.

In fact, the pyro-electric field actives the EHD pressure onto the starting liquid drop, placed onto a flat substrate, and deforms it into a Taylor's cone, until its stretching is long enough to deposit fibers onto a target substrate (Fig. 3.2). Comparing to the classical ES, the field, in the TPES, attracts the entire volume of the reservoir drop, arranging the electric field lines[12]. The stimulus propagated all over the fiber allows manipulating the polymer better during the process, improving the stability and the resolution of the deposition. In other words, the pyro-electric field converges in one point and guides the jet punctually, until the polymer meets the target substrate, drawing a line[13-15]. Through the use of a monitoring system, is it also possible to move the target substrate in order to realize well-ordered patterns[10]. An important parameter to evaluate is the distance d between the reservoir drop and the target substrate: increasing d the spatial resolution also increases, but the field exerts a lower attractive force in the drop. However, during the deposition the drop volume is not constant and decreases progressively; the control of d is a way to try to keep the uniformity of the jet[16].

3.2 Paper: "Direct Writing of Microfluidic Footpaths by Pyro-EHD Printing"

Authors and affiliations

Sara Coppola[a], Giuseppe Nasti[a], Michele Todino[a], Federico Olivieri[a,b], Veronica Vespini[a] and Pietro Ferraro[a]

[a] Institute of Applied Sciences and Intelligent System (CNR-ISASI), Via Campi Flegrei 34, 80078 Pozzuoli (NA), Italy.

[b] Department of Chemical, Materials and Production Engineering, University of Naples, Piazzale Tecchio 80, 80125 Napoli, Italy.

3.2.1 Abstract

In this study, we report a direct writing method for the fabrication of microfluidic footpaths by pyro-EHD jet printing. Here, we propose the use of a nozzle-free three-dimensional printing technique for the fabrication of printed structures that can be embedded in a variety of soft, transparent, flexible, and biocompatible polymers and thus easily integrated into lab-on-chip devices. We prove the advantage of the high resolution and flexibility of pyro-EHD printing for the realization of microfluidic channels well below the standard limit in dimension of conventional ink-jet printing technique and simply adaptable to the end-user desires in terms of geometry and materials. Starting from the description of the innovative approach proposed for the channel fabrication, we demonstrate the design, fabrication, and proof of a microfluidic matrix of interconnected channels. The method described here could be a breakthrough technology for the fabrication of in situ implantable, stretchable, and biocompatible devices, opening new routes in the field of biomedical engineering and wearable electronics.

3.2.2 Introduction

Microfluidics has become a key issue technology for a broad range of audience, from biological analysis and basic cell biology to chemical synthesis or opto-fluidics. In fact, microfluidic devices have shown their potential in many areas, such as clinical analysis[17], high-throughput screening[18], biomedical devices with applications including analysis of DNA and proteins[19], sorting of cells[18], implantable devices, chemical reactions[20-21], transfers of small volumes (1-100 nL) of materials[22], and tools for chemical and biochemical applications. The combination of microfluidics and nanotechnology can be the breakthrough technology that could bring conventional biological lab-on-chip (LOC) and point-of-care (POC) devices to the next generation of applications. Typical uses of microfluidic devices (e.g., chemical analysis) require these systems to be inexpensive and simple to operate. So far, methods used to fabricate micro-

channels have been mostly based on photolithography[23] and soft lithography in case of polymers[24-26], and even more complex techniques, such as stereo-lithography (SL)[27], laser-chemical 3D writing[28], and microjoinery[29], have also been developed to design micro-channels with more complicated geometries. Unfortunately, all of these processes are still expensive and require complex equipment and highly trained staff. In particular, lithography techniques require advanced facilities and numerous process steps and often produce toxic waste. They are also often limited in both material choice and channel geometry. More recently, microfluidic systems have been generally built using a replica molding technique and very few materials, such as the thermosetting PDMS or thermoplastics polymethylmethacrylate and polystyrene. Although applications are not lacking[23,30] and PDMS molding is able to produce micron-resolution features, the PDMS mold fabrication requires a long and slow manual procedure[31]. Additionally, to be cost-effective, molded devices have to be produced on a large scale, requiring very high initial investments, and they cannot be easily customized. Micromilling is an alternative rapid plastic fabrication method allowing more complex geometries and multi-height structures that are not limited to single layers[32]. However, it still requires assembling and bonding to produce closed channels and the milling tool cannot cut arbitrary shapes. All of the proposed methods are layer-by-layer techniques. Each layer is produced as a result of physicochemical steps not specified in the initial photomask(s) that are not well suited for packaging the device into a user-friendly, industry standard unit. The final device needs to be assembled by bonding, resulting in a cost that is very hard to predict at the start of the project. A different approach is represented by SL, which allows the assembly-free production of quasi-arbitrary 3D shapes using a photosensitive resin precursor by means of a focused laser or a digital light projector with improved resolution. Importantly, SL devices can be designed by several groups using CAD tools, conveniently ordered by mail, and their cost precisely predicted via a Web interface[33]. Unfortunately, one major problem related to the SL fabrication methods lies in the resolution in the range of tens or hundreds of microns in width and height of the channels produced. In

fact, SL offers both a more user-friendly technology and a simpler commercialization path compared to those of plastic/PDMS molding. On the other hand, commercial SL systems have laser beam diameters of approximately 100 µm. Therefore, devices with features smaller than this value cannot be readily fabricated using SL. Nano- and micro-miniaturization of devices for use in these areas could lead to many benefits, including reduced manufacturing cost, portability, use and disposal, and reduced time of analysis and consumption of reagents and analytes.

techniques	resolution	fabrication time	cost	mass production	custom-made
pyro-EHD	submicron	fast	low	yes	yes
photo-litography	submicron	medium	very high	yes	no
soft lithography	submicron	long	low	yes	no
SL	100 µm	medium	very high	yes	yes
replica molding	micron	long	medium	yes	yes
laser writing	submicron	fast	high	no	yes
micromilling	micron	fast	high	no	yes

Table 3.1. Comparison of different techniques used for the preparation of micro-channels.
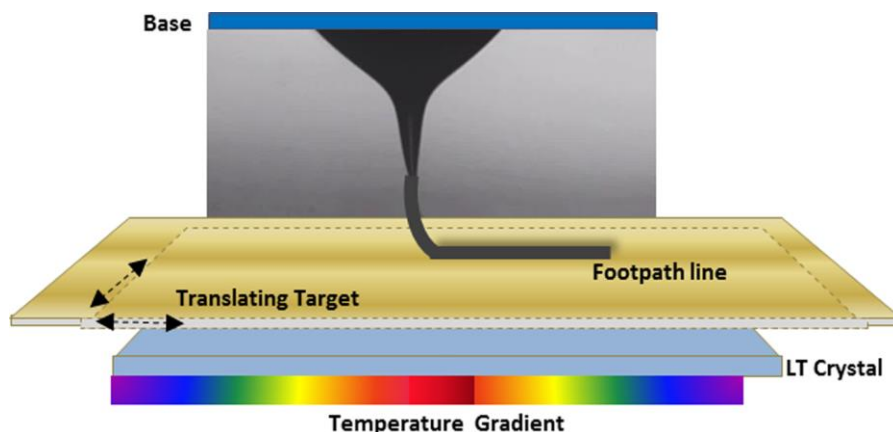
Figure 3.3. Activation of the pyroelectric field of an LT crystal by a wireless thermal source; the poly(lactic-co-glycolic acid) (PLGA) drop starts to deform into a Taylor cone under the action of the pyroelectric charges and prints the polymer fiber onto a target substrate. A computer-controlled translation stage is used for the motion of the substrate, to obtain the footpath line.

Direct writing[34], ink-jet printing[35] and near-field electrospinning[36] have been improved for ink micro-patterning on various kinds of substrates, but the printing of highly viscous polymeric ink and the requirement of a complex system are still a problem. Recently, novel fabrication and high-resolution printing approaches have been pursued on the basis of the pyro-EHD effect for the functionalization of ready-to-use devices and high-resolution patterning of viscous inks[37-39]. Here, we demonstrate the use of this nozzle-less ink-jet printing technique called tethered pyro-electrohydrodynamic spinning (TPES)[10] for the direct printing of footpaths with different geometries and dimensions adopted as templates for fabricating microfluidic channels. We propose two strategies. The first is based on the use of this pyro-printing system combined with the replica molding process. The combination of these two technologies allows the fabrication of microfluidic channels by a two-step process. The second strategy is, instead, a single-step procedure for the direct preparation of microfluidic footpaths inside the microfluidic chips. In this case, the pyro-EHD printing is used for the direct writing of biodegradable polymer guides embedded into a PDMS sample. The

method proposed is fully controllable, easily oriented to the end user, and adaptable for an on-demand printing modality. Compared with standard fabrication methods, as shown in Table 3.1, the pyro-EHD direct writing technique appears more suitable in terms of important parameters, such as resolution, biocompatibility, fabrication time, mass production perspective, custom-made, and cost. In fact, the microfluidic platforms produced are extremely flexible, conformable to irregularly curved surfaces, and could be used for numerous commercial applications of low-cost portable devices, where ultrathin and lightweight features are desirable. Moreover, we show that high-resolution micro-channels achievable by TPES printing have transversal size ranging from hundreds of nanometers to hundreds of microns, well below the limit of resolution of standard methods. The approach proposed has been demonstrated also for processing biocompatible and biodegradable materials so that the devices produced represent useful candidates for biological analysis because of their intrinsic absence of toxicity and immunogenicity[40-41].

3.2.3   Experimental section

3.2.3.1 Device Design and Fabrication

Fig. 3.3 shows the outline of the experimental apparatus used in the current study. A pyro-EHD printer was designed and built to print the micro-channel footpaths[11,42-43]. The pyro-EHD jet printer was composed essentially only of a pyroelectric crystal, a couple of linear translational stages, a target substrate, a support, and a heat source. The printing approach was based on the use of TPES[10] technique thanks to the pyroelectric effect that activates the jetting process. In fact, when a ferroelectric crystal, in our case lithium tantalate (LT), undergoes a temperature variation, it generates an electric field. The TPES exploits the non-uniform electrostatic field for direct spinning of highly viscous polymeric solutions. In fact, this method allows polymer nano-fibers to be printed directly from a polymer drop, thus overpassing the problems due to viscosity that often

causes "nozzle-clogging" in any conventional inkjet system. The drop reservoir is placed directly on the supporting base, and the pyroelectric field exerts an attractive force on the surface of the polymer drop, deforming it into a Taylor cone, thus generating liquid jet emission. Analogously to classical electrospinning, the TPES printer functioning is based on the EHD forces acting on a fluid surface immersed in a spatially non-uniform electric field.
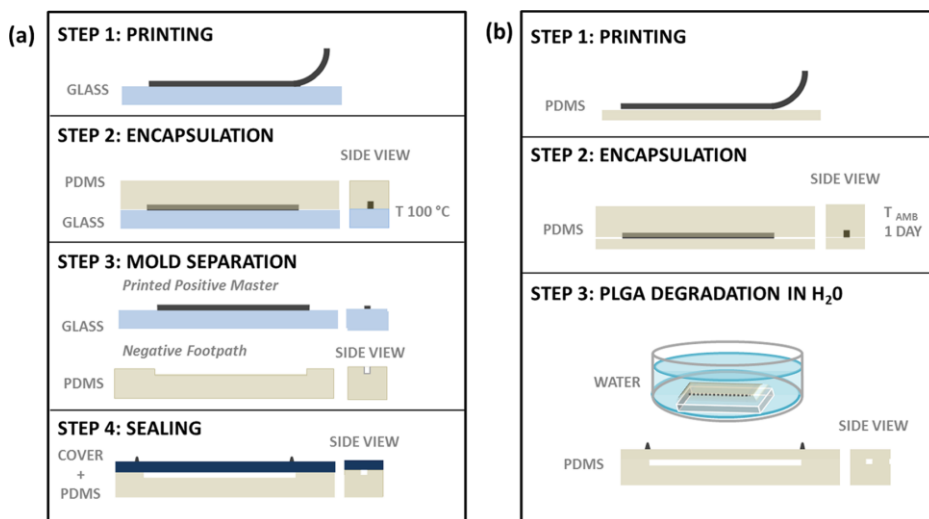

Figure 3.4. Micro-channel fabrication through replica molding case (a). In the first step, a PLGA line is printed onto a glass substrate. In the second step, liquid PDMS is poured onto the line and heated at 100 °C for 20 min. Once PDMS is cured, it is detached from the glass (third step) and this mold is covered with a second layer to close the channel (fourth step). Instead, in the micro-channel fabrication obtained with the embedding of the footpath line between two PDMS layers (b), the PLGA is directly printed onto a PDMS layer. This layer is covered with another PDMS layer (second step). This sandwich is left in water for 7 days (third step) to degrade the PLGA line and create the channel between the PDMS layers.

Fibers stretched from the elongation of the Taylor cone were deposited and printed directly onto the target substrate and used as microfluidic footpaths,

avoiding the use of electronic polymer-loaded syringe pump and external hazardous power supply[10,43]. The two directional movements of the pyro-EHD printer were digitally controlled by stepper motors, consisting of a high-precision linear motor with an x-y axis (SGSP26-100(XY) SIGMA KOKI CO., LTD) and a computer numerical control board (SIGMA KOKI CO., LTD). The software was generated by a MATLAB script and used to control the printing pattern and the moving speed along each axis during the printing process. The polymer used for the fabrication of the footpaths was PLGA (Resomer RG 504, poly(D,L-lactide-co-glycolide) lactide/glycolide 50:50, MW 38 000-54 000, Sigma-Aldrich). PLGA was dissolved in dimethyl carbonate (C_3H_6O, MW: 90.08, Sigma-Aldrich) in 1:3 weight ratio, and the solution was stirred for 10 min at T =50°C to improve its homogeneity. A commercial thermo-cross-linkable PDMS solution (Dow Corning Sylgard 184, 10:1 base-to-curing agent mixing ratio, Midland, MI; η = 3900 cP, ep = 2.65 from datasheet) was chosen as target collector of the PLGA footpaths and used as the main material component of the microfluidic chip. Two different strategies of microfluidic platform fabrication were investigated: (1) fabrication of footpaths master for replica molding [Fig. 3.4(a)] and (2) embedding microfluidic footpaths in a polymer matrix [Fig. 3.4(b)].

3.2.3.2 Fabrication of footpaths master for replica molding

In the first procedure, 3D polymer footpaths were directly printed on a supporting substrate by replica molding and sealing the microfluidic chip. As a proof of concept, we have initially designed and tested a simple and straight polymer footpath. In the first step, we fabricated through TPES a positive relief footpath as a master guide onto a hydrophobic glass substrate coated with a commercial fluorosilane (Fluorolink S10, Solvay Specialty Polymers), in order to produce a hydrophobic coating. We followed the procedure provided by the retailer and prepared a solution of fluorosilane, water, acetic acid and 2-propanol (purchased

from Sigma Aldrich), respectively in 0.1, 0.4, 0.1 and 99.4 wt%. In order to activate the glass surface, it was treated with a O_2 plasma (Femto System, Diener Electronic Gmbh & Co. KG, Ebhaosen, Germany), allowing the chemical bonding of the fluorosilane film. The reaction was totally completed after a day spent at standard conditions. After printing the positive master, in the second and third steps, we prepared the PDMS microfluidic chip by replica molding. The polymer was casted over the hydrophobic substrate encapsulating the master, as shown in Fig. 3.4. The PDMS solution was poured over the footpath and then heated at 100 °C for 20 min on a conventional hot plate to cross-link the polymer. After the curing process, the replica was peeled off the master and the PDMS chip was separated from the printed substrate to obtain a flexible polymer strip, generating a negative replica of the master itself in PDMS (edges on the master appeared as valleys in the replica, see side view). The molded PDMS produces negative replica in terms of open channels that should be sealed to a flat and transparent surface to enclose them. This flat surface could be PDMS, resulting in a channel with homogeneous walls, or another material. In this study, two different materials were used for sealing the micro-channel, glass and PDMS, whose flexibilities vary greatly. In fact, the devices packed with a second layer of PDMS were stretchable and could be very easily deformed and conformed to complex geometry. To improve the adhesion between the packing substrate and the micro-channels, ensuring the sealing, a preliminary O_2 plasma treatment was done to both the surfaces that have been successively placed in contact. In fact, the O_2 plasma treatment on PDMS or glass layer activates silanol groups on the exposed surface. These silanol groups can react with other silanol groups (as well as hydroxyl or carboxyl groups) on another surface when the two layers are brought in conformal contact, forming a tight and irreversible seal (i.e., attempting to break the seal resulted in the failure of the PDMS bulk)[44]. Using the first approach proposed, we started from the printing of the desired patterns and, in four steps, we formed channels in PDMS by replica molding. A desirable progress in the world of polymeric POC systems would consist in avoiding the replica molding procedure, reducing the fabrication steps and limiting the role of

surface chemistry during sealing. To solve this problem, we introduced an alternative and direct procedure of fabrication using an intrinsic property (degradability in water) of the PLGA material.

3.2.3.3 Embedding microfluidic footpaths in a polymer matrix

As described in Introduction, using the TPES technique, PLGA patterns were printed on a cured PDMS substrate. In this case, the PLGA ink used for the fabrication of the master was doped with a fluorochrome (Nile red, $C_{20}H_{18}N_2O_2$, technical grade, Sigma-Aldrich, 2 µg per milligram of PLGA); the dye was introduced for a better visualization of the footpaths profile. The distribution of the fluorochrome inside the polymer appears uniform, due to its molecular polarity and therefore to its solubility in PLGA, even at a concentration of 20 wt%. In the first step, the master was printed in the same way of the previous method described, whereas liquid PDMS (base and curing agent) was casted onto the patterned master substrate [Fig. 3.4(b)] and then the PDMS was cured at room temperature for 24-36 h. The result was a PDMS sample embedding a PLGA-printed fiber. This sample was then immersed in water to dissolve the PLGA[45]. In fact, in the presence of water, PLGA degrades by hydrolysis of its ester linkages. The degradation time requested for PLGA is related to the ratio of monomers used in production. In our experiment, after 7 days, the PLGA line was completely dissolved and high-resolution footpaths were inscribed into the PDMS chip exhibiting a semicylindrical fluorescent shape. Of course, different polymers and processes could be used for reducing the degradation time significantly. The proposed approach could be used also for the functionalization of the inner walls of the channel. In fact, during the degradation of the PLGA, the Nile red molecules diffuse from the solution to the walls of the PDMS channel, making it fluorescent when exposed. Fig. 3.5 shows a simple straight footpath under fluorescent illumination once complete degradation of the PLGA was achieved.
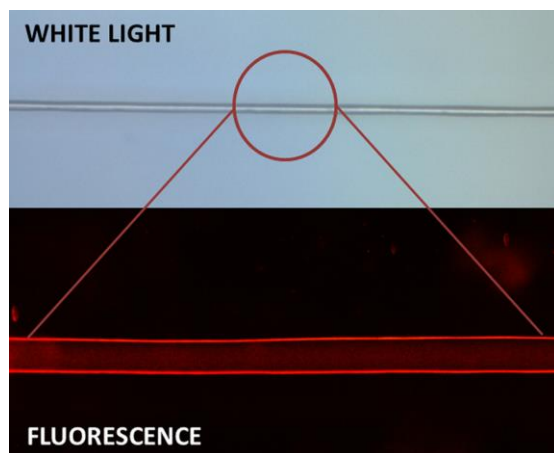
Figure 3.5. Two images of a micro-channel into a PDMS matrix: in bright field (top) and using a fluorescent lamp and a rhodamine filter (bottom). Fluorescent Nile red diffuses from the PLGA to the PDMS during the degradation of PLGA. The diameter of the channel is about 50 µm.

3.2.4 Results and discussion

The fiber diameters printed by TPES depend on the volume of the starting droplets and the working distance between the target and the base substrate. In fact, the pyro-EHD printer lowers the resolution of printing up to attoliter droplets and hundreds of nanometers[11] compared with the picoliter range that is the smallest volume of liquids that can be readily ejected from thermal/piezoelectric print heads, thereby establishing minimum sizes of patterned features as ~10 µm[46]. Higher is the distance between the printing drop and the target, thinner is the printed fiber, as demonstrated in previous studies[11,42]. The achievable width of the deposited lines or droplets can range from few hundreds of nanometers to hundreds of microns[11]. The aspect ratio (i.e., the proportional relationship between the channel width and height) is ~1 during the stable pyro-EHD printing because both height and width change simultaneously. The length of a single printed line can arrive up to 15 cm. For convenient visualization, in the experiments proposed in this study, the length of the channel was reduced to 1.5

cm and the diameter limited to about 2 µm. Fig. 3.6(a) shows the top view of the PDMS device demonstrating good control of direct printing of a single 3D printed footpath, and Fig. 3.6(b) shows the channel cross section. The cross section of the channel is cylindrical, showing the 3D core of the pyro-electro-spun micro-fiber. The morphology and structure of the patterns were characterized by microscopy (Zeiss AXIO Zoom V16) and DH. An interferometric characterization based on DH[47-48] was carried out to evaluate the quality of the surface finishing of the footpaths [Fig. 3.6(c)]. The optical setup used was a classical Mach-Zehnder interferometer in transmission configuration. Starting from the recorded hologram, the intensity and the phase distributions of the optical wavefield transmitted by the sample could be extracted[49-50]. The interferometric image obtained showed a very good internal surface finish for the footpath and its 3D nature in the case of a simple straight channel.
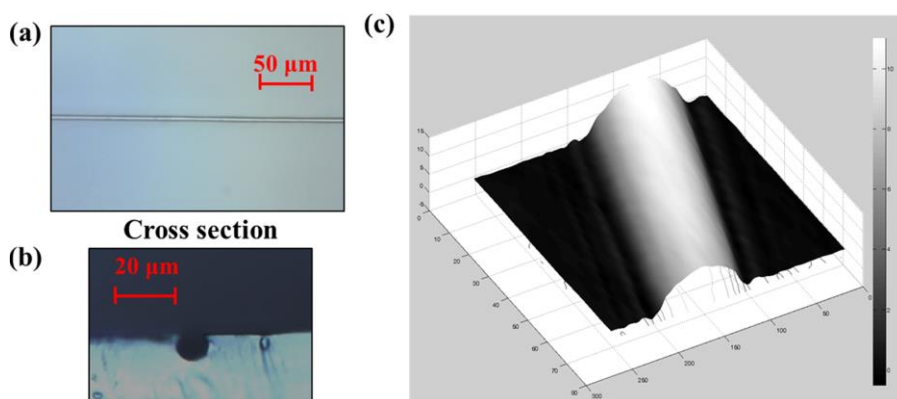
Figure 3.6. Footpath into a PDMS matrix (a) and its section (b). The inner profile of the micro-channel evaluated through DH microscopy (c).

In the following, we show that TPES was useful for the direct writing of more complex microfluidic footpaths. In fact, by using this system and controlling the translators, different geometrical patterns were printed, as shown in Figure 3.5. Crossroads is shown in Figs. 3.7(a) and 3.7(b); a simple Y-junction micro-channel is displayed in Fig. 3.7(c), and a sinusoidal channel is shown in Fig. 3.7(d). The crossflow microfluidic technology, obtainable in case of crossroads

in Figs. 3.7(a) and 3.7(b) by the delivery of a large number of fluid streams, could enable the creation of a unique patterned array system for subsequent high-throughput manipulation and screening. The Y- micro-channel of Fig. 3.7(c) with two lateral inertial migration across laminar co-flowing streams has also been used to achieve fast fluid exchange around cells and particles[51]. This technique relies on the intelligent use of the presence, in this case, of two stable equilibrium positions in low aspect ratio channels. Consequently, with an appropriate outlet design, the particles can be captured in the exchange solution with high purity, high yield, and at a high rate (which is a general characteristic of inertial microfluidic platforms). The sigmoidal channels with alternating curvature of Fig. 3.7(d) were initially introduced to reduce the number of focused streams from straight channels and have also been found to enhance inertial focusing (tighter focusing at shorter downstream distances) compared with straight channels; in particular, they have been employed for accurate positioning of cells for deformability cytometry[52]. By exploiting the polymeric instability of the Taylor cone under the printing action of the pyroelectric field[53] and particularly exploiting the jetting mode observed by Park et al. as a function of the flow rate induced by the electric field strength[54], it would be possible to obtain different and more complex channel shapes, in addition to isolated line and grids. Additionally, the use of the TPES printing system will lead to achieve printing of complex profiles at the nanoscale level; the overlapping of two printed PLGA lines in the junction area could be confined by controlling the starting polymer solution, but this demonstration is beyond the scope of this study.
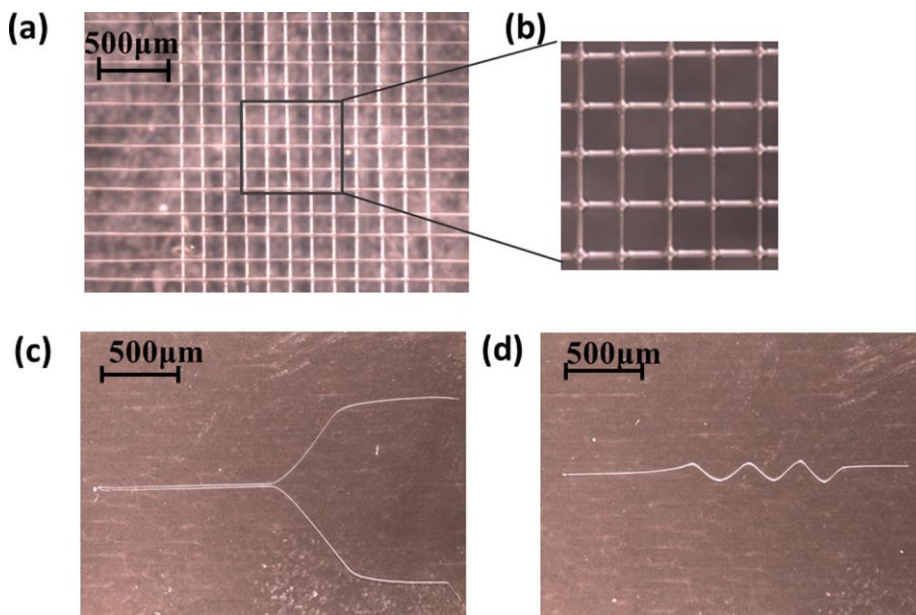
Figure 3.7. Different printed patterns: crossroads (a) and magnified view (b); Y
shape (c) and sinusoidal shape (d).

Fig. 3.8 shows the design of a microfluidic platform directly inscribed into the
polymer matrix using our second method. A continuous serpentine of parallel
channels is printed by TPES, the polymer substrate is then rotated 90°, and the
same circuit of channels is superimposed in the central area of the first one [(Figs.
3.8(a) and 3.8(b)]. A matrix of interconnected channel is fabricated after the
dissolution of the PLGA in water, as already described. During the polymer
curing process, two plastic tips were inserted corresponding to the starting and
final points of the printed channels to prepare the inlet and outlet zones, essential
to fill up and empty the platform. The geometry of the device has been validated
to ensure the accurate prediction of experimental shear stress. To address this
point, the microfluidic properties of the platform were tested in case of oil and
water solutions[*1]. In the experiment proposed in the following, the operating
principle of using micro-channels was based on self-driven capillary effect.

[*1] See supporting movie at DOI: 10.1021/acsami.7b02633

Capillary motion is the ability of a liquid to flow in a narrow space without the assistance of external forces like gravity or syringe pumps. As it is well known, it occurs because of intermolecular forces between the liquid and surrounding solid surfaces. PDMS has a hydrophobic surface and hence these kinds of channels are difficult to wet with aqueous solution. We used plasma treatment to functionalize the micro-channel and improve its hydrophilicity. A plasma treatment actives silanol groups on channel walls that, being polar, support the interaction between the channel and the aqueous solution, facilitating the flow of hydrophilic solutions. In fact, we demonstrated that the channel showed in Fig. 3.8(c) works better after an O_2 plasma treatment. Unfortunately, the effect of the plasma ends in a very short time (about 30 minutes)[17]. In order to obtain a micro-channel having hydrophilicity permanently, a solution of (3-glycidoxypropyl)triethoxysilane (3GPTS, $C_9H_{20}O_5Si$, purchased by Gelest Inc.), ethanol and water was prepared in 5:19:1 volume ratio. Acid acetic was added to the solution to correct the pH to 5. This solution was inserted into the channel after the plasma treatment, exploiting the easy injection of water-based solutions when the silanol groups are activated. The 3GPTS molecules produced silanol groups able to form hydrogen bonds with the groups activated onto the PDMS channel surface. When the water was removed from the system, at the end of the silanization process (about 6 hours, in order to ensure micro-channel complete drying), these hydrogen bonds were transformed into silane covalent bonds, while the external groups of the channel were polar, improving channel hydrophilicity permanently[55]. The microfluidic platform has been completely produced using the elastomeric material, with the advantage of being flexible and adaptable to various shapes [Fig. 3.8(d)]. On the other hand, Figs. 3.8(e) and 3.8(f) shows the operating principle of the cross flow of footpath directly integrated in the matrix of the interconnected channel. The test liquid used in the experiment was a water-based black ink. As all of the channels are interconnected, as a direct consequence of the printing step of a continuous serpentine, they could be filled by introducing the liquid of interest just into the inlet previously prepared. The cross flow generated inside the platform allowed

the simultaneous filling of the 2×2 cm^2 matrix of the micro-channel*[2]. Black dye was used just to visualize the laminar-flow profile along the footpaths.
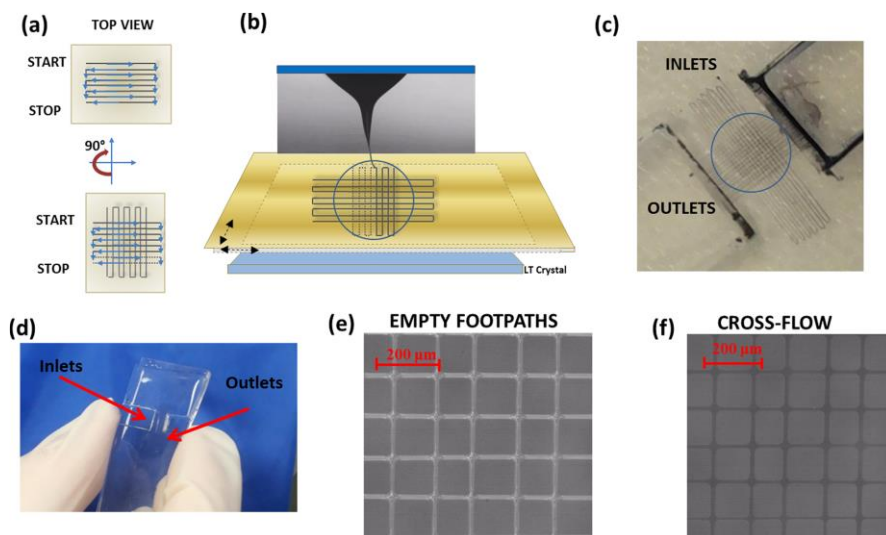

Figure 3.8. (a, b) By exploiting the TPES, a PLGA serpentine pattern is realized, and by replying the pattern and rotating the sample 90°, a crossroad is obtained. (c) A crossroad PDMS-made channel with the inlet and outlet sides for the ink. (d) Polymer channels have more flexibility than glass and PDMS-made ones. Magnified view of interconnected channels: (e) empty and (f) full of black ink.

3.2.5 Conclusions

In conclusion, we have successfully demonstrated that pyro-EHD 3D printing can be useful for direct writing of microfluidic footpaths in LOC polymeric devices. We exploit our innovative technique to create stable and fine jetting using the TPES system. Thus, we overcome the limitations that usually occurred in all previous EHD-based ink-jet printers, achieving a higher resolution in spite of a small footpath diameter and various patterns. We have described and shown two

---

*[2]   See supporting movie at DOI: 10.1021/acsami.7b02633

different approaches for the fabrication of micro-channels. In one case, we introduced an innovative method to create fluorescent channels inside a flexible and transparent polymer platform. We characterized the micro-channels by means of optical and holographic microscopy. Moreover, these microfluidic devices would offer biocompatibility, even with some caveats, because of Nile red, which could be easily replaced by biologically safe dyes, such as green fluorescent protein or quantum dots. Thus, microfluidic chips have the potential for in situ application to biological tissues; they might be used as scaffolds to mimic the biological function of different biological tissues under different physiological conditions and represent an upgrade for supporting the development of healthcare POC devices. Such understanding let us believe that these systems could bring powerful microfluidic techniques to the bench top of researchers who are not expert developers of microfluidic devices.

References

1. Lim, S.H.; Mao, H. Q. Electrospun Scaffolds for Stem Cell Engineering. Adv. Drug Delivery Rev. 2009, 61, 12, 1084-1096.

2. Pisignano, D. Polymer Fibers: Building Blocks for Nanotechnology. Royal Society of Chemistry, 2013.

3. Li, D.; Ouyang, G.; McCann, J. T.; Xia, Y. Collecting Electrospun Nanofibers with Patterned Electrodes. Nano Lett. 2005, 5, 5, 913–916.

4. Li, D.; Xia, Y. Electrospinning of Nanofibers: Reinventing the Wheel? Adv. Mater. 2004, 16, 1151-1170.

5. Chang, G.; Song, G.; Yang, J.; Huang, R.; Rozinda, A.; Shen, J. Morphology Control of Nanohelix by Electrospinning. Appl. Phys. Lett. 2012, 101, 263505.

6. Kim, J. D.; Choi, J. S.; Kim, B. S.; Choi, Y. C.; Cho, Y. W. Piezoelectric Inkjet Printing of Polymers: Stem Cell Patterning on Polymer Substrates. Polymer 2010, 51, 2147−2154.

7. Zheng, G. F.; Li, W. W.; Wang, X.; Wu, D. Z.; Sun, D. H.; Lin, L. W. Precision Deposition of a Nanofibre by Near-Field Electrospinning. J. Phys. D: Appl. Phys. 2010, 43, 415501.

8. Sun, D. H.; Chang, C.; Li, S.; Lin, L. W. Nea-Field Electrospinning. Nano Lett. 2006, 6, 839−842.

9. Huang, Y. A.; Ningbin, B.; Duan, Y.; Pan, Y.; Liu, H.; Yin, Z.; Xiong, Y. Electrohydrodynamic Direct-Writing. Nanoscale 2013, 5, 12007−12017.

10. Coppola, S.; Vespini, V.; Nasti, G.; Gennari, O.; Grilli, S.; Ventre, M.; Iannone, M.; Netti, P. A.; Ferraro, P. Tethered Pyro-Electrohydrodynamic Spinning for Patterning Well-ordered Structures at Micro- and Nanoscale. Chem. Mater. 2014, 26, 3357-3360.

11. Ferraro, P.; Coppola, S.; Grilli, S.; Paturzo, M.; Vespini, V. Dispensing Nano-Pico Droplets and Liquid Patterning by Pyroelectrodynamic Shooting. Nat. Nanotechnol. 2010, 5, 429-435.

12. Reneker, D. H.; Yarin, A. L.; Fong, H.; Koombhongse, S. Bending Instability of Electrically Charged Liquid Jets of Polymer Solutions in Electrospinning. J. Appl. Phys. 2000, 87, 4531−4547.

13. Yarin, A. L.; Koombhongse, S.; Reneker, D. H. Bending Instability in Electrospinning of Nanofibers. J. Appl. Phys. 2001, 89, 3018−3026.

14. Kiselev, P.; Rosell-Llompart, J. Highly Aligned Electrospun Nanofibers by Elimination of the Whipping Motion. J. Appl. Polym. Sci. 2012, 125, 2433−2441.

15. Bhat, P. P.; Appathurai, S.; Harris, M. T.; Pasquali, M.; McKinley, G. H.; Basaran, O. A. Formation of Beads-on-a-String Structures during Break-up of Viscoelastic Filaments. Nat. Phys. 2010, 6, 625−631.

16. Fridrikh, S. V.; Yu, J. H.; Brenner, M. P.; Rutledge, G. C. Controlling the Fiber Diameter during Electrospinning. Phys. Rev. Lett. 2003, 90, 144502, 1-4.

17. Duffy, D. C.; McDonald, J. C.; Schueller, O. J. A.; Whitesides, G. M. Rapid Prototyping of Microfluidic Systems in Poly(dimethylsiloxane). Anal. Chem. 1998, 70, 4974-4984.

18. Qin, D.; Xia, Y.; Whitesides, G. M. Rapid Prototyping of Complex Structures with Feature Sizes Larger Than 20 µm. Adv. Mater. 1996, 8, 917-919.

19. Burns, M. A.; Johnson, B. N.; Brahmasandra, S. N.; Handique, K.; Webster, J. R.; Krishnan, M.; Sammarco, T. S.; Man, P. M.; Jones, D.; Heldsinger, D.; Mastrangelo, C. H.; Burke, D. T. An Integrated Nanoliter DNA Analysis Device. Science 1998, 282, 484-487.

20. Tortora, G. J.; Grabowski, S. R. Principles of Anatomy and Physiology, 7th ed.; Harper Collins: New York, 1996.

21. Manz, A.; Harrison, D. J.; Verpoorte, E.; Widmer, H. M. Planar Chips Technology for Miniaturization of Separation Systems: a Developing Perspective in Chemical Monitoring. Adv. Chromatogr. 1993, 33, 1-65.

22. Terry, S. C.; Jerman, J. H.; Angell, J. B. A Gas Chromatographic Air Analyser Fabricated on Silicon Wafer. IEEE Trans. Electron Devices 1979, 26, 1880-1886.

23. Whitesides, G. M. The Origins and the Future of Microfluidics. Nature 2006, 442, 368-373.

24. Gonzalez, C.; Smith, R. L.; Howitt, D. G.; Collins, S. D. MicroJoinery: Concept, Definition and Application to Microsystem Development. Sens. Actuators, A 1998, 66, 315-332.

25. Jo, B.-H; Van Lerberghe, L. M.; Motsegood, K. M.; Beebe, D. J. Three Dimensional Micro-Channel Fabrication in PDMS Elastomer. J. Microelectromech. Syst. 2000, 9,76-81.

26. Yan, S.; Zhang, X.; Dai, X.; Feng, X.; Du, W.; Liu, B.-F. Rhipsalis (Cactaceae)-Like Hierarchical Structure Based Microfluidic Chip for Highly Efficient Isolation of Rare Cancer Cells. ACS Appl. Mater. Interfaces 2016, 8, 33457-33463.

27. Chen, C.; Hirdes, D.; Folch, A. Gray-Scale Photolithography Using Microfluidic Photomasks. Proc. Natl. Acad. Sci. U.S.A. 2003, 100, 1499-1504.

28. Ikuta, K.; Hirowatiri, H.; Ogata, Y. In Three Dimensional Micro Integrated Fluid Systems (MIFS) Fabricated by Stereo Lithography, Proceedings of IEEE on MEMS, Oiso, 1994; 1-6.

29. Bloomstein, T. M.; Ehrlich, D. J. Laser-Chemical Three Dimensional Writing for Microelectromechanics and Application to Standard-Cell Microfluidics. J. Vac. Sci. Technol., B 1992, 10, 26712674.

30. Mizukami, Y.; Rajniak, D.; Rajniak, A.; Nishimura, M. A Novel Microchip for Capillary Electrophoresis with Acrylic Microchannel Fabricated on Photosensor Array. Sens. Actuators, B 2002, 81, 202209.

31. Tse, L. A.; Hesketh, P. J.; Rosen, D. W.; Gole, J. L. Stereolithography on Silicon for Microfluidics and Microsensor Packaging. Microsyst. Technol. 2003, 9, 319-323.

32. Tang, S. K. Y.; Whitesides, G. M. Optical Components Based on Dynamic Liquid-Liquid Interfaces. In Optofluidics: Fundamentals, Devices, and Application; Fainman, Y., Psaltis, D., Yang, C., Eds.; McGraw-Hill, 2010; 3, 33-57.

33. Au, A. K.; Lee, W.; Folch, A. Mail-order Microfluidics: Evaluation of Stereolithography for the Production of Microfluidic Devices. Lab Chip 2014, 14, 1294-1301.

34. Li, R. Z.; Hu, A.; Zhang, T.; Oakes, K. D. Direct Writing on Paper of Foldable Capacitive Touch Pads with Silver Nanowire Inks. ACS Appl. Mater. Interfaces 2014, 6, 21721-21729.

35. Samusjew, A.; Kratzer, M.; Moser, A.; Teichert, C.; Krawczyk, K. K.; Griesser, T. Inkjet Printing of Soft, Stretchable Optical Waveguides through the Photopolymerization of High-Profile Linear Patterns. ACS Appl. Mater. Interfaces 2017, 9, 4941-4947.

36. Li, X.; Li, Z.; Wang, L.; Ma, G.; Meng, F.; Pritchard, R. H.; Gill, E. L.; Liu, Y.; Huang, Y. Y. Low-Voltage Continuous Electrospinning Patterning. ACS Appl. Mater. Interfaces 2016, 8, 32120-32131.

37. Battista, L.; Mecozzi, L.; Coppola, S.; Vespini, V.; Grilli, S.; Ferraro, P. Graphene and Carbon Black Nano-Composite Polymer Absorbers for a Pyro-Electric Solar Energy Harvesting Device Based on $LiNbO_3$ Crystals. Appl. Energy 2014, 136, 357-362.

38. Vespini, V.; Coppola, S.; Grilli, S.; Paturzo, M.; Ferraro, P. Pyroelectric Adaptive Nanodispenser (PYRANA) Microrobot for Liquid Delivery on a Target. Lab Chip 2011, 11, 3148-3152.

39. Grimaldi, I. A.; Coppola, S.; Loffredo, F.; Villani, F.; Minarini, C.; Vespini, V.; Miccio, L.; Grilli, S.; Ferraro, P. Printing of Polymer Microlenses by a Pyroelectrohydrodynamic Dispensing Approach. Opt. Lett. 2012, 37, 2460-2462.

40. Omenetto, F. G.; Kaplan, D. L. New Opportunities for an Ancient Material. Science 2010, 329, 528-531.

41. Vepari, C.; Kaplan, D. L. Silk as a Biomaterial. Prog. Polym. Sci. 2007, 32, 991-1007.

42. Vespini, V.; Coppola, S.; Todino, M.; Paturzo, M.; Bianco, V.; Grilli, S.; Ferraro, P. Forward Electrohydrodynamic Inkjet Printing of Optical Microlenses on Microfluidic Devices. Lab Chip 2016, 16, 326-333.

43. Coppola, S.; Vespini, V.; Grilli, S.; Ferraro, P. Self-Assembling of Multi-Jets by Pyro-electrohydrodynamic Effect for High Throughput Liquid Nanodrops Transfer. Lab Chip 2011, 11, 3294-3298.

44. Chaudhury, M. K.; Whitesides, G. M. Direct Measurement of Interfacial Interactions between Semispherical Lenses and Flat Sheets of Poly(dimethylsiloxane) and Their Chemical Derivatives. Langmuir 1991, 7, 1013-1025.

45. Shive, M. S.; Anderson, J. M. Biodegradation and Biocompatibility of PLA and PLGA Microspheres. Adv. Drug Delivery Rev. 1997, 28, 5-24.

46. Kuang, M.; Wang, L. B.; Song, Y. L. Controllable Printing Droplets for High-Resolution Patterns. Adv. Mater. 2014, 26, 69506958.

47. Merola, F.; Miccio, L.; Coppola, S.; Vespini, V.; Paturzo, M.; Grilli, S.; Ferraro, P. Exploring the Capabilities of Digital Holography as Tool for Testing Optical Microstructures. 3D Res. 2011, 2, No. 43.

48. Ferraro, P.; Adam, W.; Zalevsky, Z. Imaging and Quantitative Phase Analysis. In Coherent Light Microscopy. Eds.; Springer Series in Surface Sciences; Springer Science & Business Media, 2011; 3, 61-85.

49. Marquet, P.; Depeursinge, C.; Magistretti, P. J. Review of Quantitative Phase-Digital Holographic Microscopy: Promising Novel Imaging Technique to Resolve Neuronal Network Activity and Identify Cellular Biomarkers of Psychiatric Disorders. Neurophotonics 2014, 1, 020901.

50. Merola, F.; Memmolo, P.; Miccio, L.; Bianco, V.; Paturzo, M.; Ferraro, P. Diagnostic Tools for Lab-on-Chip Applications Based on Coherent Imaging Microscopy. Proc. IEEE 2015, 103, 192-204.

51. Gossett, D. R.; Tse, H. T. K.; Dudani, J. S.; Goda, K.; Woods, T. A.; Graves, S. W.; Di Carlo, D. Inertial Manipulation and Transfer of Microparticles across Laminar Fluid Streams. Small 2012, 8, 2757-2764.

52. Gossett, D. R.; Tse, H. T. K.; Lee, S. A.; Ying, Y.; Lindgren, A. G.; Yang, O. O.; Rao, J.; Clark, A. T.; Carlo, D. D. Hydrodynamic Stretching of Single Cells for Large Population Mechanical Phenotyping. Proc. Natl. Acad. Sci. U. S. A. 2012, 109, 7630-7635.

53. Parekh, D. P.; Ladd, C.; Panich, L.; Moussa, K.; Dickey, M. D. 3D Printing of Liquid Metals as Fugitive Inks for Fabrication of 3D Microfluidic Channels. Lab Chip 2016, 16, 1812-1820.

54. Park, J. U.; Hardy, M.; Kang, S. J.; Barton, K.; Adair, K.; Mukhopadhyay, D. K.; Lee, C. Y.; Strano, M. S.; Alleyne, A. G.; Georgiadis, J. G.; Ferreira, P. M.; Rogers, J. A. High-Resolution Electrohydrodynamic Jet Printing. Nat. Mater. 2007, 6, 782-789.

55. Hoang, M. V.; Chung, H.-J.; Elias, A. L. Irreversible Bonding of Polyimide and Polydimethylsiloxane (PDMS) Based on a Thiol-Epoxy Click Reaction. J. Micromech. Microeng. 2016, 26, 105019-105027.

CHAPTER 4

CONCLUSIONS

This thesis was focused on the exploitation of pyroelectric fields to manipulate polymeric solutions with the use of a LN crystal. In particular, the combination between pyroelectricity and EHD was investigated, in order to realize single polymeric micro-lenses or micro-lenses arrays (as reported in Chapter 2) and to fabricate micro-fluidic channels (presented in Chapter 3). About the lenses fabrication, the first approach proposed was based on the pyro-EHD dispenser, a printing technique patented by CNR-ISASI. The pyro-EHD dispenser proposes an alternative procedure to the classic EHD printers, which permits to avoid the use of electrodes and nozzle and offers the chance to print several kind of polymers in micro- and nano-scale with high resolution. Specifically, the micro-lenses fabrication proposed passes through the evolution of the pyro-EHD dispenser setup: the flexibility of the system is then enhanced passing to the forward pyro-EHD configuration. The novelty of the forward setup consist of the localizing of the starting drop at the same side of the crystal, while in the classic configuration it lies on the base opposite to the crystal. In other words, the limitations that occurred in conventional EHD printing systems, consisting of the target substrate inserted between the two electrodes, were exceeded. In this way, it is potentially possible to print on any kind of substrate. This was validated in Chapter 2.3 by the direct printing of micro-lenses onto a commercial micro-fluidic channel. The setup produces lenses with high resolution and the lenses show uniform sizes and shapes. The quality of the lenses was tested with a geometric and optical characterization. A second approach to fabricate the lenses exploits the pattern impressed onto a poled pyroelectric crystal to create lenses arrays; the pyroelectric field lines guide the polymer (PDMS) that, due to EHD effect, self-assembles on the crystal and assumes the shape of a lenses array, as confirmed by an optical characterization. When nano-fillers (such as semi-conductive nano-rods) are added to PDMS, during the application of the pyroelectric field, these move into the polymer matrix due to DEP effect, creating well-ordered nano-composites onto the crystal surface. In Chapter 2.5 the arrangement of quantum dots onto self-assembled micro-lenses was proposed; DEP effect onto QDs has been evaluated. Furthermore, the attention has been

focused on self-assembled lenses arrays onto crystals having small hexagon patterns (25 and 50 μm) and on the pattern transfer onto an external polymeric membrane. In Chapter 3 the fabrication of micro-fluidic devices through pyro-EHD effect was reported. In particular, pyro-EHD dispenser, in its classic configuration, allowed to use highly viscous polymeric solutions, which can deposit polymeric fibers, representing an alternative to the electrospinning. A movement stage system assisted the deposition along the target substrate. The produced fibers were characterized by the typical pyro-EHD printer uniformity and their dimensions ranged from hundreds of microns to hundreds of nanometers. The TPES technique, analyzed in Chapter 3, was used to print PLGA fibers in order to realize patterns for micro-channels. The flexibility of the technique permitted to write patterns of different shapes and dimensions and the fiber maintained its shape in the polymeric (PDMS) matrix, used to fabricate the micro-channel. Replica molding and plasma treatment processes completed the channel fabrication. It was also showed the possibility to functionalize the inner channel walls and to improve the hydrophilicity of the channel. Definitely, pyro-EHD represents an attractive solution to many technological fields, such as optics and microfluidics, due to its versatility. High resolution patterning and printing have also great interest in nano-technology or biology, where the touch-less approach constitutes another interesting skill. The miniaturization of the devices and the possibility to optimize lab-on-a-chip systems is a very impressive research feature. The potentiality of the setup could be further explored, realizing patterns made of different materials, suitable, for example, for electronic industry. The functionalization of micro-structures is considered, on the other hand, very interesting for photonics and composite industry.

Aknowledgements

accompagna in ogni momento, nel mio fantastico presente, fin nel lucente futuro; la mia avventura, il mio amore, la mia Donna: Rachele.

Da Piazzale Tecchio 80 è tutto, a voi studio!